

© Copyright by Qingzhao Kong, 2015

All Rights Reserved.

**INNOVATION IN PIEZOCERAMIC BASED STRUCTURAL HEALTH
MONITORING**

A Dissertation

Presented to

the Faculty of the Department of Mechanical Engineering

University of Houston

In Partial Fulfillment

of the Requirements for the Degree

Doctor of Philosophy

in

Mechanical Engineering

by

Qingzhao Kong

May 2015

**INNOVATION IN PIEZOCERAMIC BASED STRUCTURAL HEALTH
MONITORING**

Qingzhao Kong

Approved:

Chair of the Committee
Gangbing Song, Professor
Mechanical Engineering

Committee Members:

Matthew Franchek, Professor
Mechanical Engineering

Yi-Lung Mo, Professor
Civil and Environmental Engineering

Li Sun, Associate Professor
Mechanical Engineering

Mo Li, Assistant Professor
Civil and Environmental Engineering

Suresh K. Khator, Associate Dean
Cullen College of Engineering

Pradeep Sharma, Professor and Chair
Mechanical Engineering

Acknowledgements

I would like to express my deepest appreciation and be forever thankful to my advisor, Dr. Gangbing Song, for his excellent guidance, patience, encouragement and support during my studies in these years. I am extremely lucky to have an advisor who has been helpful in providing so much care and instructions for my research field. In addition, Dr. Gangbing Song taught me how to behave in both my research and my life which I will never forget. I would like to give my special thanks to Dr. Yi-Lung Mo for guiding me in many experiments and helping me to develop my knowledge in civil engineering. I would also like to show my gratitude to Dr. Matthew Franchek, Dr. Li Sun, and Dr. Mo Li for spending time reading my thesis and providing precious suggestions to improve the quality of the thesis.

I would also like to acknowledge all my colleagues for their assistants in many aspects during these years. I especially thank Dr. Siu Chun Michael Ho and Miss. Rachel Hirsch for proofreading and improvement of my papers, reports, presentations and dissertation, Mr. Devendra Patil for his professional assistance in mechanical design and experimental setup, and Mr. Jiabiao Ruan for his expertise in data acquisition and instrumentations. Many thanks to Dr. Haichang Gu, Mr. Junxiao Zhu, Miss. Qing Ji, Mr. Chenyu Wang, Mr. Mohammad Parvasi, Mr. Jianjun Wang, Mr. Feng Qin for their assistance and suggestions in my research and dissertation writing.

Finally, I owe more than thanks to my parents who gave me financial assistance and spiritual encouragement throughout my life.

**INNOVATION IN PIEZOCERAMIC BASED STRUCTURAL HEALTH
MONITORING**

An Abstract

of a

A Dissertation

Presented to

the Faculty of the Department of Mechanical Engineering

University of Houston

In Partial Fulfillment

of the Requirements for the Degree

Doctor of Philosophy

in

Mechanical Engineering

by

Qingzhao Kong

May 2015

vi

Abstract

Recent structural failures in both developing and developed countries highlight the importance of structural health monitoring, which has the ability to provide early warning based on real time monitoring of the structure of interest. The versatile functions and low cost of piezoceramic material has demonstrated its capability as transducers in structural health monitoring. This dissertation investigated modeling and innovative applications using piezoceramic based smart aggregate transducers for health monitoring of various structures.

A theoretical and experimental modeling study of piezoceramic based smart aggregates were firstly conducted. Fundamental equations of a smart aggregate were established and numerical simulations were performed. The resonance and anti-resonance frequencies of a smart aggregate sample were computed, and were later verified by experimental tests.

Many structural failures were initiated by cracks. A chapter of this dissertation is devoted to crack detection using piezoceramic based transducers. Two types of structures, a pipeline and a concrete column, were investigated. For the pipeline structure, an active sensing system with distributed actuators and sensors detects the crack and monitor the crack development. For the concrete column, the cyclic crack open-close condition was determined by embedded smart aggregates using wavelet packet-based structural damage index.

Steel plate reinforced concrete structures are increasingly used in civil engineering. However, the bonding between the steel plate and the concrete is not well studied nor well known. This dissertation investigated detection of bond slip between the steel plate and concrete using smart aggregates. With appropriate deployment of smart aggregates in concrete structure and steel plate surface, shear stress induced bond slip phenomenon was monitored in real time. The severity of debonding was also characterized using the proposed method.

Concrete structures are often used as underground containment for nuclear materials. Cracks and underground water are a lethal combination to migrate the radioactive pollution. This dissertation proposed an effective active sensing based method to detect concrete cracks and to further detect water presence in these concrete cracks, as experimentally demonstrated.

Concrete is the most popular structural material and understanding its very early age (0-20 hours) hydration performance is of great importance. This dissertation proposes a novel approach to this topic using smart aggregate based active sensing approach. Two modes of smart aggregate, compressive mode and shear mode, were investigated and the results were compared. Both time domain and frequency domain analyses were conducted and the proposed approach can clearly identify the three distinct states, the liquid state, the transition state, and the hardened state, during the concrete hydration process.

Soil freeze-thaw condition plays an important role in structural soil interaction in cold regions. The last chapter of this dissertation presents an innovative active sensing

based method to monitor soil freeze-thaw condition using embedded smart aggregates. Since wave propagation is highly sensitive to the mechanical properties of soil during the freezing and thawing process, the received stress wave can be an effective indicator to determine the soil status. A wavelet packet-based soil frozen index was proposed and successfully applied to monitor the soil freezing or thawing status.

Table of Contents

Acknowledgements.....	v
Abstract.....	vii
Table of Contents	x
List of Figures	xv
List of Tables	xxvi
1 Introduction.....	1
1.1 Motivations and Objectives	1
1.2 Contributions.....	3
1.3 Organization.....	5
2 Introduction to structural health monitoring.....	8
2.1 Definition of damage	8
2.2 Implemented transducers	10
2.2.1 Strain gauge sensor	10
2.2.2 Fiber Optic sensor	10
2.2.3 <i>Piezoceramic based transducer</i>	11
2.3 Feature extraction and information condensation.....	11
2.3.1 Dynamic response characteristics	12
2.3.2 New features and techniques	14

2.4	Advanced Signal processing methods	17
2.4.1	Wavelet packet-based analysis	17
2.4.2	Polar plot analysis	18
2.4.3	Time reversal technique	19
2.4.4	Canonical variate analysis.....	20
2.5	Piezoceramic transducers.....	20
2.6	Smart aggregate transducer.....	23
2.6.1	Introduction to smart aggregate	23
2.6.2	Applications of smart aggregates for structural health monitoring	26
2.7	Structural damage index	31
3	Theoretical and experimental characterization of smart aggregate properties	33
3.1	Introduction.....	33
3.2	Basic equations	34
3.2.1	Constitutive equations.....	35
3.2.2	Geometric relationship equations	36
3.2.3	Electrostatic charge equations.....	37
3.2.4	Dynamic equilibrium equations.....	37
3.3	Dynamic solution of smart aggregate	39
3.4	Numerical simulations	42

3.5	Experimental verification.....	44
3.6	Summary	46
4	Structural crack monitoring	47
4.1	Introduction.....	47
4.2	Detection principles	48
4.3	Crack monitoring of a pipeline	49
4.3.1	Background.....	49
4.3.2	Experimental setup and procedures	50
4.3.3	Experimental results.....	53
4.3.4	Discussion.....	56
4.4	Crack monitoring of a concrete column due to simulated pseudo-dynamic load.	57
4.4.1	Background.....	57
4.4.2	Experimental setup and procedures	57
4.4.3	Experimental results and discussions.....	60
4.5	Summary	69
5	Bond slip detection of steel plate concrete beams	70
5.1	Introduction.....	70
5.2	Detection principles	72
5.3	Bond slip detection of steel plate reinforced concrete beams.....	73

5.3.1	Experimental results and discussions.....	73
5.3.2	Experimental setup and procedures	90
5.4	Summary.....	95
6	Water presence detection in concrete cracks	96
6.1	Introduction.....	96
6.2	Detection principles	97
6.3	Simple experimental verifications	98
6.3.1	Water existence detection	98
6.3.2	Water quantity detection.....	100
6.4	Water detection in a concrete crack	101
6.4.1	Experimental setup and procedures	101
6.4.2	Experimental results and discussions.....	104
6.5	Summary.....	106
7	Very early age concrete hydration monitoring	107
7.1	Introduction.....	107
7.2	Very early age concrete hydration monitoring using smart aggregates.....	109
7.2.1	A concrete beam test using compressive mode smart aggregates	109
7.2.2	A concrete beam test using both compressive mode and shear mode smart aggregates	115

7.3	Summary	123
8	Soil freeze-thaw monitoring	124
8.1	Introduction.....	124
8.2	Detection principles	125
8.3	A small scale soil specimen test.....	126
8.3.1	Experimental setup and procedures	126
8.3.2	Experimental results and discussions.....	129
8.4	A large scale soil specimen test	139
8.4.1	Experimental setup and procedures	139
8.4.2	Experimental results and discussions.....	141
8.5	Summary	144
9	General Conclusions and Future Works	145
	References.....	148
	Appendices.....	171

List of Figures

Figure 2-1 Decomposition tree of wavelet package analysis.....	18
Figure 2-2 Piezoelectric elementary cell (1): Before poling (Left) (2): After poling (Right)	21
Figure 2-3 PZT patch in compression mode.....	22
Figure 2-4 PZT patch in shear mode.....	23
Figure 2-5 First generation of smart aggregate and its structure	23
Figure 2-6 Second generation of smart aggregate and its structure.....	24
Figure 2-7 Smart aggregates with different protected materials.....	25
Figure 2-8 A sine wave with the constant frequency of 30Hz.....	27
Figure 2-9 an example of a swept frequency signal	28
Figure 2-10 Experimental setup of an active sensing test using smart aggregates	29
Figure 2-11 A zoom in photo of two bonded smart aggregates.....	29
Figure 2-12 Received sensor signal from the actuator.....	30

Figure 2-13 The power spectrum of the sensor signal	30
Figure 3-1 Test smart aggregate samples and schematic of a smart aggregate	34
Figure 3-2 A simplified model for a second generation smart aggregate.....	35
Figure 3-3 The influence of the thickness of the whole epoxy between two Marbles on the fundamental resonance and anti-resonance frequencies as well as the corresponding electromechanical coupling factor	43
Figure 3-4 The influence of the thickness of the PZT patch on the fundamental resonance and anti-resonance frequencies as well as the corresponding electromechanical coupling factor	44
Figure 3-5 The influence of the diameter of the PZT patch on the fundamental resonance and anti-resonance frequencies as well as the corresponding electromechanical coupling factor	44
Figure 3-6 Experiment setup.....	45
Figure 3-7 Relationship between impedance and frequency for smart aggregates	46
Figure 4-1 Block diagram of smart aggregate based active sensing system.....	49
Figure 4-2 location of PZT patches on the pipeline.....	51

Figure 4-3 A photo of pipeline specimen with PZT patches	51
Figure 4-4 Experimental setup.....	52
Figure 4-5 One section of the swept sine wave signal used in the experiment	53
Figure 4-6 Signal response of PZT 2 for Each Operating Condition (OC)	54
Figure 4-7 Signal response of PZT 3 for Each Operating Condition (OC)	54
Figure 4-8 Signal response of PZT 4 for Each Operating Condition (OC)	55
Figure 4-9 Wavelet packet-based pipeline crack severity index	56
Figure 4-10 Location of smart aggregates in the concrete column.....	58
Figure 4-11 (a) A smart aggregate fixed on the rebar cage (b) A Smart aggregate was installed in the base.....	58
Figure 4-12 A photo of the concrete column after casing	59
Figure 4-13 Acceleration record	60
Figure 4-14 Response spectrum.....	60
Figure 4-15 Force-displacement relationships for the concrete column.....	61

Figure 4-16 Moment-curvature relationships for concrete column	61
Figure 4-17 A photo of the concrete column yielding after test	62
Figure 4-18 Displacement history in x-direction of the column.....	62
Figure 4-19 wave packet-based damage index for the concrete column	63
Figure 4-20 Damage index of the concrete column in first 1000 steps	64
Figure 4-21 Damage indices of the concrete column from step 1000 to step 2100.....	65
Figure 4-22 Damage indices of the concrete column from step 2100 to step 3300.....	66
Figure 4-23 Damage index of the concrete column from step 3400 to step 4000	67
Figure 4-24 Damage indices of the concrete column from different locations (a) Bottom sensors, (b) Middle sensors, (c) Top sensors	69
Figure 5-1 Applications of steel plate concrete structures	71
Figure 5-2 Block diagram of smart aggregate based bond slip detection between concrete and steel plate.....	73
Figure 5-3 Shear Force vs. time of SC1 north and south.....	73
Figure 5-4 Shear Force vs. time of SC4 north and south.....	74

Figure 5-5 Details of crack on north side of SC1 after loading	75
Figure 5-6 Details of cracks on south side of SC1 after loading	75
Figure 5-7 Damage index of SA1 on north side of SC1	76
Figure 5-8 Damage index of SA2 on north side of SC1	77
Figure 5-9 Damage index of SA3 on north side of SC1	78
Figure 5-10 Damage index of SA4 on north side of SC1	79
Figure 5-11 Damage index of SA5 on south side of SC1	80
Figure 5-12 Damage index of SA6 on south side of SC1	81
Figure 5-13 Damage index of SA7 on south side of SC1	81
Figure 5-14 Damage index of SA8 on south side of SC1	82
Figure 5-15 Details of crack on north side of SC4 after loading	83
Figure 5-16 Damage index of SA1 on north side of SC4	83
Figure 5-17 Damage index of SA2 on north side of SC4	84
Figure 5-18 Damage index of SA3 on north side of SC4	85

Figure 5-19 Damage index of SA4 on north side of SC4.....	86
Figure 5-20 Damage index of SA4 on north side of SC4.....	86
Figure 5-21 Damage index of SA5 on south side of SC4.....	87
Figure 5-22 Damage index of SA6 on south side of SC4.....	88
Figure 5-23 Damage index of SA8 on south side of SC4.....	89
Fig. 1 Figure 5-24 Shear force vs. damage index of SC1 and SC4.....	90
Figure 5-25 Dimensions of SC beam specimens (unit: inch)	92
Figure 5-26 A photo of steel plates with welded reinforcement bar for SC1	92
Figure 5-27 Location of smart aggregates in SC 1 (Unit: Inch)	93
Figure 5-28 Location of smart aggregates in SC 4 (Unit: Inch)	93
Figure 5-29 Smart aggregate fixed between reinforcement rebar (left)and attached on steel plate (right)	93
Figure 5-30 Experimental diagram	94
Figure 5-31 Experimental setup of SC1.....	94

Figure 5-32 The loading actuators and the casted concrete beam of SC1	95
Figure 6-1 Schematic diagram of stress wave propagation through a concrete crack.....	97
Figure 6-2 Diagram of stress wave propagation through a water filled concrete crack ...	98
Figure 6-3 Experimental setup of water drop detection.....	99
Figure 6-4 Sensor voltage plot in two cases	100
Figure 6-5 Experimental setup of water quantity detection and the schematic diagram	100
Figure 6-6 Sensor voltage plot in three cases	101
Figure 6-7 Concrete Beam embedded with three smart aggregates	102
Figure 6-8 Orientation and location of smart aggregates.....	102
Figure 6-9 Experimental Setup of the loading process.....	102
Figure 6-10 A photo of the concrete beam with a large crack after loading	102
Figure 6-11 The concrete beam filled in a water container	103
Figure 6-12 An example of swept sine wave lasted for 0.3s	103

Figure 6-13 Sensor voltage graphic: (a): SA 1, no crack and no water; (b): SA 2, no crack and no water; (c): SA 1, with crack but no water; (d): SA 2, with crack but no water; (e): SA 1, with water in crack; (f): SA 2, with water in crack.....	105
Figure 6-14 Sensor energy performance of SA (1) and SA (2) in three cases.....	106
Figure 7-1 (a) smart aggregates installed beside reinforcement rebar (b) A photo of the test concrete beam after casing	110
Figure 7-2 Schematic diagram of the experimental setup	110
Figure 7-3 Time domain signal response of the fluid stage at (a): 15 minutes; (b): 30 minutes; (c): 45 minutes; (d): 1 hour	112
Figure 7-4 Frequency domain signal response of the fluid stage	112
Figure 7-5 Time domain signal response of the transition stage (a): 2 hours; (b): 3hours (c): 4hours (d): 4.5 hours (e): 5 hours (f): 6 hours; (g): 7 hours (h): 7.5 hours.....	113
Figure 7-6 Frequency domain signal response of the transition stage.....	113
Figure 7-7 Time domain signal response of the hardened stage (a): 8 hours; (b): 10 hours (c): 12 hours (d): 16 hours	114
Figure 7-8 Frequency domain signal response of the transition stage.....	114

Figure 7-9 Frequency domain signal response during the concrete hydration	115
Figure 7-10 The schematic of the proposed concrete beam with embedded smart aggregates	116
Figure 7-11 The orientation of two pairs of smart aggregates.....	117
Figure 7-12 A photo of the concrete mold with installed smart aggregates	117
Figure 7-13 Power Spectrum Density of SMSA Sensor Signal during the entire concrete hydration process	118
Figure 7-14 Resonance frequency (a) and the corresponding signal power (b) for SMSAs	119
Figure 7-15 Power Spectrum Density of CMSA Sensor Signal during the entire concrete hydration process	119
Figure 7-16 Resonance frequency (a) and the corresponding signal power (b) for CMSAs	120
Figure 7-17 The amplitude of received signal under the constant frequency sine wave excitation (90 kHz and 100 kHz).....	122
Figure 8-1 Schematic diagram of smart aggregate based active sensing approach	126

Figure 8-2 A proposed active sensing system with multiple smart aggregates for soil freeze-thaw monitoring.....	126
Figure 8-3 A photo of the test soil specimen with transducers.....	127
Figure 8-4 Schematic of the test soil specimen and sensor location.....	127
Figure 8-5 Particle size distribution of the soil specimen.....	128
Figure 8-6 Specimen temperature monitoring during the freezing-thawing cycle.....	130
Figure 8-7 Signal recorded by the SA sensor during the freezing process.....	131
Figure 8-8 Power Spectrum Density at different soil temperature during the freeze-thaw cycle.....	132
Figure 8-9 Energy vector plot in different freezing and thawing degrees.....	136
Figure 8-10 Calculated signal energy of two resonant frequency peaks in different temperature.....	137
Figure 8-11 The values of resonance frequencies of two resonant frequency peaks in different temperature.....	137
Figure 8-12 Wavelet packet-based soil frozen index.....	138

Figure 8-13 Experimental setup..... 140

Figure 8-14 Recorded signal of the SA sensor for the unfrozen soil..... 141

Figure 8-15 sensor signal in one sweep period at different temperatures..... 142

Figure 8-16 Wavelet packet based soil freeze-thaw status indicator 143

Figure 8-17 The hysteresis loop of freeze-thaw status indicator vs. temperature 144

List of Tables

Table 2-1 Mechanical properties of concrete and marble.....	24
Table 3-1 Material properties.....	42
Table 3-2 Theoretical and experimental results.....	46
Table 4-1 Pipeline dimensions and Q235 steel properties.....	50
Table 4-2 Important properties of PZT patches used in the experiment.....	51
Table 4-3 Test operating conditions (OCs).....	52
Table 5-1 Damage information of each beam.....	74
Table 5-2 Detailed information of the test beams.....	91
Table 6-1 Detailed parameters of the guided swept sine wave.....	103
Table 7-1 Parameters of the Swept Sine Wave.....	110
Table 7-2 Composition details of the TxDoT traditional concrete mix.....	110
Table 7-3 Comparison results between SMSA and CMSA.....	121
Table 8-1 Properties of the smart aggregates.....	127

Table 8-2 Parameters of the swept sine wave	129
Table 8-3 Frequency and amplitude of the 1st RFP at various soil temperatures	133
Table 8-4 Frequency and amplitude of the 2nd RFP at various soil temperatures	133
Table 8-5 Pressure and shear wave velocity of the soil specimen at various temperatures	135
Table 8-6 Parameters of the excitation sine wave	141

1 Introduction

In the 21st century, structural health monitoring has become a grand challenge for civil, aerospace, and mechanical engineers. The outcomes of ongoing developments in structural health monitoring include new sensors, advanced algorithms, and comprehensive implementations. Piezoceramic materials, as one of the “smart materials” with both sensing and actuating ability, wide frequency range, long service life, and low cost, have been used to develop transducers in industrial applications. Meanwhile, novel piezoceramic based transducers are being researched and tested in the field of structural health monitoring. Along with the development of piezoceramic transducers in structural health monitoring, advanced algorithms using time-domain analysis, frequency domain analysis, and energy based analysis, and impedance measurements are being developed. However, the full potential of piezoceramic transducers in structural health monitoring is yet to be explored. Taking advantages of piezoceramic materials, this dissertation mainly explores innovations in piezoceramic based health monitoring of various structures.

1.1 Motivations and Objectives

Piezoceramic material is fragile and not suitable for direct field application. A new technology called “smart aggregate” was recently developed [1] [2]. In the smart aggregate, a piezoceramic transducer, often in form of a patch, is sandwiched between protection materials, which can be concrete, marble, granite, among others. However, analytical and numerical modeling of the smart aggregate has not been conducted in the past. The first objective of this dissertation is to establish constitutive equations and

obtain the dynamic solutions, including resonance and anti-resonance frequencies of the smart aggregate. Accurate values of resonance frequencies will greatly assist the implementation of piezoceramic based smart aggregates for structural health monitoring.

Many structural failures were initiated by cracks. Recently, pipeline structural health monitoring receives increasing attention. However, the active sensing approach using distributed piezoceramic transducers, though full of potential, has not been reported to monitor the onset and the severity of cracks in a pipeline. It is an objective of this dissertation to explore the crack monitoring of pipelines by using piezoceramic based active sensing approach. On the other hand, concrete structures, under earthquake excitations, are prone to crack development. Monitoring of cracks in concrete structures has been researched in the past, however, few research focus on the monitoring of the opening and closing of cracks subject to dynamic loads. It is also an objective of this dissertation to address such a challenge by using embedded smart aggregates and the active sensing approach.

Steel plate reinforced concrete is a newly emerged concrete structure which is formed by sandwiching the concrete structure between two steel plates with reinforcement. However, the study of debonding detection, especially to the early detection, between the steel plates and the concrete has not received much attention. It is an objective of this dissertation to investigate the detection of bond slip between the steel plates and concrete using smart aggregates.

Concrete structures are often used as underground containment for nuclear materials. Cracks and underground water are a lethal combination to migrate the

radioactive pollutant. Additionally, liquid in concrete cracks may erode the rebar and reduce the carrying capacity of the concrete. It is therefore important to detect the liquid presence in concrete cracks. An objective of this dissertation is to develop an effective approach to detect concrete cracks and to further detect the liquid presence in these cracks.

The carrying capacity of concrete is highly influenced by the early age concrete hydration process, especially in the very early age (0-20 hours), when concrete is under intensive reaction. Monitoring of the very early age concrete hydration process is of great importance. It is an objective for the dissertation to develop a novel wave propagation based method to monitor the very early age hydration process and identify different concrete stages.

Soil freeze-thaw condition plays an important role in structural soil interaction in cold regions. The traditional methods to monitor the soil freeze-thaw condition are temperature measurement and field sample analysis. Wave propagation energy is highly sensitive to the mechanical properties of soil during the freezing and thawing process. However, this principle has not been utilized to monitor soil freezing and thawing in the literature. It is therefore an objective for this dissertation to develop an active sensing approach to quantitatively characterize the soil freezing and thawing process.

1.2 Contributions

In this dissertation, theoretical and experimental investigations in the modeling of the piezoceramic based smart aggregate were conducted, as shown in Chapter 3. Constitutive equations and dynamic equilibrium equations for a smart aggregate were

established for the first time. Through analytical and numerical methods, values for resonance frequencies were obtained and the results are in good agreement with the experimental ones.

This dissertation developed an active sensing approach using distributed piezoceramic based transducers to detect cracks and monitor the crack development in pipelines, as shown in Chapter 4. This method also provides a possibility to locate the crack through the appropriate deployment of sensors. Another contribution in Chapter 4 is the monitoring of crack open-close condition of concrete structures using embedded smart aggregates. A wavelet packet-based structural damage index has the potential to offer appreciable values to determine if the crack is opening or closing.

Early detection of bond slip between two layers is a challenge to engineers. This dissertation developed an active sensing approach using smart aggregates to detect the bond slip initiation and development, as shown in Chapter 5. A wavelet packet-based structural damage index is perfectly capable of detecting the bond slip in initial stage and providing reliable values to monitor the further development of the bond slip condition.

This dissertation developed a smart aggregate based active sensing approach to detect cracks and the further water presence in those cracks of concrete structures, as shown in Chapter 6. A wavelet packet-based energy analysis of sensor signal was proposed to identify three status, including health status, crack existence, and water in cracks, of concrete structures. This investigation is significant to provide a prompt warning of material migration from underground containment for nuclear materials.

The quality of the concrete hydration process, especially in the very early age (0-20 hours) partially influences the carrying capacity of concrete structures. An effective and accurate monitoring of the very early age concrete hydration process is highly in demand. This dissertation explored an active sensing approach to identify three stages, liquid stage, transition stage, and hardened stage of the very early age concrete hydration process, as shown in Chapter 7. A comparison study of concrete hydration monitoring using compressive mode and shear mode smart aggregates was investigated. The method mentioned in this chapter is also qualified to monitor the full process of concrete hydration from 0 to 28 days.

This dissertation also proposed a wavelet packet-based approach to quantitatively monitor soil freeze-thaw process by using smart aggregates. The soil freeze-thaw process can be detailed presented in the wavelet packet-based energy vector analysis. Further, a wavelet packet-based soil frozen index is capable of quantitatively characterizing the cyclic soil freezing and thawing process.

1.3 Organization

This dissertation is organized into 9 chapters, with details shown in below.

Chapter 1 describes the background, motivations and objectives, contributions, and organization of this dissertation.

Chapter 2 provides introduction and literature reviews of advanced technical fields related to structural health monitoring. Smart aggregate transducers and their applications in structural health monitoring are introduced. An introduction to wavelet packet-based structural damage index is also included in this chapter.

In chapter 3, firstly, a theoretical mode of the smart aggregate was proposed. Constitutive equations and related basic equations of the smart aggregate were established. Consequently, the dynamic solution of the smart aggregates was derived and the resonance frequencies of smart aggregate samples were computed. The numerical simulation was performed to investigate the influence between the computed resonance frequencies and the scale-factor errors of the smart aggregates. An experimental verification was performed and the results are in good agreement with the theoretical ones.

In chapter 4, a literature survey of structural crack monitoring is presented. The smart aggregate based active sensing approach for structural crack monitoring is introduced. An experiment of crack detection of a pipeline using piezoceramic based transducers was first investigated. The experimental results proof the feasibility of both the crack initiation detection and further development monitoring using active sensing approach. Another experiment of crack open-close monitoring of a concrete column was also investigated. The experimental results demonstrate that the wavelet packet-based structural damage index successfully monitors the crack opening and closing process under the pseudo-dynamic load.

In chapter 5, steel plate reinforced concrete structures are introduced. An active sensing approach using smart aggregates for bond slip detection is shown in details. Two steel plate reinforced concrete beams were investigated. The bond slip condition was presented in a wavelet packet-based structural damage index. The experimental results show that the active sensing approach using smart aggregates has the ability to monitor

the bond slip between steel plates and concrete. This method offers an early detection of bond slip and a continuously monitoring of its severity.

In chapter 6, previous literatures of crack detection and water detection are reviewed. A smart aggregate based active sensing system is demonstrated to detect concrete crack and the further water presence. Two simple experimental verifications were performed using smart aggregates. Further, an experiment of a concrete beam with three embedded smart aggregates was investigated. Based on the wavelet packet-based energy analysis, the developed smart aggregate based active sensing system is capable of detection the concrete crack and the further water presence in the crack.

In chapter 7, previous researches of the very early age concrete hydration are introduced. Then, an innovative wave propagation based method using smart aggregates and related principles are presented. The proposed method was first investigated in a concrete beam. Three stages during the very early age concrete hydration process were identified: liquid stage, transition state, and the hardened stage. Additionally, a comparison study of the proposed method in concrete hydration monitoring with different modes of smart aggregates was experimentally researched in a small-scale concrete beam.

In chapter 8, literatures related to soil freeze-thaw monitoring are reviewed. An innovative active sensing approach and soil frozen index are presented. Two different sizes of soil specimen were investigated. The experimental results from both specimens are in good agreement which proofs the reliability of the proposed method for soil freeze-thaw monitoring.

Chapter 9 concludes the dissertation and also recommends future work.

2 Introduction to structural health monitoring

In the recent decades, structural failures and collapses have caused casualties and economic loss all over the world. On August 1, 2007, the I-35W Mississippi River Bridge suddenly collapsed, killing 13 people and injuring 145. The National Transportation Safety Board (NTSB) announced the reason that the gusset plates' structure was failed due to the additional weight on the bridge. On June 5, 2013, a neighboring building under demolition collapsed at the southeast corner of the 22nd and market streets in Philadelphia. The accident caused 6 death and 14 injuries. On April 24, 2013, an eight-story building of Rana Plaza collapsed in Savar, Bangladesh. 1129 people died and more than 2500 injured in that accident **Error! Reference source not found.** The structural failures and collapses all around the world emphasize the importance of the early warning and detection of damage based on real-time monitoring of the structure of interest. The discipline of structural health monitoring has received increasing attention in the past twenty years.

2.1 Definition of damage

In the study of structural health monitoring, the word “damage” which often appears in most of the related studies, has to be clarified first. In most cases for engineering fields, damage is referred as changes, including geometric characteristics, material properties and boundary conditions, which affect a system or a structure to behavior as undesirable performance in current or future state [4]. Take an example of the

geometric property change, a crack, which occurs in a structure and alters the structural geometric characteristic, can adversely decrease the carrying capacity of the structure.

Generally, damage identification is based on at least two different states. One is the undamaged state, representing the initial condition of a structure or a system which is always considered as health state. Another one is the damaged state, which is identified by the changes of features measured and compared to the initial undamaged state. In addition, except the damage identification, a comprehensive analysis of the damage including the location, severity, and the development, is also required to be well addressed.

In the past decades, before structural health monitoring appeared, visual inspection (hands-on inspection) is a traditional and fundamental method to report damages for civil infrastructures, which include buildings, transportation systems, energy generation and distribution systems, etc. In visual check, structural damage (e.g. cracks, bond slip, and erosion) is always checked by in-situ trained inspectors. A study organized by Federal Highway Administration's Nondestructive Evaluation Validation Center (NDEVC) was investigated to compare the performance 49 inspectors from 25 state departments of transportation in their visual damage detection [5]. However, the quality of visual check method highly depends on the experience of the inspectors. In addition, visual inspection is not a real-time and long term monitoring. With the development of science and technology, structural health monitoring has become a popular discipline field for engineers. Numerous techniques with various implemented transducers, feature

extraction characteristics, and advanced signal processing methods have been researched and developed to structural health monitoring [6][7].

2.2 Implemented transducers

2.2.1 Strain gauge sensor

Strain gauge sensor is a conventional sensor to measure structural local strain which can be used to monitor and evaluate the structural health [8]. The strain gauge sensor was invented by Edward E. Simmons and Arthur C. Ruge in 1938 [9]. When the object is deformed, the deformation of the foil in the strain gauge sensor will cause the change of electrical resistance, which can be measured and represent the change of the strain. Choi *et al.*, integrated the traditional strain gauge sensor with wireless sensor nodes which can overcome the limitation of wire based strain gauge sensor [10]. Recently, Pecora *et al.*, presented a new type of strain gauge sensor using conductive thermoplastic nanocomposite material. The proposed strain gauge sensor is flexible and stretchable which has potential applications of inflatable structures [11]. The strain in the local structure is an interest feature for engineers to determine the damage and structural failure.

2.2.2 Fiber Optic sensor

Fiber optics has been widely used in sensing due to the versatile properties of light [12]. Fiber optic sensors provide excellent properties, such as high resolution, electromagnetic immunity, and small size, which are suitable for applications in structural health monitoring. The intensity, phase, wavelength or time delay of the light

can be measured and utilized to quantize the change of the strain or temperature of the target. Various applications in structure health monitoring using fiber optic sensors have been reported [13][14]. Based on different detection purpose of structures, fiber optic sensor can be specific designed and calibrated to measure the temperature of the environment [15], local strain of a structure [16], moisture and humidity of an area [17].

2.2.3 *Piezoceramic based transducer*

Piezoceramic materials belong to piezoelectric materials which have the property of piezoelectricity [18]. Due to the piezoelectricity, distributed piezoceramic based transducers are capable of performing as both actuators and sensors to excite and detect the dynamic motion of the structure. In addition, piezoelectric transducers can also be used as ultrasonic wave transmitter and receiver in wave based structural health monitoring. Researchers have developed various of sensing methods in different applications of structural health monitoring, including early age concrete hydration monitoring [1], damage detection of reinforced concrete frame under simulated earthquake [19], interface inspection between corroded steel bars and concrete [20], crack detection of composite reinforced concrete walls [21], impedance based damage assessment of the pipeline structure [22], crack detection under the impact behavior using piezoceramic based smart aggregates [23].

2.3 Feature extraction and information condensation

In the process of structural health monitoring, feature extraction is a most common and effective method to identify the damage. Most data features are obtained

from the structural dynamic response and the damage-sensitive features will be extracted and analyzed associated with information condensation. Compared to the undamaged state of the structure, the change of the data features is referred to some damage in the structure [24]. In recent years, some new features and techniques based on the piezoelectric transducers received increasing attentions, including impedance measurement and wave propagation based data features.

2.3.1 Dynamic response characteristics

In most cases, dynamic response characteristics of a structure or a system change subject to damage. Various methods have been developed to structural health monitoring by measuring or deriving from the dynamic response characteristics, including resonant frequency, damping ratio, stiffness, mode shape, and frequency response function. The details are shown below:

2.3.1.1 Resonant frequency and mode shape

The change of resonant frequencies can be considered as an effective index to evaluate the structural health condition. Zak *et al.*, investigated the relationship between resonant frequencies and delamination length of an eight-layer composite plate [25]. In the numerical simulation supported by finite element formulation, the resonance frequencies increase as the delamination length grows. The conclusion was verified by an experimental test using eight-layer composite plates. Messnia *et al.*, developed single damage detection into multiple damage detection associated with different damage levels by analyzing the changes of the structural natural frequencies. A truss structure was numerically studied using Multiple Damage Location Assurance Criterion (MDLAC) and

multiple damage location can be determined [26]. Stanbridge *et al.*, used Continuously-Scanning Laser Doppler Vibrometer (CSLDV) to find the mode shapes of three different flat plates: one defect-free, one with a saw-cut, and one with a fatigue crack. The mode shapes of those three flat plates were clearly distinguished which proved the feasibility of damage detection based on mode shapes [27].

2.3.1.2 Damping

Damping is considered as an ability to reduce the oscillation of a structure or a system. The change of the structural or system damping can be also referred as damage occurs [28] [29]. Keye *et al.*, developed a method to detect the damage on the carbon-fiber-reinforced polymer used in aircraft panel. Through measuring the modal damping parameters, the damage can be located [30]. In the measurement of specific damping capacity (SDC), Kyriazoglou *et al.*, detected the initial damage in woven fabric composites [31].

2.3.1.3 Frequency response function

Frequency response function method is based on the measurement range to all frequencies, not just the modal frequencies. The advantage of this method is the capability of providing frequency response at different locations of the structure with appropriate sensor distribution [32]. Bandara *et al.*, developed an artificial neural networks trained with summation frequency response functions. The method was experimentally investigated using a three-story bookshelf structure. In a good agreement of the experimental results, the proposed method has shown potentials to detect the nonlinear damage of structures [33].

2.3.2 New features and techniques

2.3.2.1 Impedance measurement

Electromechanical impedance (EMI) technique using piezoceramic based transducers has been researched for many years [21] [34] [35]. A conventional method to detect structural damage or identify related parameters is to measure the impedance of surface bonded piezoceramic based transducers [36]. Associated with some advanced statistical approaches [37], the structural damage severity and the change of material property can be quantitatively characterized [38]. The EMI technique with piezoceramic based transducers for structural health monitoring has been widely used to detect damage crack [39], early age concrete hydration [40], strength gain in concrete [41], etc.

2.3.2.2 Wave propagation based detection

2.3.2.2.1 Passive sensing method

Passive sensing method associated with passive sensors aims to sense the signal from objectives without any energy input need. The advantage of passive sensing is such passive methods can save energy for passive sensing especially for some harsh environment where continuous and reliable energy is hard to supply. Passive sensing methods for structural health monitoring have been used for many years [42] [43] [44].

Acoustic emission (AE) is commonly used as a passive sensing method to measure the microscope movements of structures. When a crack occurs as well as some other damage in a structure, the damage event induced energy will propagate in the structure in terms of stress wave [45]. The stress wave energy will be sensed by distributed acoustic emission sensors attached to the structure and be utilized to

characterize the damage event of a structure [46]. Lingard *et al.*, presented his exploratory work in detecting the sliding motion using acoustic emission. Both unlubricated and with elastohydrodynamic lubrication conditions were investigated. The relationship between the AE signal and deformation in the contact zones was characterized. [47]. Carpinteri *et al.*, applied acoustic emission technique to monitor the structural health based on counting events due to the damage. In addition, he developed a statistical and fractal analysis to describe the behavior of quasi-brittle material in compression [48]. Farhidzadeh *et al.*, monitored the fracture process of a reinforced concrete shear wall due to cyclic loading. A *b*-value analysis Gaussian filter was investigated to measure the crack propagation. Contributed by a cluster analysis based on the *k*-means, tensile and shear cracks can be classified automatically [49].

Passive impact damage detection has been studied over many years [50]. Choi *et al.*, deployed distributed piezoelectric sensors into a beam and investigated an identification system consists of a system model and a response comparator to identify the impact load and location [51]. Song *et al.*, embedded piezoceramic transducers in a model concrete bridge girder and successfully detect the level of damage due to a collision impact. A linear relation between the output of sensor energy and the impact energy was found [23]. Pedemonte *et al.*, presented detected the impact damage in a composite structure using advanced signal analysis including time domain analysis, frequency domain analysis, and wavelet domain analysis [52]. Consequently, Staszewski *et al.*, presented a modified multilateration procedures with Genetic Algorithms to locate the position of an impact for a composite aircraft structure [53].

2.3.2.2.2 Active sensing method

Comparing to passive sensing mentioned above, active sensing method benefits from the controllable probing signal which can be defined with appropriate intensity, frequency, length, and direction. At the meanwhile, distributed sensors are utilized to detect the received signal from the probing signal propagated from structures or environment. The related information obtained from the detected signal can be an assessment to identify the target, structure, or environment in different applications.

Radar is a good example using active sensing method. The radar dish or antenna generates radio waves to air and the radio waves are bounced off from objects when they are in the wave path. The received wave energy by the objects will be utilized to determine the location, dimension, and even the shapes of the targets.

Piezoceramic transducers are commonly used in active sensing method due to their exceptional piezoelectricity. Researches applied the active sensing method using piezoceramic transducers to structural health monitoring for various civil structures [54] [55]. The structural damage or material properties can be identified by the associated signal detected by the distributed sensors. Active sensing method is more flexible to predict and detect the structural damage with pre-determined probing signal and sensor location [56].

Wang *et al.*, developed the active sensing approach to monitor the bolted structures. A wavelet packet based damage index was presented to looseness of a bolt. The looseness degree of the bolt was quantitatively characterized by the values of the bar shown in the damage index [57]. Wang *et al.*, also studied bolt lessening using active

sensing approach with piezoceramic patches. The degree of bolt lessening was presented by the calculated signal energy [58]. Ruan *et al.*, presented his recent research to detect the damage of a wind turbine blade. An energy analysis and an innovative polar plot analysis were applied to develop a relationship between sensor signal and crack depth [59]. Du *et al.*, attached several piezoceramic patches on a pipeline segment to detect the crack severity using wavelet packet-based damage index. The increasing depth of the crack was successfully identified corresponding to the increasing values shown in the wavelet packet-based damage index [60].

2.4 Advanced Signal processing methods

2.4.1 Wavelet packet-based analysis

Wavelet packet analysis is widely used in mathematics, signal processing, image processing, quantum mechanics, and theoretical physics, etc. Chui *et al.*, first introduced his recent research related to wavelet [61]. Comparing to the tradition Fourier Transform, wavelet packet technique is a localized analysis in time-frequency of the signal [62]. The wavelet packet analysis can realize the time decomposition at high frequency and frequency decomposition at low frequency. The signal can be specifically characterized based on wavelet packet analysis [63]. A decomposition tree based on wavelet package analysis is shown in Figure 2-1.

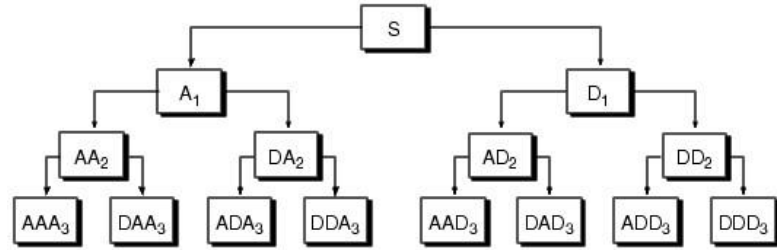


Figure 2-1 Decomposition tree of wavelet package analysis

Wavelet packet analysis decompose original signal into 2^n set of signal which has n scale or level. As shown in Figure 2-1, the signal is first decomposed by a low frequency band (A) and a high frequency band (D). The first step is marked as level 2. Then for level 3, each frequency band is continuously decomposed into a low frequency and a high frequency band, respectively. According to the demand in use, the signal will be eventually divided into 2^n level. Each frequency band is a wave packet of the original signal.

Wavelet packet analysis has been considered as a promising tool for structural health monitoring. Based on the wavelet analysis, cumulative damage of a building subjected to a real earth quake excitation was deeply studied [63]. The knowledge of wavelet packet analysis was also applied to detect the early faults of gear systems. The damage of the gear system can be presented by the particular frequency band through the signal decomposition [64][65]. Moreover, effects of noise contamination and the evaluation of the damage severity of structures were investigated [66] [67].

2.4.2 Polar plot analysis

Polar analysis is an advance signal process tool to characterize the signal in polar coordinates. In wave based active or passive sensing approaches, the properties of the

propagated wave are associated with the structural damage. When the structure is subject to a crack, notch, or a bond slip, the magnitude and the phase of the propagated wave or received wave from sensors will significantly change corresponding to the damage. Such damage can be clearly presented by an appropriate polar analysis [68].

Polar analysis has been applied to structural health monitoring due to its exceptional ability of presenting the change of the signal phase. Zhu *et al.*, developed the polar analysis into evaluating the effects of heading angle on the structural safety [69]. The original reliability and redundancy indices processed from the SHM data were directly presented in the polar coordinate which offered straightforward indicators to help ship operators in adjusting the speed and heading angles. Michaels *et al.*, experimentally simulated a fastener hole in an aluminum plate specimen shown in acoustic wavefield images. The polar results successfully polished the original data and helped to determine the scattering pattern [70].

2.4.3 Time reversal technique

Time reversal technique was firstly proposed by Fink [71]. Time reversal technique can focus ultrasound, electromagnetic waves spatially and temporally in both homogeneous and non-homogeneous environment. In a randomly inhomogeneous media, time reversal technique gives a solution to overcome the complex influence of multi-pathing problem and provide an accurate signal focusing on targets [72]. Therefore, time reversal technique is applicable in detecting targets (i.e. crack, void) for structural health monitoring [73]. Park *et al.*, integrated time reversal technique with wavelet-based signal processing technique to identify defects on a quasi-isotropic composite plate. Without

any past data as baseline, the defects can be directly found and located [74]. Taking the advantage of the temporal and spatial focusing from time reversal technique, a considerable noise can be eliminated. Time reversal technique has a potential ability to provide an image based damage detection [75].

2.4.4 Canonical variate analysis

In some fields of structural damage detection especially for vibration-based detection, the sensor data especially obtained from vibration-based detection is subject to the high mode density. Canonical variate analysis (CVA) can be utilized to distinguish the high modes of the signal [50]. Canonical variate analysis has been experimentally investigated and proved to be a valid tool for extracting high modes from a signal [76][77]. Marchesiello *et al.*, presented the mode shapes of the data related to the Z24 bridge location in Canton Bern using Canonical variate analysis. Implemented with Modal Assurance Criterion (MAC), the canonical variate analysis automatically extracts modal parameters of the data [78]. The canonical variate analysis was considered as a reliable method for structural health monitoring with unknown input.

2.5 Piezoceramic transducers

Piezoelectric ceramics belong to the group of ferroelectric materials. The word “Piezo” is derived from the Greek word for pressure. The piezoelectric properties were first experimentally demonstrated by Columnre Curie and Jacques Curie in 1880 using quartz crystals. Later, people called them as Direct Piezo Effect and Inverse Piezo Effect. The piezo effect exhibited by natural materials such as quartz, tourmaline, Rochelle salt,

etc. is very small. Polycrystalline ferroelectric ceramic materials such as BaTiO₃ and Lead Zirconate Titanate (PZT) have been developed with improved properties. PZT crystallites are centro-symmetric cubic (isotropic) before poling and after poling exhibit tetragonal symmetry (anisotropic structure) below the Curie temperature, as shown in Figure 2-2 [79].

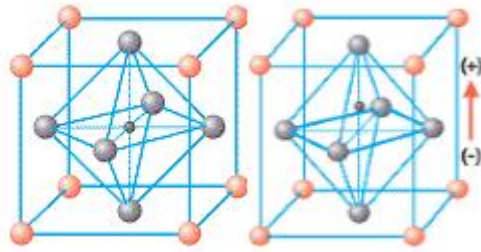


Figure 2-2 Piezoelectric elementary cell (1): Before poling (Left) (2): After poling (Right)
Mechanical stresses arising as an external force applying to the piezoelectric

material will induce displacement along the poling direction. This is called the direct piezo effect. The direct piezoelectric effect is frequently referred to as the generator effect in the literature. An electric field applying to the piezoelectric material will generate a stress or strain. This is called the inverse piezo effect. The inverse piezoelectric effect is frequently also called the motor effect. Due to the electromechanical property of the piezoelectric material, piezoceramic based transducer can be used as an actuator, as well as a sensor [80].

Lead zirconium titanate (PZT) is one of the most common used piezoelectric material and can be cut into small sizes as piezoceramic patches. If the poling direction of the piezoceramic patch is 3-direction, which is the same direction with the electric field, as shown in Figure 2-3, piezoelectricity [81] is presented mathematically by the material's constitutive equation shown as

$$D_3 = e_{33}\varepsilon_3 + k_{33}^\varepsilon E_3 \text{ and} \quad (2-1)$$

$$\sigma_3 = C_{33}\varepsilon_3 - e_{33}E_3, \quad (2-2)$$

where σ_3 and ε_3 are the stress and strain components of the piezoelectric material along the 3-direction, respectively; D_3 and E_3 represent the electric displacement and electric field in the same direction, respectively; the coefficients are $C_{33P} = 1/S_{33P}$, $e_{33} = d_{33}/S_{33P}$ and $\kappa_{33}^\varepsilon = \kappa_{33}^\sigma - d_{33}^2/S_{33P}$, where S_{33P} , d_{33} and κ_{33}^σ are the elastic coefficient, piezoelectric coefficient and permittivity coefficient, respectively.

In case of being used as a sensor, the applied external electric field is zero. The relationship between electric displacement and generated charge can be expressed as

$$q = \iint [D_1 \quad D_2 \quad D_3] \begin{Bmatrix} dA_1 \\ dA_2 \\ dA_3 \end{Bmatrix}, \quad (2-3)$$

where dA_1 , dA_2 , and dA_3 are the components of the electrode area.

The compression mode of a PZT patch is shown in Figure 2-3. Suppose that 3-direction is the main stress direction.

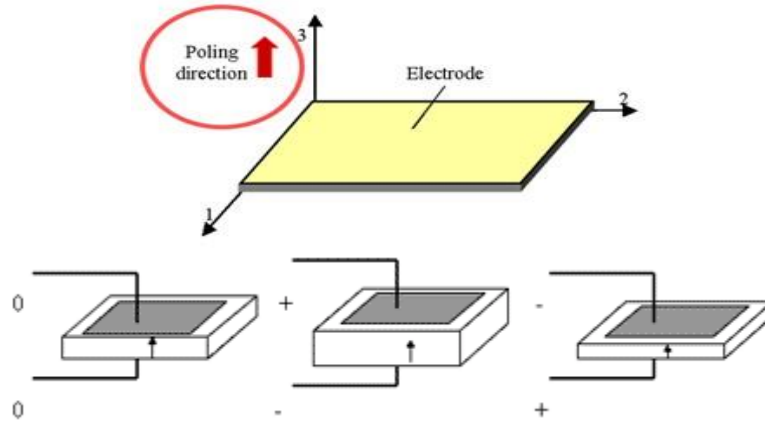


Figure 2-3 PZT patch in compression mode

For shear mode of a PZT patch is shown in Figure 2-4. The main stress direction is along the 3-direction.

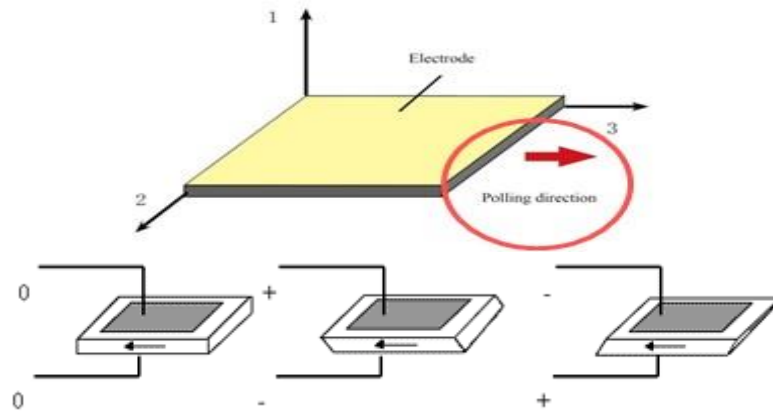


Figure 2-4 PZT patch in shear mode

2.6 Smart aggregate transducer

2.6.1 Introduction to smart aggregate

2.6.1.1 First generation of smart aggregate

In order to protect the fragile PZT patch, a smart aggregate (SA) is introduced. The first generation of smart aggregate is designed by casting a piezoelectric patch with lead wires by a concrete block, as shown in Figure 2-5 [1].

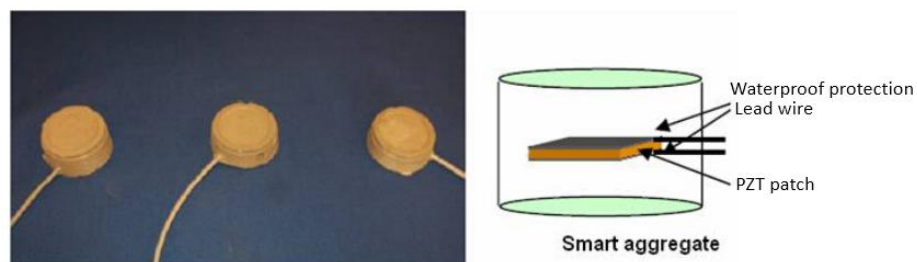


Figure 2-5 First generation of smart aggregate and its structure

The first generation of smart aggregate casts the original fragile PZT patch with a concrete, which dramatically increases its survivability comparing to the naked PZT

patch. Therefore, smart aggregates can be used as embedded transducers for structural health monitoring.

2.6.1.2 Second generation of smart aggregate

In order to continuously improve the performance of smart aggregates as embedded transducers, the second generation of smart aggregates is proposed [2]. The second generation of smart aggregate is designed by sandwiching a PZT patch between two marble pieces, as shown in Figure 2-6. The mechanical properties of first and second generation of smart aggregates are shown in Table 2-1.

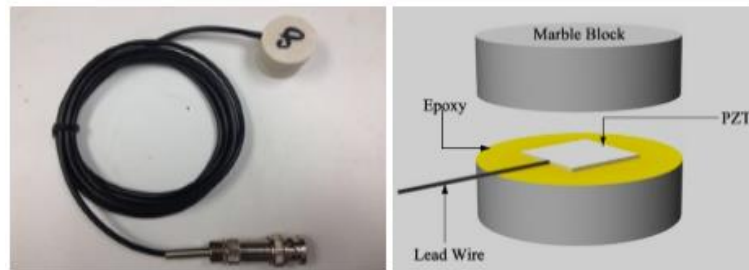


Figure 2-6 Second generation of smart aggregate and its structure

Table 2-1 Mechanical properties of concrete and marble

	Young's Modulus	Compressive strength	Tensile Strength
Concrete	30 Gpa	20-40 Mpa	2-5 Mpa
Marble	50-70 Gpa	200 Mpa	7-20 Mpa

Obviously, the second generation smart aggregates have a greater Young's modulus, compressive strength, and tensile strength than the first generation smart aggregate. The improved mechanical properties promote the second generation smart aggregates to be more suitably embedded in the concrete under large carrying load.

Based on the dimension and properties of test objects, smart aggregates can be made in different sizes. In addition, marble material used in the second generation of

smart aggregate can be replaced by some other materials, such as metal. Figure 2-7 shows different kinds of smart aggregates using concrete, marble, and metal housing. For easy connection, a BNC connector is welded to the end of the leading wire. Please note that all piezoceramic patches receive waterproof treatment.

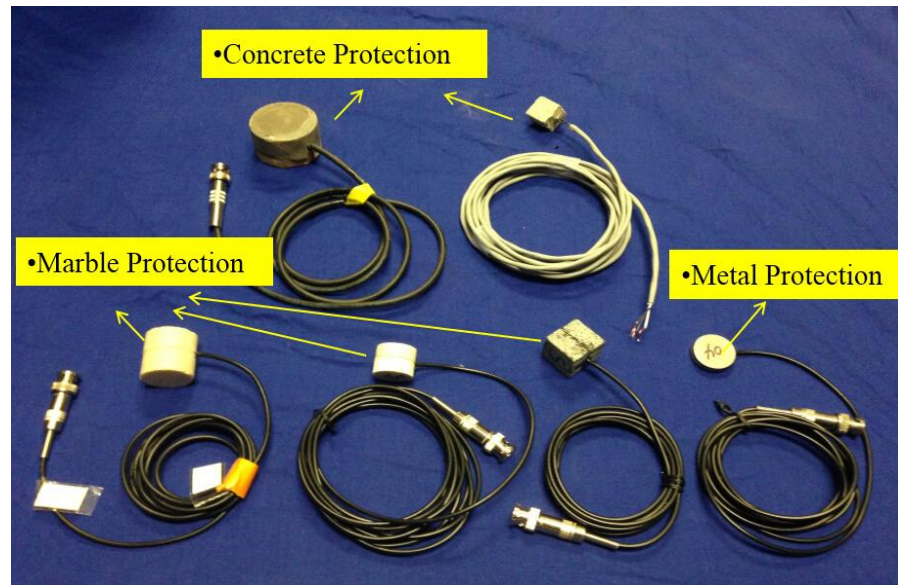


Figure 2-7 Smart aggregates with different protected materials

If the piezoceramic patch is under d_{33} mode, the fabricated smart aggregate is called Compression Mode Smart Aggregate (CMSA). When the smart aggregate is excited by a continuous sinusoidal signal excitation, a corresponding compressive (longitudinal) wave will be generated along the poling direction. On the other hand, a Shear Mode Smart Aggregate (SMSA) can be developed using a d_{15} mode piezoceramic patch and generate shear wave due to the continuous sinusoidal signal excitation.

The advantages of smart aggregates can be concluded as follows:

- (1) Smart aggregate can be perfectly functioned under harsh environment.
- (2) The small size of smart aggregates can be easily installed.

- (3) Due to the composed materials, smart aggregates are low cost sensors.
- (4) Smart aggregate have a long service life.
- (5) Smart aggregates can perform a non-destructive structural health monitoring.

2.6.2 Applications of smart aggregates for structural health monitoring

2.6.2.1 Background

Smart aggregates have been widely utilized as embedded transducers for structural health monitoring. Song *et al.*, proposed active sensing approach and a concrete damage index associated with smart aggregates to concrete structure health monitoring [1]. In various applications using smart aggregates, the concrete crack damage can be detected and the severity of the crack can be characterized [82] [83] [84] [85]; the very early age concrete hydration process can be monitored [86] [87]. Xu *et al.*, applied smart aggregates to detect the active debonding of large rectangular CFSTs and a concrete-filled steel tube. The debonding situation was presented by the wavelet packet analysis [88] [89]. Chung *et al.*, presented the recent research to characterize the hydration process for both concrete and mortar specimens with different water-to-cement using smart aggregates. The initial water-to-cement ratio can be determined by the total power of the received sensor signal [90].

2.6.2.2 Smart aggregate based active sensing approach

As mentioned in Section 2.4.1, smart aggregates are capable of monitoring concrete structure health due to their stable chemical and mechanical properties. In addition, based on electromechanical property of piezoceramic material, smart aggregates can be utilized as both actuators and sensors in an active sensing system. In an active

sensing system, some selected smart aggregates are used as actuators to generate guided signal and the signal is eventually detected by the distributed sensors. The property change of the structure can be assessed based on detected signal associated with different advanced signal process analysis.

2.6.2.2.1 Sinusoidal signal excitation

Sinusoidal signal seems to be one of the most common excitation signal used in active sensing method. One example is the constant frequency sine wave. Figure 2-8 shows a sine wave with the constant frequency of 30Hz. The advantage of the constant frequency since wave excitation is that the signal is easy to generate and analyze if the selected frequency is good enough to realize the test propose.

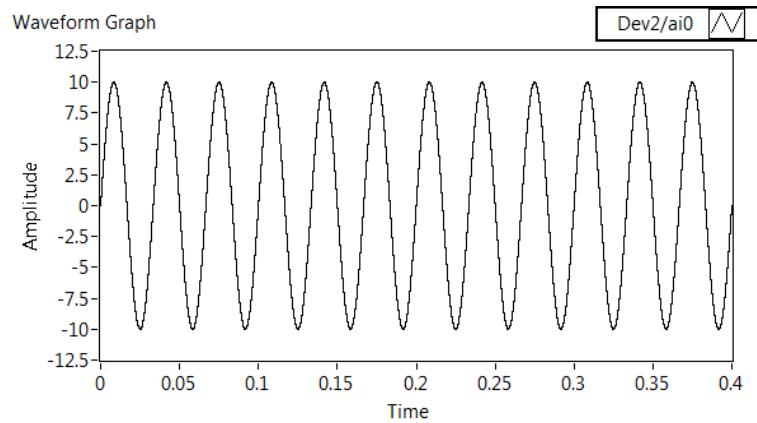


Figure 2-8 A sine wave with the constant frequency of 30Hz

When the structural health condition cannot be determined by a single frequency, a swept frequency sine wave can be utilized as another excitation signal. Different from a constant frequency signal, a swept frequency signal has a frequency range. Figure 2-9 shows an example of a swept frequency signal. The start frequency is 10Hz and the stop

frequency is 1000Hz. The period of the signal is 1s. In order to see clearly of the frequency change, only the first 0.4s of the signal is picked up in the figure.

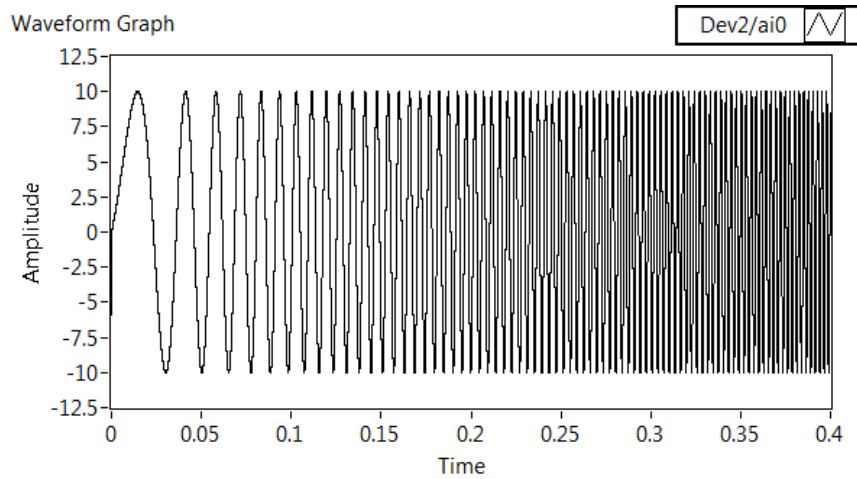


Figure 2-9 an example of a swept frequency signal

In some cases, appropriate constant frequency signal and swept frequency signal can be applied to monitor the structure together. Different excitation signal can complete different tasks in monitoring the particular structural damage.

2.6.2.2.2 Two smart aggregated based active sensing system

2.6.2.2.2.1 Experimental setup and procedures

In order to verify smart aggregates to be suitable in active sensing system, a preliminary experiment of a two smart aggregates based active sensing test was conducted. Two smart aggregates were firstly stick together using a thin layer of super glue, as shown in Figure 2-10. Smart aggregate (1) is used as an actuator and smart aggregate (2) is used as a sensor. Since the two smart aggregate is bonded, the stress wave can propagate directly from the actuator to the sensor. A small piece of foam was placed under the smart aggregates to avoid the signal energy attenuates from the bottom contact. A data acquisition system (NI USB 6363) and a laptop were used to generate

excitation signal and receive the signal response. The sampling rate of the data acquisition system is 1MS/s. The experimental setup is shown in Figure 2-10 and Figure 2-11.

In the experiment, smart aggregate (1) was sending repeated swept sine signal to smart aggregate (2) and the received signal was continuously recorded. A swept frequency sine wave is applied to the test. The start frequency is 100 Hz and the stop frequency is 150 KHz. The period of the swept sine wave is 1s and the amplitude is 10V.

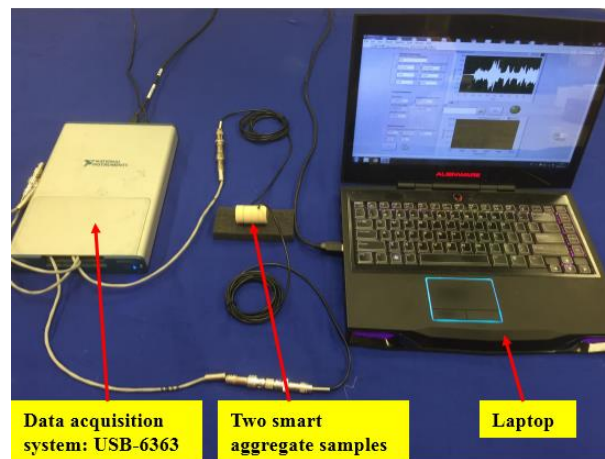


Figure 2-10 Experimental setup of an active sensing test using smart aggregates

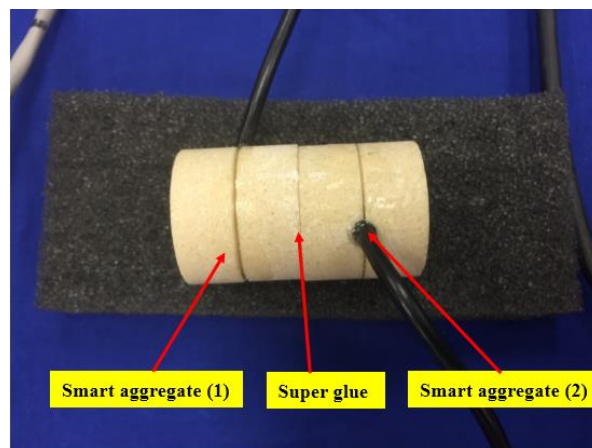


Figure 2-11 A zoom in photo of two bonded smart aggregates

2.6.2.2.2 Experimental results and discussions

Figure 2-12 shows the received sensor signal for a period of 1s. The X-axis corresponds to the samplings and the Y-axis corresponds to the sensor voltage. Since the sampling rate of the system is 1Ms/s, the length of X-axis corresponding to time is exactly 1s which is just one period of the excitation swept frequency signal. The power spectrum of the sensor signal for one period is also calculated, as shown in Figure 2-13. It can be clearly found that the magnitude of the received sensor signal is related to the excitation frequency from the actuator.

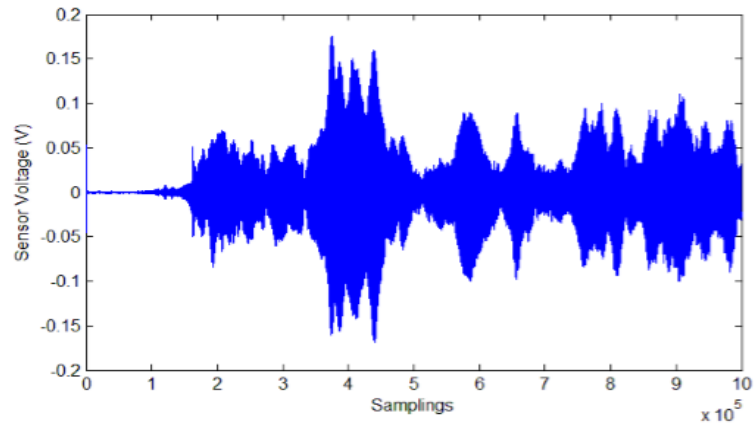


Figure 2-12 Received sensor signal from the actuator

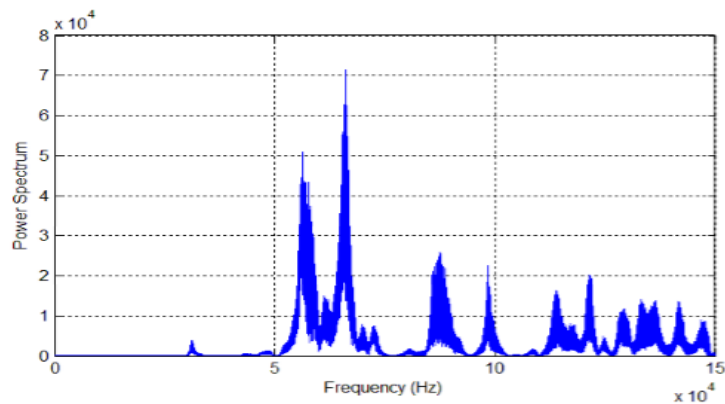


Figure 2-13 The power spectrum of the sensor signal

From the experiment, several conclusions can be obtained as follow:

- 1) Active sensing method using smart aggregates is feasible.
- 2) The stress wave can propagate through smart aggregate in a wide high frequency range.
- 3) The receive signal strength is high sensitive to the excitation frequency.

2.7 Structural damage index

A wavelet packet based structural damage index is developed. A structural damage index is calculated based on root-mean-square (RSMD) method with derived different wavelet packets [91] [92]. In the application of structural health monitoring using smart aggregates, the received sensor energy is an important indicator used to evaluate different conditions of structural damage.

Mentioned in Section 2.5, a sensor signal S can be decomposed by n -level wavelet packet into 2^n signal sets $\{X_1, X_2 \dots X_{2^n}\}$. E_j is the energy of the decomposed signal, and j is the frequency band ($j= 1 \dots 2^n$). X_j is the decomposed sensor signal, which can be expressed as

$$X_j = [X_{j,1}, X_{j,2}, \dots, X_{j,m}], \quad (2-4)$$

where m is the number of data samples. Additionally, the energy of the decomposed signal is defined as

$$E_j = X_{j,1}^2 + X_{j,2}^2 + \dots + X_{j,m}^2. \quad (2-5)$$

According to the data from different measured time i , the signal energy vector at time i is defined as

$$E_i = [E_{i,1}, E_{i,2}, \dots, E_{i,2^n}]. \quad (2-6)$$

A structural damage index can be defined by using the developed root-mean-square deviation (RMSD) method [93]. It is shown as

$$I = \sqrt{\frac{\sum_{j=1}^{2n} (E_{i,j} - E_{1,j})^2}{\sum_{j=1}^{2n} E_{1,j}^2}}, \quad (2-7)$$

where $E_{1,j}$ is calculated from the initial data which is always measured in structure health status. The subsequent data is measured after structure health status related to some damage occurred in the test structure.

From the structural damage index, it can be found that when the subsequent data is close to the original data, the value of the damage index is approaching to 0. On the other hand, when the subsequent data is approaching to 0, the value of the damage index is approaching to 1. The structural damage such as crack or bond slip can be regarded as a stress relief in the path of stress wave propagation between actuators and sensors. When the active sensing method is applied to structural health monitoring, the received sensor signal will proportionally attenuate associated with the structural damage degree. Therefore, when the value of damage index is 0, it means the test structure is in a good health condition. However, when the value of damage index is approaching to 1, it means the test structure might be totally failure. When the value of damage index is between 0 and 1, the test structure should be objected by some considerable damage. The degree of damage will be quantitatively presented by the value of the damage index. The larger value of the damage index corresponds to a higher degree of the structural damage.

3 Theoretical and experimental characterization of smart aggregate properties

3.1 Introduction

As mentioned in Section 2.4, smart aggregates are capable of using as embedded transducers to monitor the structure health. Due to the electromechanical property of piezoceramic material, smart aggregate can be utilized as either an actuator or a sensor in an active sensing system. To better understand the electromechanical performance and active sensing system, a theoretical and experimental characterization of smart aggregates and the performance of smart aggregate based active sensing system need to be addressed first. Piezo-elasticity theory has been effectively used to solve the dynamic electromechanical problem for various piezoelectric structures, such as piezoelectric composite stack transducers [94], axially polarized multilayer piezoelectric/elastic composite cylindrical transducers [95], 2-2 cement based piezoelectric transducers [96], piezoceramic/metal sandwich cylindrical transducers [97][98][99][100] and circular cylindrical piezoelectric transformers [101][102][103][104].

In this chapter, a simplified theoretical model is proposed to analyze the electromechanical characteristics of the second generation smart aggregate based on one dimensional linear theory of piezo-elasticity. Firstly, the basic equations for a smart aggregate were established. According to the basic equations for a smart aggregate, the dynamic solution of a smart aggregate subjected to an external harmonic voltage was derived. Then, the electric impedance was calculated, and the resonance and anti-resonance frequency equations were given. In addition, the effects of the thickness of

epoxy between two marbles, the thickness and diameter of the lead zirconate titanate (PZT) patch on the fundamental resonance and anti-resonance frequencies as well as the corresponding electromechanical coupling factor were discussed. , To verify the validity of the proposed theoretical model, an experiment was investigated.

3.2 Basic equations

As shown in Figure 3-1, the fabricated second generation smart aggregates and the schematic are exhibited. The second generation smart aggregate is designed by sandwiching a copper with two PZT patches embedded between a pair of solid and drilled cylindrical marble pieces using epoxy. The two piezoelectric patches are assigned electrically in parallel and mechanically in series. The lead wires soldered at the interface between two PZT patches and the surface of copper package are threaded from the hole drilled at the interface between two marbles.

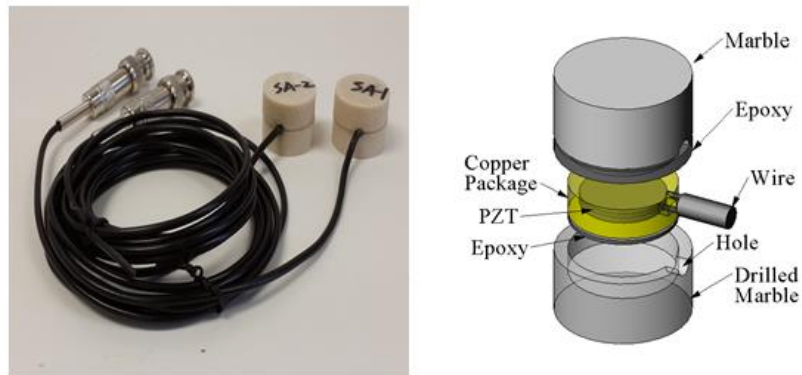


Figure 3-1 Test smart aggregate samples and schematic of a smart aggregate

A simplified model for the second generation smart aggregate is proposed, as shown in Figure 2-2. Symbols M , P , E and C denote the components of Marble, PZT, Epoxy and Copper. The smart aggregate is divided into two pure marble layers (M), one

pure epoxy layer (E), one EM composite layer, two CM composite layers, two PCM composite layers and one CE composite layer. The z -direction is along the thickness of the smart aggregate.

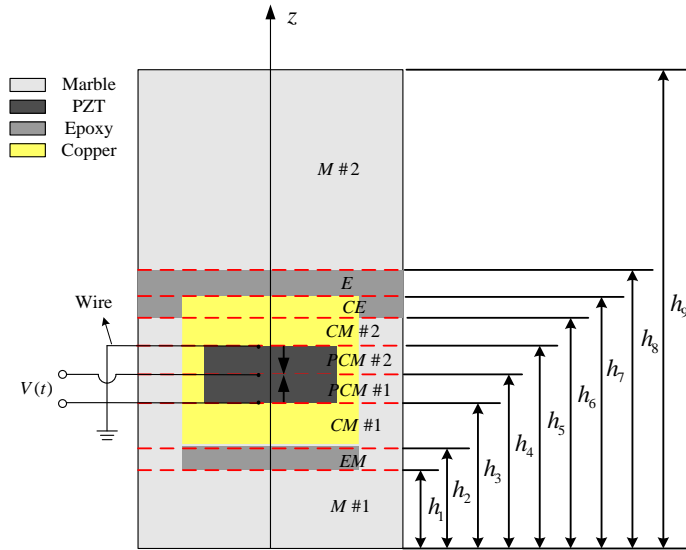


Figure 3-2 A simplified model for a second generation smart aggregate

Since PCM composite layer is the most complicated layer in the smart aggregate. The basic equations of PCM composite layer are first derived. When the basic equations of PCM composite layer are established, the corresponding expressions of EM , CE , CM , M and E composite layers can be obtained, respectively.

3.2.1 Constitutive equations

The constitutive equations of each composed material in PCM composite layer can be written as following:

For PZT patch, the constitutive equation is shown as

$$\begin{aligned}\sigma_P &= C_{33P}\varepsilon_P - e_{33}E_z \text{ and} \\ D_z &= e_{33}\varepsilon_P + \kappa_{33}^\varepsilon E_z .\end{aligned}\tag{3-1}$$

For copper and marble material, the constitutive equations are shown as

$$\sigma_C = C_{33C}\varepsilon_C \text{ and}\tag{3-2}$$

$$\sigma_M = C_{33M}\varepsilon_M ,\tag{3-3}$$

where σ_P and ε_P are the stress and strain components of the piezoelectric material along the z direction, respectively; D_z and E_z represent the electric displacement and electric field in the same direction, respectively; the coefficients are $C_{33P} = 1/S_{33P}$, $e_{33} = d_{33}/S_{33P}$ and $\kappa_{33}^\varepsilon = \kappa_{33}^\sigma - d_{33}^2/S_{33P}$, where S_{33P} , d_{33} and κ_{33}^σ are the elastic coefficient, piezoelectric coefficient and permittivity coefficient, respectively. σ_C and ε_C are the stress and strain components of the copper material along the z direction, respectively; C_{33C} is the Young's modulus of the copper material. σ_M and ε_M are the stress and strain components of the marble material along the z direction, respectively; C_{33M} is the Young's modulus of the marble material.

3.2.2 Geometric relationship equations

The geometric relationship equations of the smart aggregate can be shown as

$$\varepsilon_P = \varepsilon_C = \varepsilon_M = \frac{\partial W_{PCM}}{\partial z} \text{ and}\tag{3-4}$$

$$E_z = -\frac{\partial \phi}{\partial z},\tag{3-5}$$

where W_{PCM} are the displacement components of the composite material layer along the Z direction, respectively; ϕ represents the electric potential in the same direction.

3.2.3 Electrostatic charge equations

The electrostatic charge equation of the smart aggregate can be shown as

$$\frac{\partial D_z}{\partial z} = 0. \quad (3-6)$$

3.2.4 Dynamic equilibrium equations

The dynamic equilibrium equation for axial force in z direction is shown as

$$\frac{\partial N_{PCM}}{\partial z} = [\rho_p S^p + \rho_c (S^c - S^p) + \rho_m S^m] \frac{\partial^2 w_{PCM}}{\partial t^2}, \quad (3-7)$$

where N_{PCM} [$N_{PCM} = \sigma_p S^p + \sigma_c (S^c - S^p) + \sigma_m S^m$] represents as the axial force and S [$S = S^p + (S^c - S^p) + S^m$] is the area of the cross section of the smart aggregate, where S^c is the area of the cross section of the whole copper package; S^p , $(S^c - S^p)$ and S^m are the area of the cross section of the piezoelectric part, copper part and marble part in *PCM* composite layer, respectively; ρ_p , ρ_c and ρ_m are the densities of the piezoelectric material, copper material and marble material, respectively.

The following harmonic external voltage is considered as

$$V(t) = V_0 e^{j\omega t}, \quad (3-8)$$

where V_0 is the external voltage amplitude, j ($j = \sqrt{-1}$), ω ($\omega = 2\pi f$) is the circular frequency, and t is time. For harmonic, steady vibration, the following parameters will change according to the time t , which can be presented as

$$(\sigma_p, D_z, \phi, \sigma_c, \sigma_m, w_{PCM}) = [\sigma_p(z), D_z(z), \phi(z), \sigma_c(z), \sigma_m(z), w_{PCM}(z)] e^{j\omega t}. \quad (3-9)$$

Combine Equation 3-1 to 3-7 and Equation 3-9, yields

$$\begin{cases} w_{PCM}(z) = A_{PCM} \sin k_{PCM} z + B_{PCM} \cos k_{PCM} z \\ N_{PCM}(z) = S[p_{PCM}(A_{PCM} \cos k_{PCM} z - B_{PCM} \sin k_{PCM} z) + \frac{e_{33}^2}{\kappa_{33}^\varepsilon} \chi_1 C_1] \\ \phi(z) = \frac{e_{33}}{\kappa_{33}^\varepsilon} (A_{PCM} \sin k_{PCM} z + B_{PCM} \cos k_{PCM} z + C_1 z + C_0) \\ D_z(z) = -e_{33} C_1 \end{cases}, \quad (3-10)$$

where $k_{PCM} = \omega/V_{PCM}$, $V_{PCM}^2 = C_{33(PCM)}/\rho_{PCM}$, $C_{33(PCM)} = (C_{33P} + 1/\kappa_{33}^\varepsilon) \chi_1 + C_{33C} \chi_2 + C_{33M} (1 - \chi_1 - \chi_2)$, $\rho_{PCM} = \rho_P \chi_1 + \rho_C \chi_2 + \rho_M (1 - \chi_1 - \chi_2)$, $p_{PCM} = C_{33(PCM)} k_{PCM}$, $\chi_1 = S^P/S$, $\chi_2 = (S^C - S^P)/S$. Please note that A_{PCM} , B_{PCM} , C_1 and C_0 are undetermined constants. In k_{PCM} addition, the piezoelectric coefficient will be defined as plus or minus depending on the polarization direction in the positive z -axis or negative z -axis [105].

Similarly, the corresponding expressions of EM , CE , CM , M and E composite layers can be obtained shown as

$$(N_{XY}, w_{XY}) = [N_{XY}(z), w_{XY}(z)] e^{j\omega t} \quad \text{and} \quad (3-11)$$

$$(N_X, w_X) = [N_X(z), w_X(z)] e^{j\omega t}. \quad (3-12)$$

In Equation 3-11, symbol X and Y can be replaced by the combinations of C , M , E , which can express the change of axial force and displacement in z -direction due to the harmonic vibration. In Equation 3-12, symbol X can be replaced by symbol M and E regarding to the other marble layer and Epoxy layer.

The detailed expressions can be further written as

$$\begin{cases} w_{XY}(z) = A_{XY} \sin k_{XY} z + B_{XY} \cos k_{XY} z \\ N_{XY}(z) = S[p_{XY}(A_{XY} \cos k_{XY} z - B_{XY} \sin k_{XY} z)] \end{cases} \quad \text{and} \quad (3-13)$$

$$\begin{cases} w_X(z) = A_X \sin k_X z + B_X \cos k_X z \\ N_X(z) = S[p_X(A_X \cos k_X z - B_X \sin k_X z)] \end{cases} \quad (3-14)$$

where $k_{XY}=\omega/V_{XY}$, $V_{XY}^2=C_{33(XY)}/\rho_{XY}$, $C_{33(XY)}=C_{33X}x_3+C_{33Y}(1-x_3)$,
 $\rho_{XY}=\rho_Xx_3+\rho_Y(1-x_3)$, $\rho_{XY}=C_{33(XY)}k_{XY}$, $x_3=S^C/S$, $k_X=\omega/V_X$, $V_X^2=C_{33(X)}/\rho_X$, $\rho_X=C_{33(X)}k_X$.
 C_{33E} and ρ_E are the Young's modulus and the density of the epoxy material, respectively.
 A_{XY} , B_{XY} , A_X and B_X are the undetermined constants.

3.3 Dynamic solution of smart aggregate

The mechanical and electrical boundary conditions, as well as the continuous conditions, can be written as

$$\begin{cases} N_M^{(1)} \Big|_{z=0} = 0 \\ N_M^{(2)} \Big|_{z=h_0} = 0 \end{cases}, \quad (3-15)$$

$$\begin{cases} \phi^{(1)} \Big|_{z=h_3} = 0 \\ \phi^{(1)} \Big|_{z=h_4} = V(t) \\ \phi^{(2)} \Big|_{z=h_4} = V(t) \\ \phi^{(2)} \Big|_{z=h_5} = 0 \end{cases}, \quad (3-16)$$

$$\begin{cases} w_{EM} \Big|_{z=h_1} = w_M^{(1)} \Big|_{z=h_1} \\ N_{EM} \Big|_{z=h_1} = N_M^{(1)} \Big|_{z=h_1} \\ w_{CM}^{(1)} \Big|_{z=h_2} = w_{EM} \Big|_{z=h_2} \\ N_{CM}^{(1)} \Big|_{z=h_2} = N_{EM} \Big|_{z=h_2} \\ w_{PCM}^{(1)} \Big|_{z=h_3} = w_{CM}^{(1)} \Big|_{z=h_3} \\ N_{PCM}^{(1)} \Big|_{z=h_3} = N_{CM}^{(1)} \Big|_{z=h_3} \\ w_{PCM}^{(2)} \Big|_{z=h_4} = w_{PCM}^{(1)} \Big|_{z=h_4} \\ N_{PCM}^{(2)} \Big|_{z=h_4} = N_{PCM}^{(1)} \Big|_{z=h_4} \end{cases}, \text{ and} \quad (3-17)$$

$$\left\{ \begin{array}{l} W_{CM}^{(2)} \Big|_{z=h_5} = W_{PCM}^{(2)} \Big|_{z=h_5} \\ N_{CM}^{(2)} \Big|_{z=h_5} = W_{PCM}^{(2)} \Big|_{z=h_5} \\ W_{CE} \Big|_{z=h_6} = W_{CM}^{(2)} \Big|_{z=h_6} \\ N_{CE} \Big|_{z=h_6} = N_{CM}^{(2)} \Big|_{z=h_6} \\ W_E \Big|_{z=h_7} = W_{CE} \Big|_{z=h_7} \\ N_E \Big|_{z=h_7} = N_{CE} \Big|_{z=h_7} \\ W_M^{(2)} \Big|_{z=h_8} = W_E \Big|_{z=h_8} \\ N_M^{(2)} \Big|_{z=h_8} = N_E \Big|_{z=h_8} \end{array} \right. , \quad (3-18)$$

where the right superscripts “(1)” and “(2)” are marked as layer number. Please note that both side of smart aggregate in this model are considered as free boundary conditions.

Combine the equations (3-9) to (3-14) into (3-15) to (3-18), 22 equations can be used to solve 22 unknown constants. A set of linear algebraic equations can be obtained as

$$a_{mn}A_\alpha = B_\alpha V_0 , \quad (3-19)$$

where a_{mn} , A_α and B_α can be given by (A.1) , (A.2) and (A.3) in Appendix A, respectively, $m = 22$, $n = 22$.

Thus, 22 unknown constants can be derived as

$$A_\alpha = (a_{mn})^{-1} B_\alpha V_0 . \quad (3-20)$$

Of particular importance are the results

$$C_1^{(1)} = V_0 \frac{|b_{mn}^{(1)}|}{|a_{mn}|} \text{ and} \quad (3-21)$$

$$C_1^{(2)} = V_0 \frac{|b_{mn}^{(2)}|}{|a_{mn}|} , \quad (3-22)$$

where $b_{mn}^{(1)}$ and $b_{mn}^{(2)}$ can be obtained through replacing ninth column and thirteenth column in a_{mn} with B_α , respectively.

The electric current can be determined further by

$$I(t) = -\frac{dQ^{(1)}(t)}{dt} + \frac{dQ^{(2)}(t)}{dt} = j\omega S^P e_{33} \frac{|b_{mn}^{(1)}| + |b_{mn}^{(2)}|}{|a_{mn}|} V_0 e^{j\omega t}, \quad (3-23)$$

where

$$Q^{(1)}(t) = \int_{S^P} D_z^{(1)} dS^P = -S^P e_{33} C_1^{(1)} e^{j\omega t} \quad \text{and} \quad (3-24)$$

$$Q^{(2)}(t) = \int_{S^P} D_z^{(2)} dS^P = S^P e_{33} C_1^{(2)} e^{j\omega t}. \quad (3-25)$$

Furthermore, the electrical admittance \tilde{Y} or impedance Z can be expressed as

$$\tilde{Y} = \frac{1}{Z} = \frac{I(t)}{V(t)} = j\omega S^P e_{33} \frac{|b_{mn}|}{|a_{mn}|}, \quad (3-26)$$

where $|b_{mn}| = |b_{mn}^{(1)}| + |b_{mn}^{(2)}|$. Further, b_{mn} can be simplified through replacing thirteenth column in $b_{mn}^{(1)}$ with $B_\alpha^{(3)}$.

Thus, resonance frequency f_r and anti-resonance frequency f_a are also obtained respectively when $|Z|=0$ and $|Z|=\infty$, as

$$|a_{mn}| = 0 \text{ (Resonance equation) and} \quad (3-27)$$

$$|b_{mn}| = 0 \text{ (Anti-resonance equation).} \quad (3-28)$$

Equation 3-27 and Equation 3-28 are two transcendental equations, which can be solved numerically to get the resonant frequencies. In addition, the electromechanical coupling factor of a structure defined by Mason [106] is adopted as

$$k_d^2 = \frac{f_a^2 - f_r^2}{f_a^2}. \quad (3-29)$$

3.4 Numerical simulations

The structure of the second generation smart aggregate is shown in Figure 3-1. The diameter of the PZT patch is 14.7mm, and the thickness is 0.3 mm. The diameter of the copper package is 18mm, and its thickness is 2.6mm. The diameter and height of every marble block is 24.5 mm and 10 mm, respectively. Besides, a hole was drilled on the bottom of the Marble, and its depth is 2.4mm. The thickness of the whole epoxy between a pair of marbles is 0.5mm. The thickness of the epoxy between the marble and copper package is 0.15mm. The corresponding material properties are listed in Table 3-1.

Table 3-1 Material properties

Material types	P-5H	Copper	Marble	Epoxy
Young's modulus C_{33} (GPa)	46	100	50	3.2
Density(g/m^3)	7.45	8	2.58	1.65
d_{33} (pC/N)	670	~	~	~
$\kappa_{33}^{\sigma} / \varepsilon_0$	4500	~	~	~

$\varepsilon_0 = 8.85 \times 10^{-12} \text{ F/m}$, Permittivity of free space

The above structural sizes and material properties are adopted in the following numerical analysis, unless otherwise stated. During the fabrication of the proposed smart aggregate, it is difficult to keep the thickness of the whole epoxy between two marbles as constant. The influence of the thickness of the whole epoxy on the dynamic characteristics of SA is evaluated by numerical analysis. The thickness of the whole epoxy ranges between 0.4 and 0.8 mm. The analytical results are plotted in Figure 3-3.

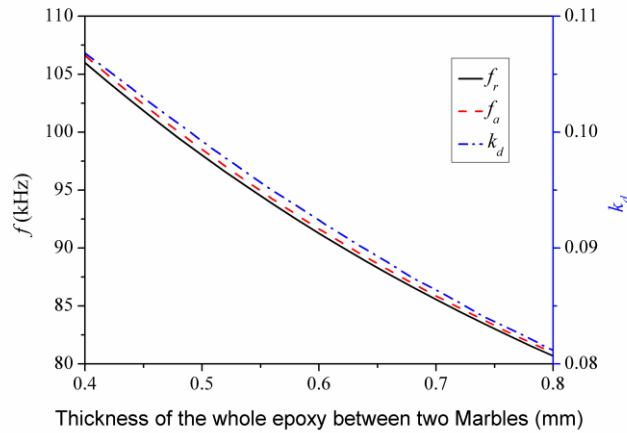


Figure 3-3 The influence of the thickness of the whole epoxy between two Marbles on the fundamental resonance and anti-resonance frequencies as well as the corresponding electromechanical coupling factor

It shows that the fundamental resonance and anti-resonance frequencies as well as the corresponding electromechanical coupling factor decrease as the thickness of the whole epoxy increases. Further, keeping the thickness of the whole copper package as constant, Figure 3-4 and Figure 3-5 present the effects of the thickness and diameter of PZT patch on the dynamic characteristics of SA. In Figure 3-4, the thickness of PZT patch ranges between 0.1 and 0.8 mm. It can be found that with the increase of the thickness of PZT patch, the fundamental resonance frequency decreases obviously than the fundamental anti-resonance frequency, which leads to the increase of the corresponding electromechanical coupling factor. The diameter of PZT patch ranges between 10 and 16 mm. Similar results obtained from Figure 3-5 can be also found.

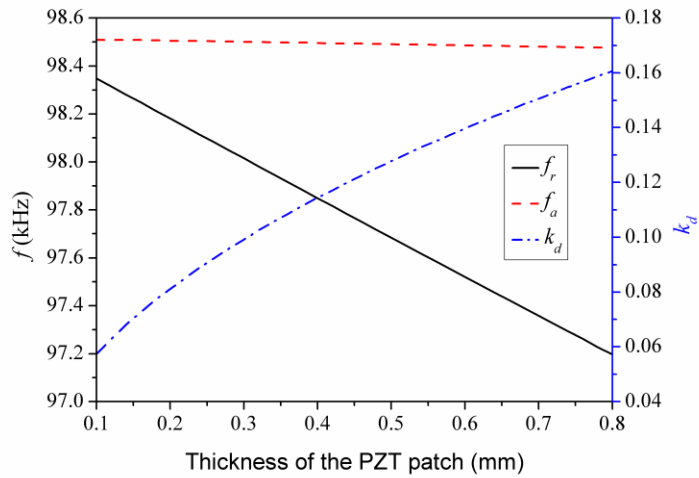


Figure 3-4 The influence of the thickness of the PZT patch on the fundamental resonance and anti-resonance frequencies as well as the corresponding electromechanical coupling factor

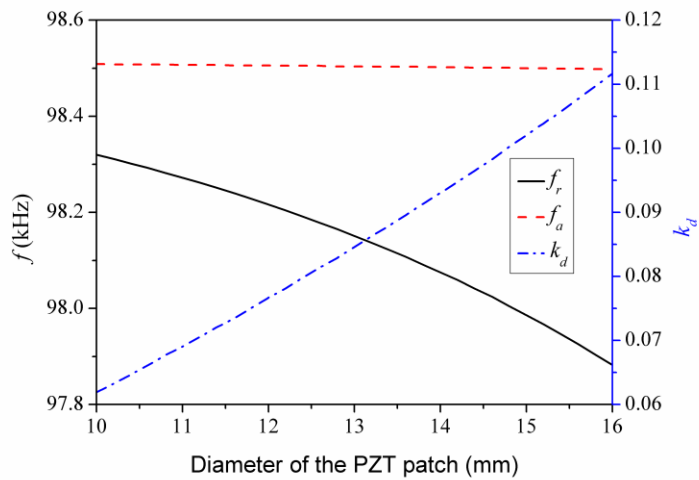


Figure 3-5 The influence of the diameter of the PZT patch on the fundamental resonance and anti-resonance frequencies as well as the corresponding electromechanical coupling factor

3.5 Experimental verification

In order to verify the theoretical model, two smart aggregates are experimentally investigated. The thickness of the Epoxy layer between two Marbles is measured using a

vernier caliper. Both thickness of the Epoxy layer are around 0.62mm. Further, their fundamental resonance and anti-resonance frequencies are measured using *Agilent 4294A Precision Impedance Analyzer*, as shown in Figure 3-6. The smart aggregate samples are laid on the sponge along the z-direction during test, which can be considered as a free-free mechanical boundary condition.

In the test, the *Agilent 4294A Precision Impedance Analyzer* scanned the smart aggregates in the frequency range from 60 KHz to 90 KHz and the impedance of each smart aggregate was recorded.

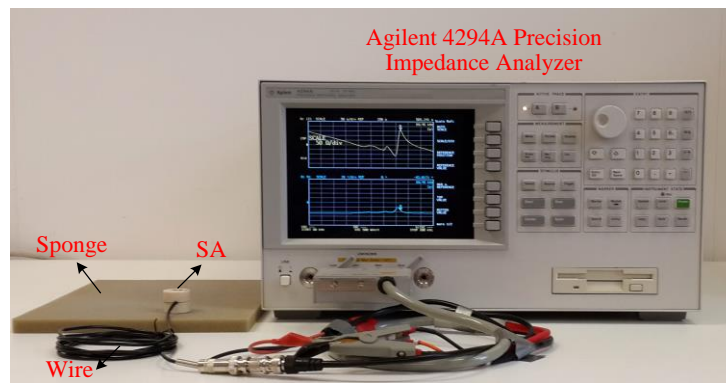


Figure 3-6 Experiment setup

The measured impedance-frequency relationship for the two samples of smart aggregates is shown in Figure 3-7, where the fundamental resonance and anti-resonance frequencies can be obtained. The theoretical and measured results are listed in Table 3-2. The errors ($\text{Error} = (\text{Theory} - \text{Experiment}) / \text{Theory}$) between the fundamental resonance and anti-resonance frequencies are 2.49% and 1.07% for SA-1, 0.05% and -1.25% for SA-2, respectively. From the comparative results, it can be seen that the measured frequencies are basically in agreement with the theoretical results.

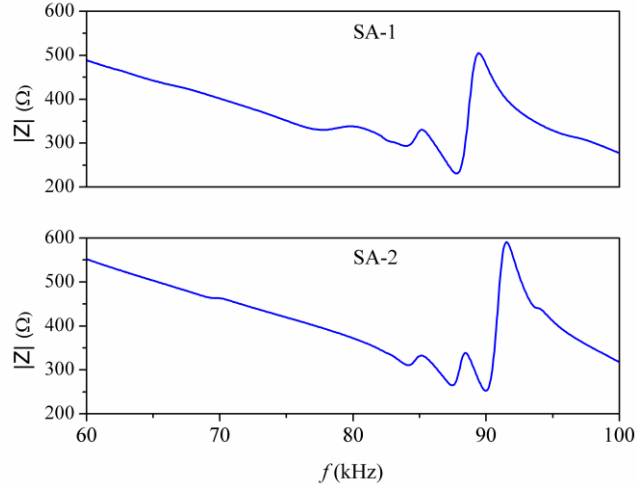


Figure 3-7 Relationship between impedance and frequency for smart aggregates

Table 3-2 Theoretical and experimental results

		Resonance f_r (kHz)	Anti-resonance f_a (kHz)
Theoretical results		90.04	90.42
Experimental results	SA-1	87.80	89.45
	SA-2	90.00	91.55

3.6 Summary

Based on one dimensional linear theory of piezoelectricity, a simplified theoretical model was established to analyze the electromechanical characteristics of smart aggregate. The electric impedance was analytically derived, and the resonance and anti-resonance frequencies equations were also given. The relationships between the resonance and anti-resonance frequencies with the thickness of the whole epoxy between two marbles, the thickness and diameter of the PZT patch were discussed. In addition, experiments were done to validate the theoretical analysis. The analytical fundamental resonance and anti-resonance frequencies are in good agreement with the experimental results, which can validate the reasonableness of the proposed simplified theoretical model.

4 Structural crack monitoring

4.1 Introduction

Crack damage is harmful to the health of structures. If the early crack is not promptly detected and addressed, the developed crack may potentially arouse a failure of the whole structure [107]. Structural crack detection is an important field in structural health monitoring. Traditionally, most of the crack damage was detected by visual check. Trained inspectors were assigned to the in-situ place to check the presence of local cracks in some critical points of a structure [5]. The disadvantage of visual check for crack detection is the poor accuracy of the results which high depend on the experience of the assigned inspectors. In addition, the internal crack in structures can hardly be detected.

Active sensing approach has been proofed to be an exceptional method for structural health monitoring. Many successful applications of structural health monitoring using active sensing approach have been presented [108] [109] [110]. As mentioned in Section 2.4, piezoceramic transducers can function as both actuators and sensors which are capable of being used in the active sensing approach for structural health monitoring. In the past decades, piezoceramic transducers have been successfully applied to structural crack detection by researches. Ruan *et al.*, presented a polar plot analysis using attached piezoceramic patches to detect the crack damage on a wind turbine blade [111]. Yan *et al.*, embedded piezoceramic transducers to monitor concrete shear wall by a wavelet packet-based damage index [83].

In this chapter, an active sensing approach using piezoceramic based transducers was developed for structural crack monitoring. An experiment of crack detection of a

pipeline using piezoceramic based transducers was first investigated. A wavelet packet-based structural damage index was explored to determine the crack initiation and the further development in the pipeline. Another experiment of crack open-close monitoring of a concrete column using embedded smart aggregates was also investigated. The computed values in the structural damage index were used as indicators to determine if the crack is opening or closing.

4.2 Detection principles

The active sensing approach using smart aggregates is a good example to illustrate the principle developed in this chapter for structural crack monitoring, as shown in Figure 4-1. A column structure with embedded smart aggregates is drawn to explain the developed structural damage detection approach. One or several smart aggregates can function as actuators to generate guided waves propagating in the structure. Other distributed smart aggregates are used as sensors to receive the waves. If a crack appears in the structure, it can act as a stress relief in the wave propagation path. The amplitude of the received signal from sensors will attenuate due to the related cracks. In addition, the severity of cracks can be characterized by the selected signal processing technique called “wavelet packet-based analysis”, as mentioned in Section 2.5. A wavelet packet-based structural damage index is capable of providing quantitatively values to describe the initial crack in the structure and its further development.

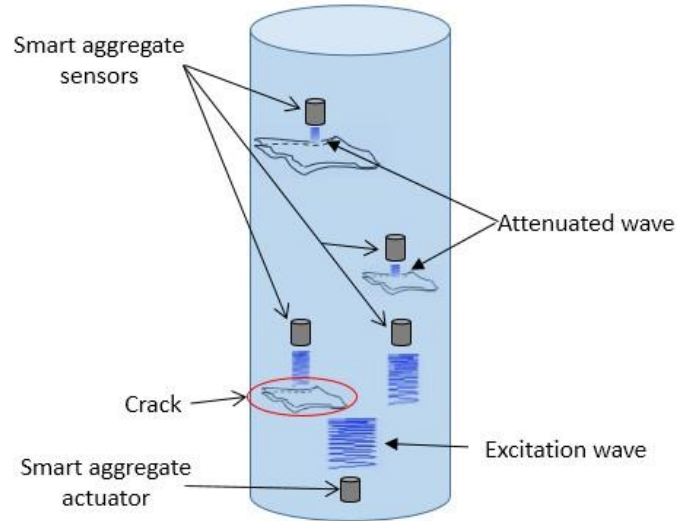


Figure 4-1 Block diagram of smart aggregate based active sensing system

4.3 Crack monitoring of a pipeline

4.3.1 Background

Pipelines consistently experience complications in service, with some examples being stress corrosion and excessive external forces, which cause the pipelines to form cracks. These cracks, if not detected in a timely fashion, may lead to catastrophic events with severe economic losses and environmental pollution. The study on damage detection of pipelines is of great significance to ensure their safe operation and receives increasing attention in the literature. Methods for pipeline damage detection include the fiber optic sensor based method [112], the acoustic emission method [113], the magnetic particle inspection method [114], the ultrasonic method [115], the eddy current method [116], and piezoelectric impedance method [22].

In recent years, the piezoceramic transducer based active sensing approach has been developed and demonstrated its promises in real-time damage detection and health

monitoring of civil infrastructures [23] [63] [82]. In this section, the feasibility study of developing the active sensing approach to crack detection of a pipeline using piezoceramic transducers was investigated.

4.3.2 Experimental setup and procedures

One section of a pipeline sample was used in this experiment. The pipeline was constructed from Q235 steel. The dimensions and material properties of the pipeline are shown in Table 4-1. The outer and inner diameters of the pipeline are 101mm and 80mm, respectively.

Table 4-1 Pipeline dimensions and Q235 steel properties

Steel grade	Density (kg/m ³)	Elastic modulus (MPa)	Poisson ratio	Wall thickness (mm)	Pipe length (mm)
Q235	7850	205,000	0.30	10.5	100

Four PZT patches were fixed on the pipeline surface using Epoxy (LOCTITE EPOXY). The locations of PZT patches are shown in Figure 4-2. It should be noted that PZT-1, PZT-2, and PZT-3 are equidistant from each other along the length of the pipe. Also seen in Figure 4-2, the location of PZT-4 is rotated 90 degrees counterclockwise from PZT-3. A third point to note is that an artificial crack was cut approximately halfway between PZT-1 and PZT-2. Figure 4-3 shows the actual specimen with the aforementioned PZT locations and the artificial crack.

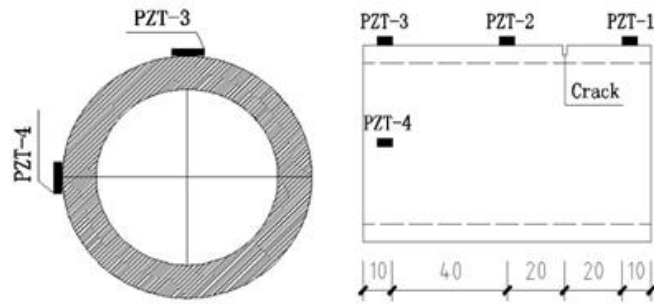


Figure 4-2 location of PZT patches on the pipeline

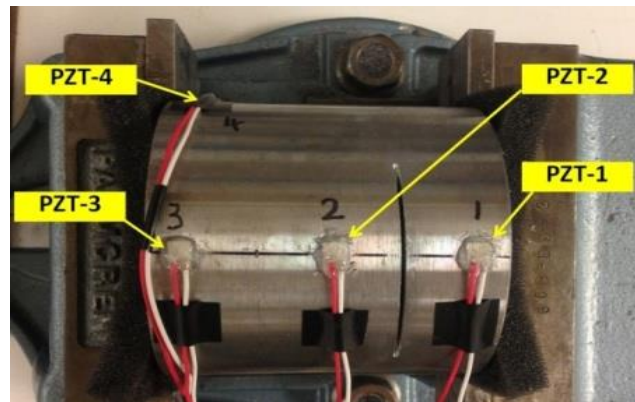


Figure 4-3 A photo of pipeline specimen with PZT patches

As mentioned previously, the PZTs display special electromechanical properties, such as density, capacitance, etc. Some of these properties are presented in Table 4-2.

Table 4-2 Important properties of PZT patches used in the experiment

Density (g/cm ³)	Dielectric constant	Electromechanical coupling coefficient	Capacitance (nF)	Piezoelectric coefficient (C/N)	Curie temperature (°C)
7.50	1600±10%	0.65	3.77	450	350

During the test, eight operating conditions correlating to different crack depths (0 mm – 10.5 mm) were investigated. Table 4-3 depicts each operating condition with its corresponding crack depth. It should be noted that the crack depth increases by 1.5 mm for each operating condition starting from Condition 1.

Table 4-3 Test operating conditions (OCs)

Operating Condition	1	2	3	4	5	6	7	8
Crack depth (mm)	0	1.5	3.0	4.5	6.0	7.5	9.0	10.5

In the presented test system, the PZT actuator (PZT-1) is connected with a function generator (Agilent 33120A). The PZT sensors (PZT-2, PZT-3 and PZT 4) are connected with a data acquisition system (NI USB-6363). The sampling rate of the data acquisition system for each channel is 1Ms/S. The test bench is used to fix the pipeline sample. Please note that two pieces of artificial form were placed between both pipe edges and the test bench. Thus the stress wave cannot propagate through the test bench. The experimental setup is shown in Figure 4-4.

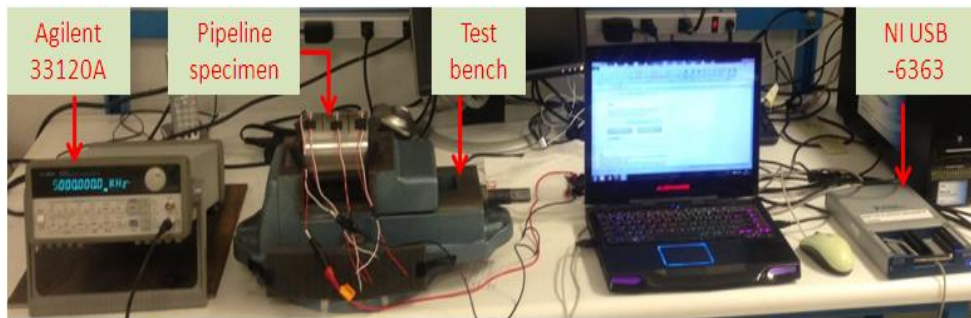


Figure 4-4 Experimental setup

During the test, PZT-1 was used as an actuator and PZT-2, PZT-3, PZT-4 were used as sensors. A swept sine wave signal from 60 kHz to 200 kHz was generated by PZT-1, as shown in Figure 4-5. The amplitude of the excitation signal is 10V and the period is 2s. During each operating condition, PZT-1 produced the guided swept sine wave to all the other sensors and the response signal were recorded by the sensors. Since the pipeline crack was regarded as a stress relief which affected the performance of the

stress wave propagation between the actuator and sensors, the sensor signals accurately reflected the pipeline crack severity for each operating condition.

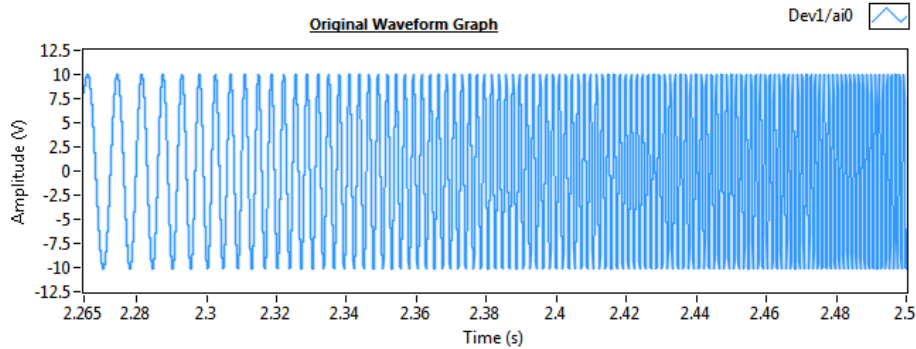


Figure 4-5 One section of the swept sine wave signal used in the experiment

4.3.3 Experimental results

The received signals of PZT-2, PZT-3 and PZT-4 in each operating condition are shown below in Figure 4-6, Figure 4-7 , and Figure 4-8. Each signal was subject to several resonance frequencies within the range of 60 kHz to 200 kHz. Each plot reflects the sensor signal response from one period of the swept sine wave signal, which is equal to 2 seconds in the time domain. From the plots, several resonance peaks can be observed, especially towards the end of the period (i.e., after 1.8 seconds). Through the analysis of these peaks, the same general trend can be identified for each of the PZTs. This trend shows that the amplitudes of the resonance peaks decrease with an increase of the crack depth. This trend indicates that less energy is collected by the sensors with increasing crack depth. Ultimately when the crack is of a depth near 10.5 mm, the entire signal response is extremely weak, which indicates that the crack almost fully blocks the stress wave propagation from the actuator to sensors.

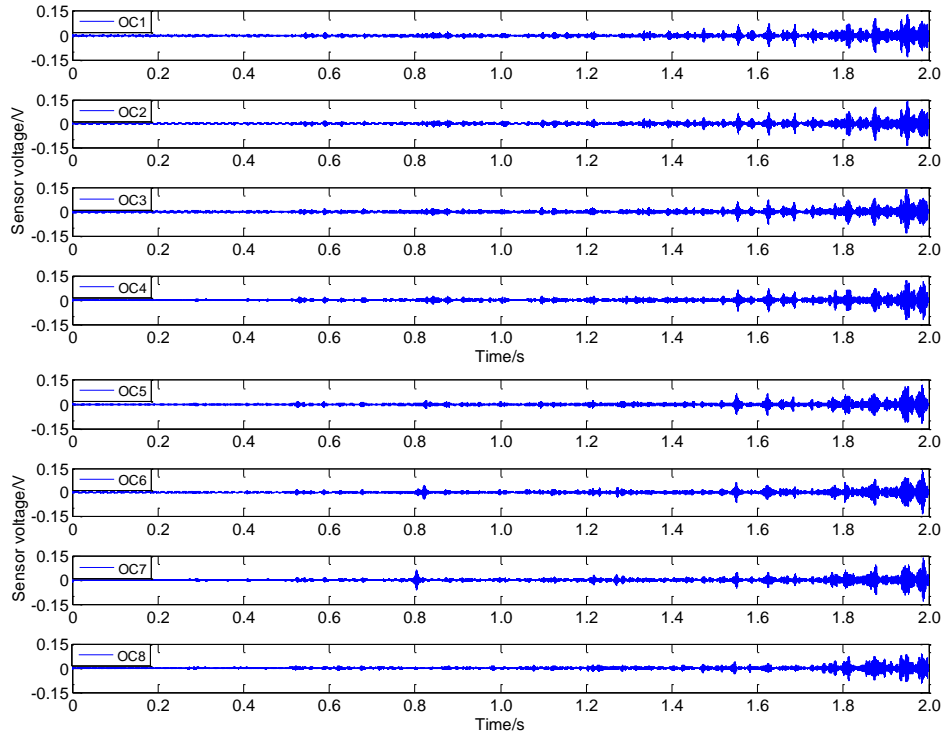


Figure 4-6 Signal response of PZT 2 for Each Operating Condition (OC)

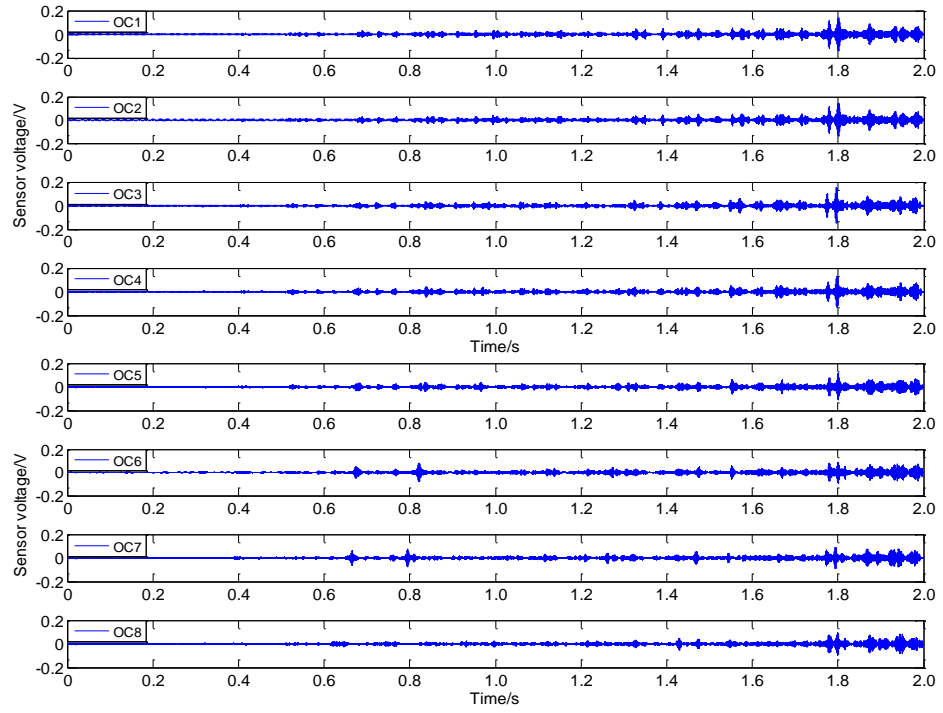


Figure 4-7 Signal response of PZT 3 for Each Operating Condition (OC)

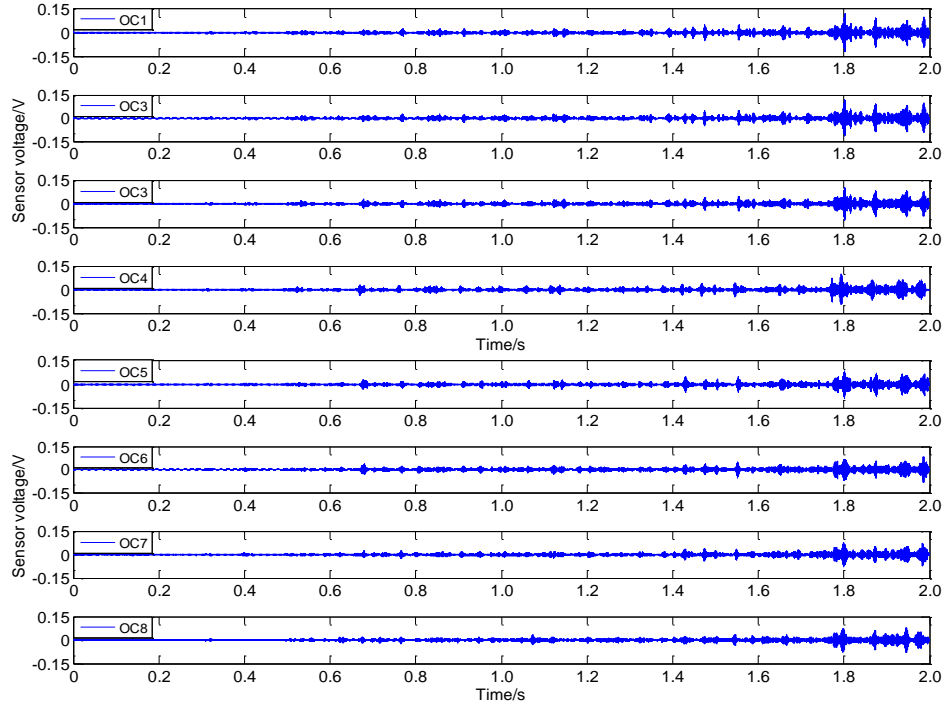


Figure 4-8 Signal response of PZT 4 for Each Operating Condition (OC)

In order to quantitatively analyze the crack severity on the pipe, the wavelet packet-based crack severity index is developed, as shown in Figure 4-9. The height of the bars indicates the damage degree collected by the each corresponding sensor. Based on the principle of the crack severity index, 0 is the health status of the structure corresponding to a crack depth of 0 mm (Operating Condition No. 1). It can be seen that the heights of the bars increase for each incremental operating condition that corresponds to an increase of the crack depth. For Sensor 2, the most distinguishable changes in crack severity index are observed due to the increases in bar height up to the value of 0.4 for Operating Condition No. 8. This can be attributed to Sensor 2's close proximity to the artificial crack location on the pipe (as seen in Figure 4-3). The same trend is also observed for Sensors 3 and 4, which confirms that the crack functions as a stress relief in the wave propagation path.

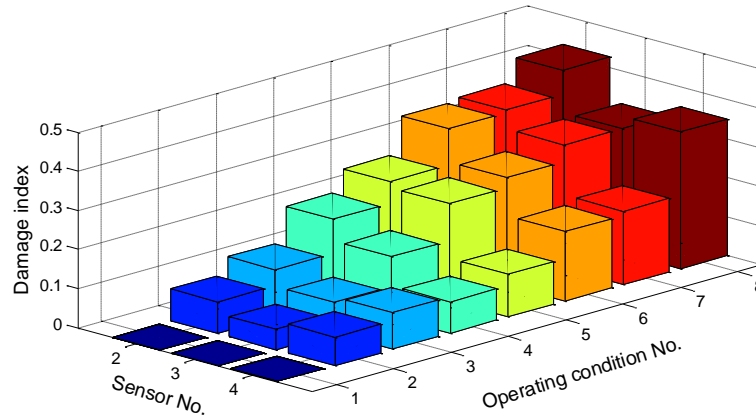


Figure 4-9 Wavelet packet-based pipeline crack severity index

4.3.4 Discussion

The active sensing approach using distributed piezoceramic based transducers was developed in this section for crack detection. Since the crack functions as a stress relief in the wave propagation path, the signal response of the sensors report a decreasing trend with the increasing depth of the crack. From the wavelet packet-based crack severity index, the crack severity for each operating condition was quantitatively identified by the values indicated by the heights of the index bars. As the cracks developed, the damage index for all sensors increased. In addition, the energy loss phenomenon directly correlated to the locations of the sensors with respect to the crack and the sensitivity of the sensors. It was then identified that the sensor closest to the crack was subject to a largest energy loss. Since the damage index value of the sensors is highly dependent upon sensor locations, the proposed crack severity index presents great potential to locate cracks with distributed sensors.

4.4 Crack monitoring of a concrete column due to simulated pseudo-dynamic load

4.4.1 Background

In this section, another application of structural crack monitoring was presented. Under the dynamic load (seismic excitation), smart aggregates were used as transducers to perform the health monitoring test on a reinforced concrete (RC) column. In the proposed health monitoring approach, one smart aggregate was used as an actuator to generate a swept sine signal while the others were used as sensors to detect the signal response from different location. The propagation energy of the waves will be attenuated by cracks in the concrete structure. The attenuated energy can be used as a parameter to evaluate the structural damage. A wavelet packet-based structural damage index was developed to detect the concrete crack in the test.

4.4.2 Experimental setup and procedures

A RC column instrumented with 12 smart aggregates was fabricated at Prestressed Engineering Company, LLC in Blackstone, Illinois. The location of smart aggregates in the concrete column is shown in a structural drawing and a three-dimensional view. Figure 4-10 and Figure 4-11 show pictures of some smart aggregates actual location in the rebar cage of the column.

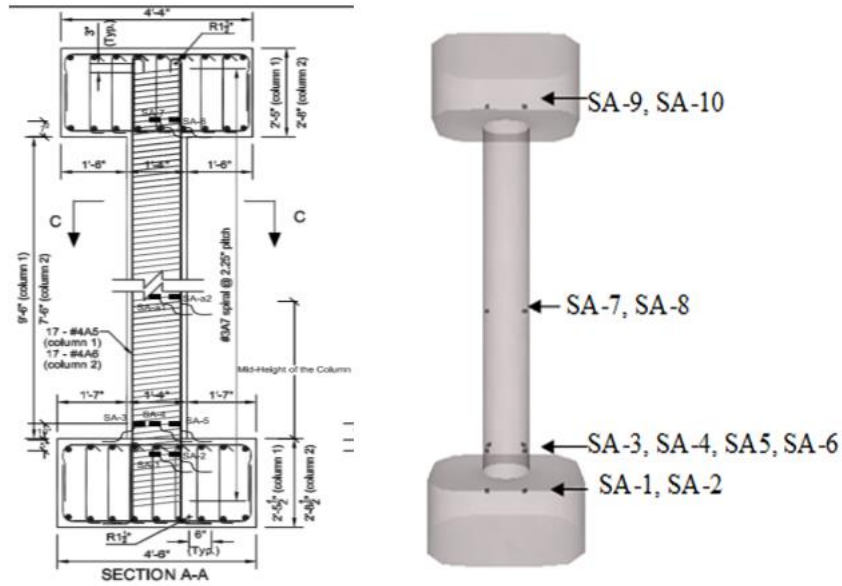


Figure 4-10 Location of smart aggregates in the concrete column



Figure 4-11 (a) A smart aggregate fixed on the rebar cage (b) A Smart aggregate was installed in the base

A series of 330 kip actuators called “Load and Boundary Condition Boxes” (LBCDs) were placed at the top of the full-scale column to apply load to the specimen. The test concrete column was mounted to a strong floor using all-thread rods. The column was instrumented with LVDTs, strain gauges, Krypton displacement cameras, in addition to the smart aggregates. A photo of the casted concrete column can be seen in Figure 4-12. In the test, the smart aggregate (1) was used as the actuator to generate a

swept sine wave through a function generator. The amplitude, period, and the frequency range of the swept sine wave are 10V, 3s, and 100 Hz-10 kHz, respectively. Smart aggregates (3) to smart aggregate (10) were used as sensors to detect the signal. The sensing signal was recorded by a NI-6353 data acquisition system.



Figure 4-12 A photo of the concrete column after casing

During the test, the concrete column was assumed to be a column in a curved bridge subjected to a simulated pseudo-dynamic earthquake record. After each step of the record, the stiffness of the column was calculated and the next step of the earthquake record was adjusted using a finite element analysis to account for any decrease in stiffness in the system. The simulated earthquake record represented a 40 second earthquake. The magnitude of the acceleration was increased every 10 seconds. Figure

4-13 and Figure 4-14 show the acceleration record and a response spectrum showing the design spectral acceleration and the spectral accelerations corresponding to the four acceleration levels, respectively. Structural health monitoring tests were performed periodically during the approximately 38-hour test.

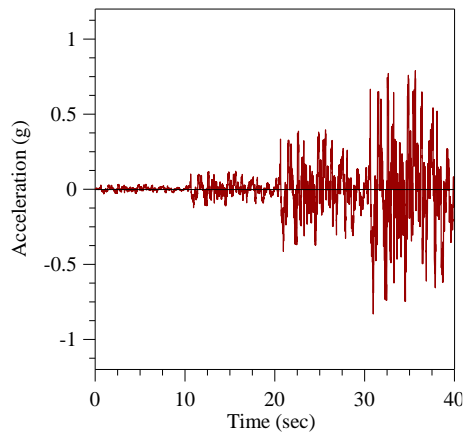


Figure 4-13 Acceleration record

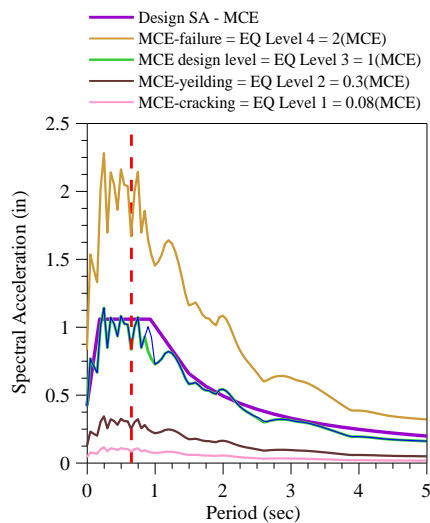


Figure 4-14 Response spectrum

4.4.3 Experimental results and discussions

The test was stopped due to the actuators in the x-direction running out of stroke. At that point, the concrete column had yielded and was exhibiting spalling, but had not

yet failed. Figure 4-15 and Figure 4-16 show the force-displacement and moment-curvature relationships in the x-, y- and z-directions for the concrete column, respectively.

A photo of the yielded concrete column after test is shown in Figure 4-17.

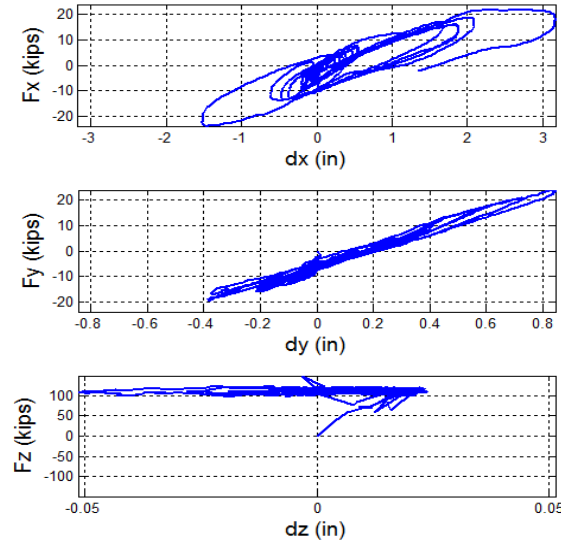


Figure 4-15 Force-displacement relationships for the concrete column

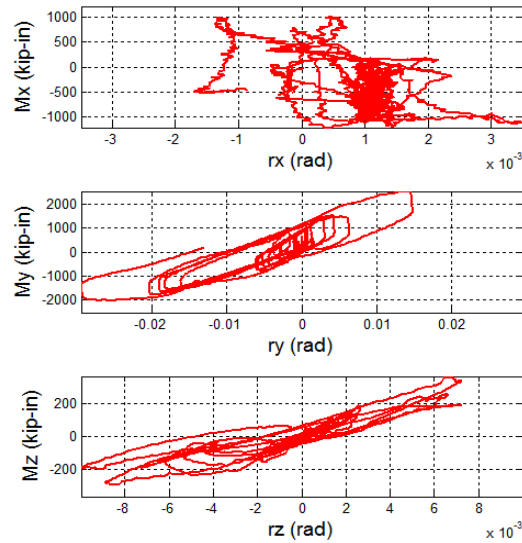


Figure 4-16 Moment-curvature relationships for concrete column



Figure 4-17 A photo of the concrete column yielding after test

As shown in Figure 4-15, x-direction is the main axis of displacement to the concrete column. Therefore, the phenomenon of the cracks “open and close” is highly depended on the cycles of displacement in x-direction. The displacement history in x-direction at the top of concrete column was shown in Figure 4-18. During the 38-hour test, 13 cycles of displacement in x-direction is observed and marked in Figure 4-18.

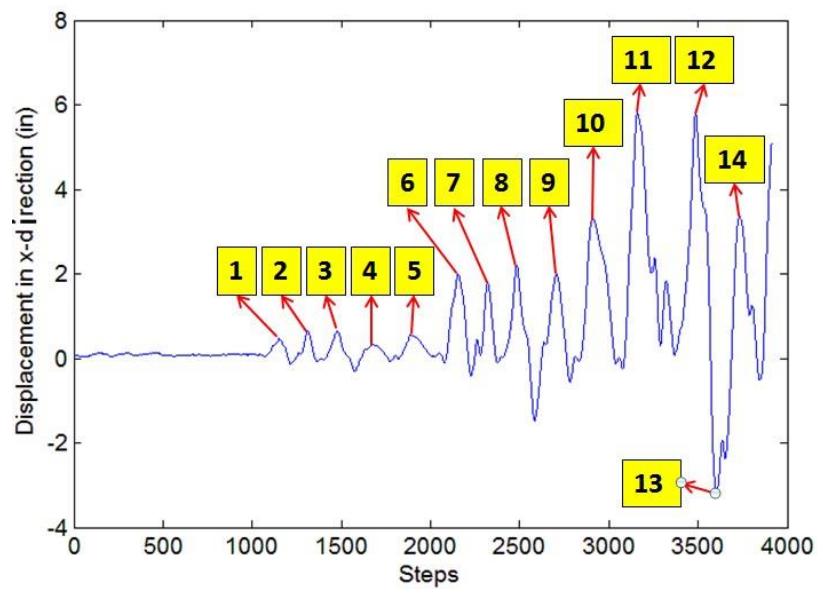


Figure 4-18 Displacement history in x-direction of the column

In the test, smart aggregate (6) and smart aggregate (9) failed to function. The possible reason for the dead sensors may be the wire broken in the concrete during casting. Experimental results from other sensors are shown below.

Figure 4-19 shows the wave packet-based damage index for the concrete column. From Figure 4-19, it is seen that the damage gradually increases throughout the duration of the test. It is also obvious that the damage increased greatly shortly after Step 1000, this corresponds to the first cracks in the column. In some places, the damage index decreases rather than increasing. This is due to the cyclic behavior of the test. As the column is pushed in one direction, cracks open on the side of the column that is in tension. As the column is pushed in the opposite direction, these cracks close. The lower damage index values correspond to the original cracks closing during the cyclic loading.

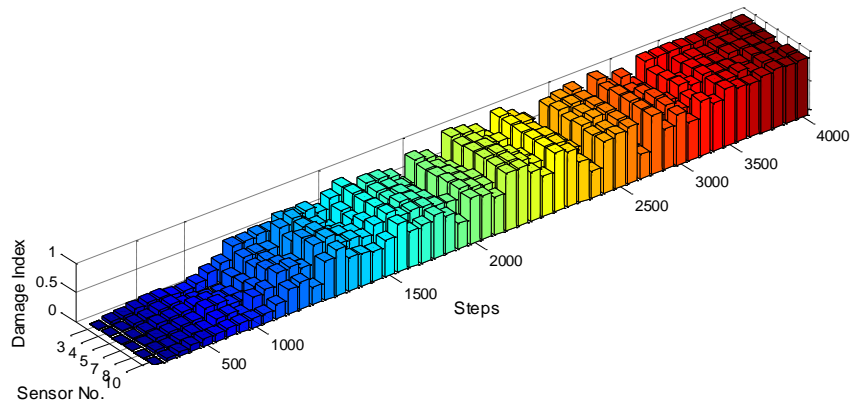


Figure 4-19 wave packet-based damage index for the concrete column

According to the x-direction displacement history, the damage index is separated into several sub-indices according to the x-direction displacement cycles. In the first 1000 steps, the displacement of the concrete column is very small. The damage index of the

concrete column in the first 1000 steps is shown in Figure 4-20. It can be clearly seen that the values of the index for all the sensors are small. The values of the index in the first 1000 steps yield to the x-direction displacement data.

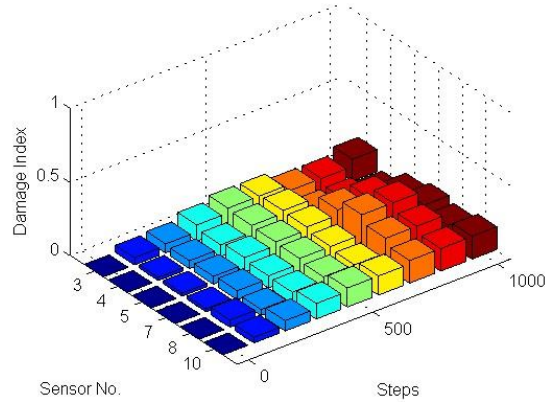


Figure 4-20 Damage index of the concrete column in first 1000 steps

The separate damage indices from cycle 1 to cycle 5 corresponding to step 1100 to step 2100 are shown below in Figure 4-21. Each damage values have the same trend which is increasing in the first half and decreasing in the second half. The increasing and decreasing phenomenon of each damage index confirms the cyclic behavior of the test. As the column is pushed in one direction, the cracks open which correspond to the increasing of the damage index values. As the column is pushed back, the cracks close which correspond to the decreasing of the damage index. Please note that, the motion of the concrete column in first 5 cycles is smaller than the other cycles. The maximum value of the damage index is around 0.8.

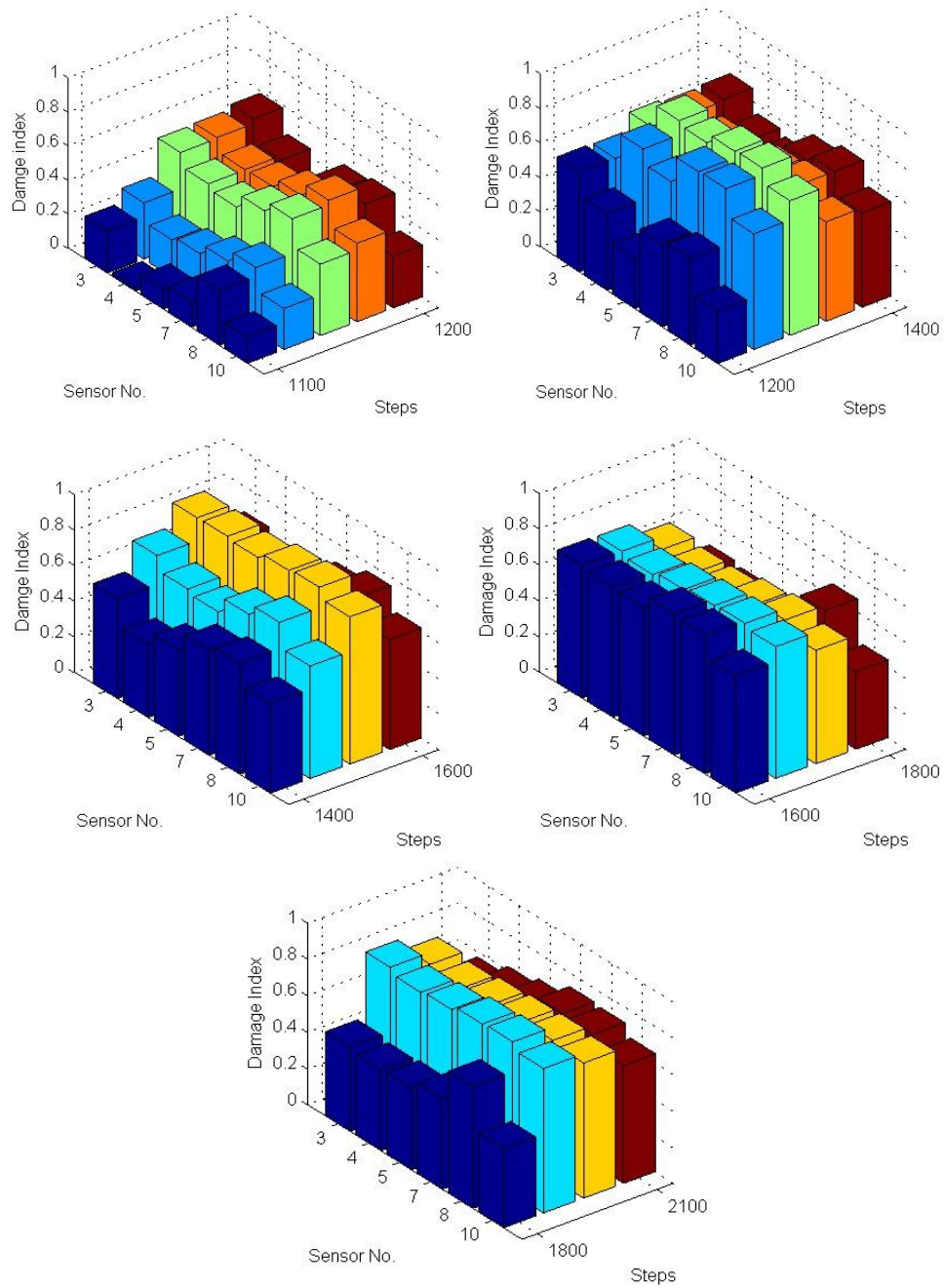


Figure 4-21 Damage indices of the concrete column from step 1000 to step 2100

The separate damage indices from cycle 6 to cycle 11 corresponding to step 2100 to step 3500 are shown in Figure 4-22. Similar trend can be also found in these indices. The values of the damage index is increasing as the cracks open and decreasing as the

cracks close. In this period, x-displacement of the concrete column is much larger than those from cycle 1 to cycle 5. Since the concrete column structure has been failed, the maximum value of the damage index is approaching to 1.

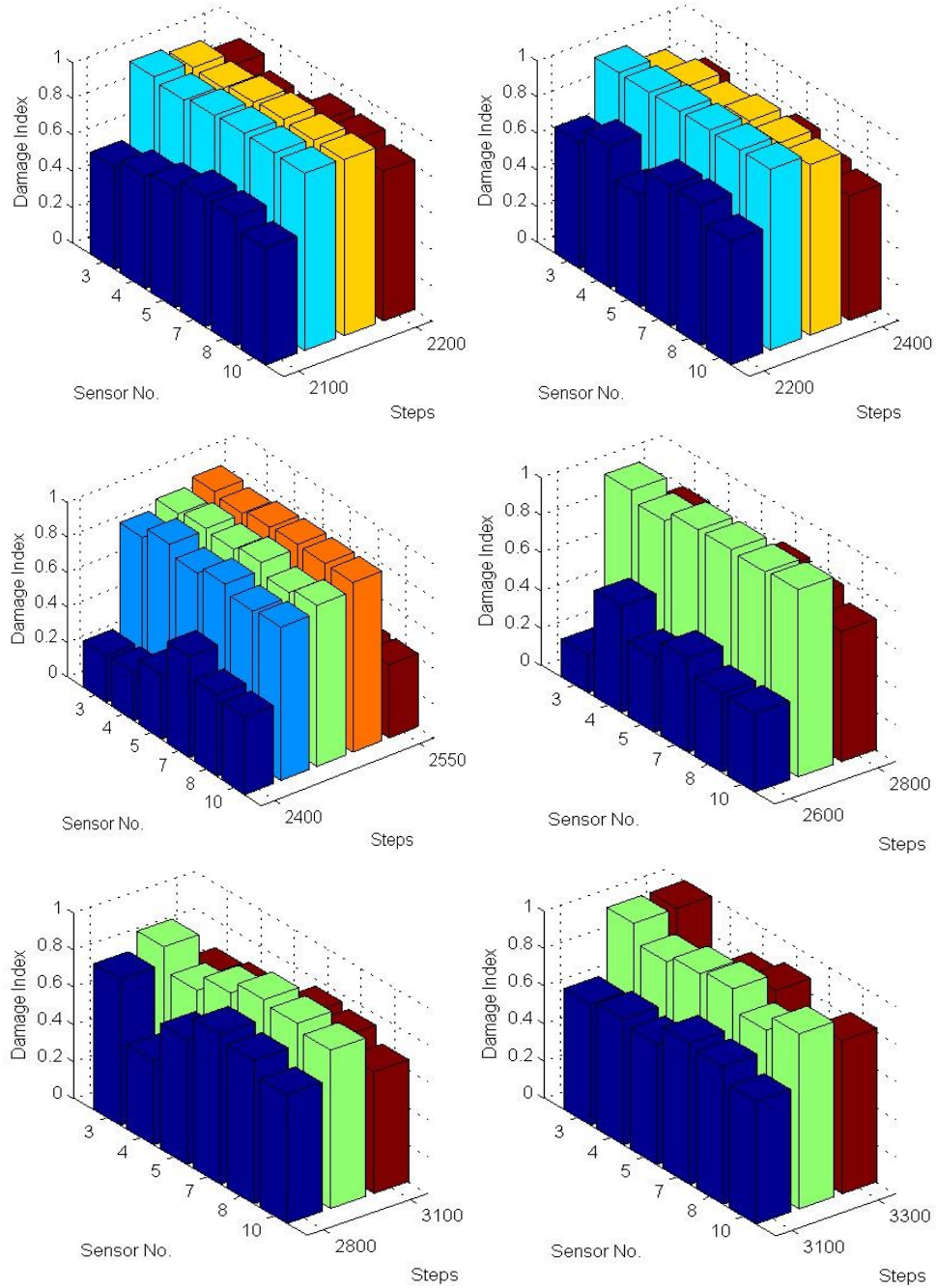


Figure 4-22 Damage indices of the concrete column from step 2100 to step 3300

The separate damage index from cycle 12 to cycle 14 corresponding to step 3500 to step 4000 is shown in Figure 4-23. Compared to the previous damage indices, the values of the damage index is not presenting an increasing and decreasing phenomenon. It can be concluded that the cracks in this period are in large degree which dramatically attenuates the stress wave energy propagation from the actuator to the sensors. The sensors can receive very little energy which leads to the values of the damage index stable at 1 even when the concrete column is pushed.

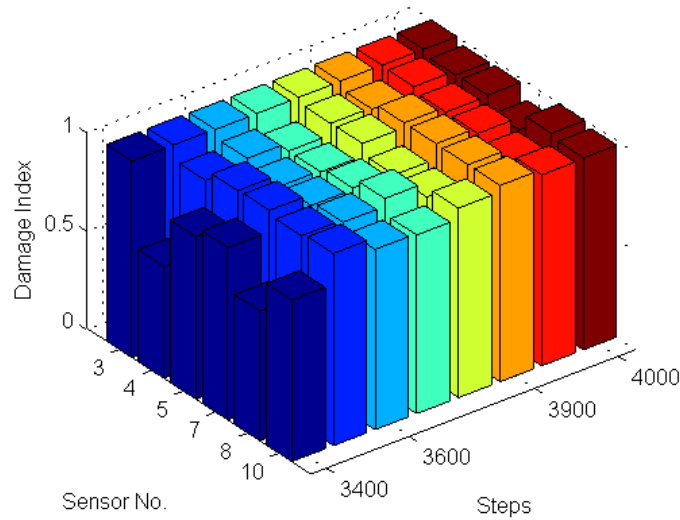
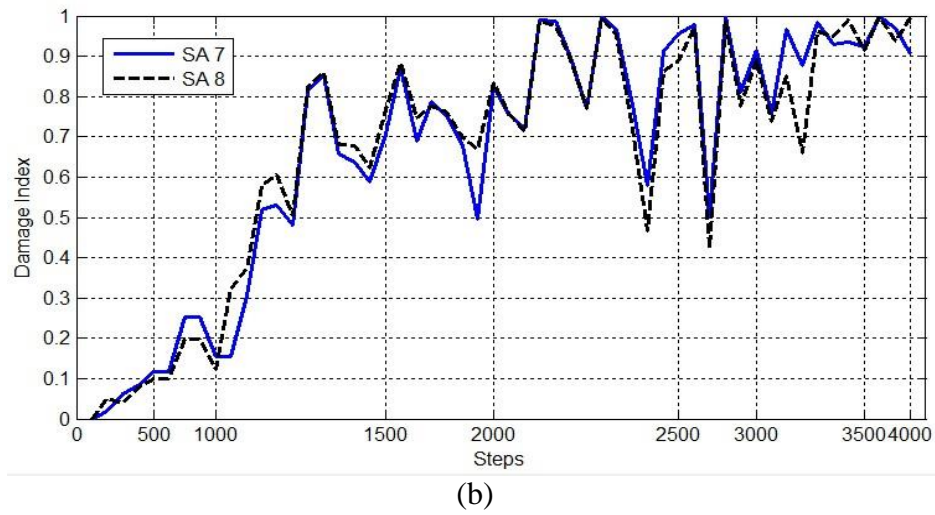
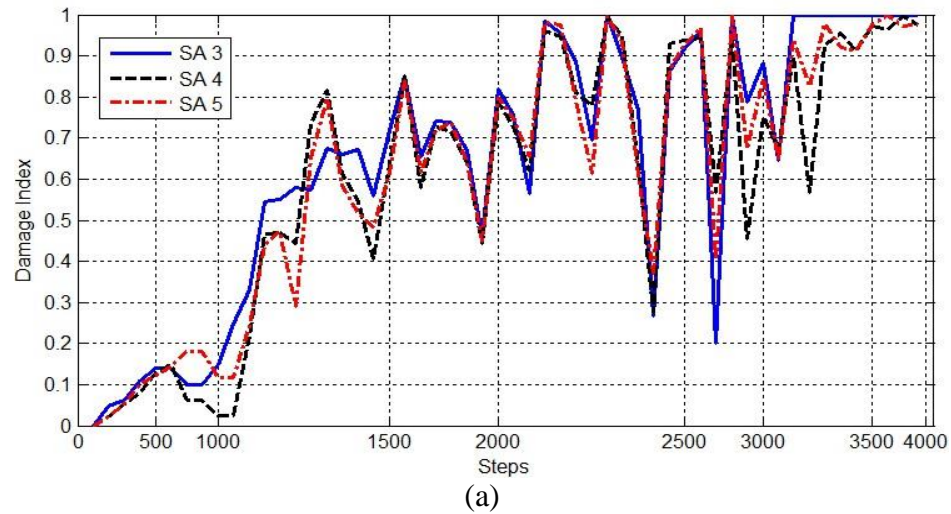


Figure 4-23 Damage index of the concrete column from step 3400 to step 4000

Figure 4-24 presents the damage indices of the concrete column at different locations from the bottom to the top. Figure 4-24(a) (b) (c) present the damage index of the concrete column at bottom, middle, and top, respectively. Since the actuator in this test is from the concrete base and most of the cracks occurred at the very bottom of the concrete, all received signal from sensors were significantly influenced by those cracks. The received signal of each sensor was correspondingly attenuated by the crack.

Therefore, the phenomenon of the cyclic value for each sensor can be observed from all the damage indices. The values of the damage index from different locations are closing to each other which mean that the major crack happened on the bottom of the concrete column is successfully detected by all the operating sensors.



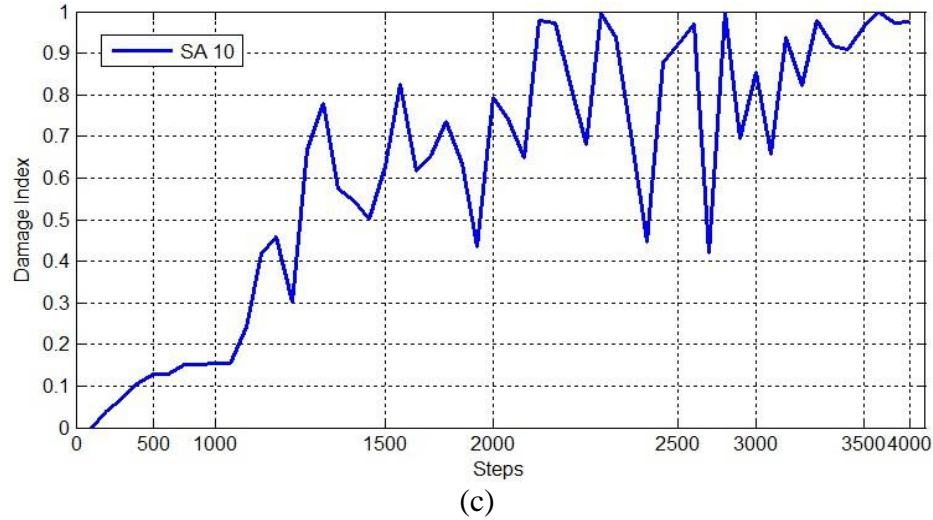


Figure 4-24 Damage indices of the concrete column from different locations (a) Bottom sensors, (b) Middle sensors, (c) Top sensors

4.5 Summary

In this chapter, structural crack detection using piezoceramic based transducers was researched. An active sensing approach using distributed piezoceramic based transducers was developed to detect cracks and monitor the crack development in a pipeline. The crack development in the pipeline was presented by the increasing values in the wavelet packet-based structural damage index. This method also provide a possibility to locate the crack through the appropriate development of sensors. Another experiment of a concrete column was investigated to monitor crack open-close condition under the simulated earthquake. The increasing and decreasing values shown in the wavelet packet-based structural damage index has the potential to offer appreciable values to determine if the crack is opening or closing.

5 Bond slip detection of steel plate concrete beams

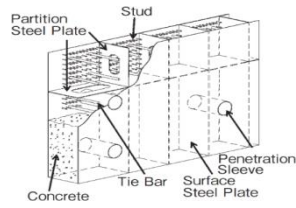
5.1 Introduction

Concrete is the most popular construction material in structural engineering practice. To obtain better structure behavior and take advantage of material strength, concrete structure is quite often constructed with steel, including concrete and reinforcing bar used in reinforced concrete, concrete and pre-stressing tendon used in pre-stressed concrete, concrete and steel plate used in concrete steel composite structures.

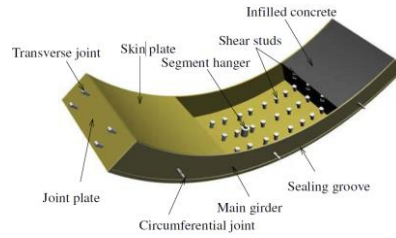
Steel plate concrete (SC) structures have a lot of advantages, such as:

- (1) Steel plate can act as formwork, and placement of rebar and removal of formwork are eliminated [117].
- (2) SC structures are efficient in terms of cost, labor and construction period, especially when modular construction is adopted [118].
- (3) Tests showed that SC panels are very effective for protection of structures against impact by aircraft [119].

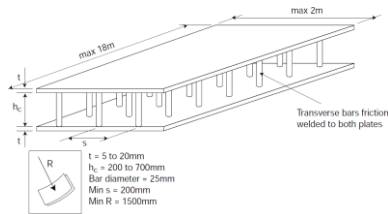
Steel plate reinforced concrete (SC) structures take the full advantage of respective strengths of steel and concrete. SC structures are widely applicable in structural engineering practice, i.e., containment wall for nuclear power plants as shown in Figure 5-1(a) [120], submerged tube tunnels as shown in Figure 5-1(b), core or shear wall system for skyscrapers as shown in Figure 5-1(c), blast and impact resistant shelters as shown in Figure 5-1(d), offshore decking system and bridge deck [121], pressure hulls for subsea oil production [122], etc.



(a) Typical SC structure used in nuclear power plants



(b) Schematic of composite segment for shield tunnel



(c) British Bi-steel for skyscrapers



(d) SC shell with J hocks for ice-resistant shell

Figure 5-1 Applications of steel plate concrete structures

Theoretically, as long as the integrity of SC structures is sustained, SC structures can take the full advantage of respective strengths of steel and concrete. However, integrity of SC structures may be undermined or even lost due to adverse effects such as concrete cracks, buckling of steel plates, poor concrete compactness and bond slip, etc. Experimental studies showed that bond slip in SC beams could lead to integrity loss, and subsequently SC beams lost the stiffness and end up with a reduced fatigue life [123].

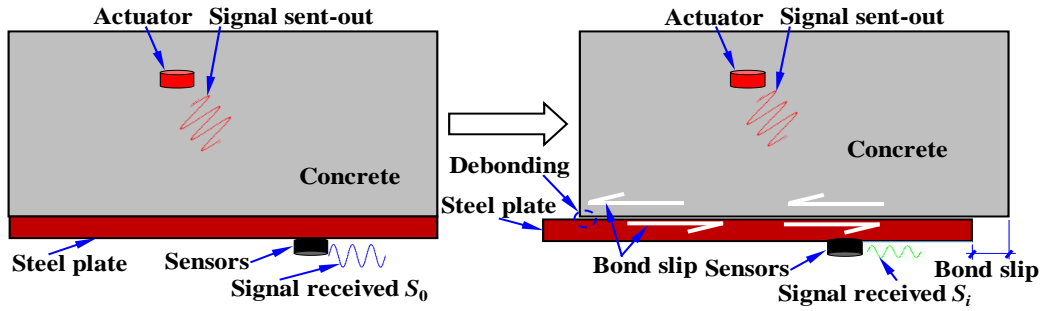
Piezoceramic transducers have shown the potential to detect the debonding condition in recent years. Wu *et al.*, indicates that debonding between concrete and rebar and yielding in rebar can be detected with built-in piezoelectric sensors and actuators [124]. Xu *et al.*, succeed in active detection of interface debonding in concrete filled steel tube using piezoelectric transducers and wavelet packet-based analysis [89]. Yan *et al.*,

applied time reversal technique to detect the compactness of concrete in concrete filled steel tube using smart aggregates [125].

In this chapter, an active sensing approach using smart aggregates was developed to detect bond slip between steel plates and concrete of SC beams. Two SC beams with different reinforcement ratio were investigated. A wavelet packet-based analysis was used to from the structural damage index which can provide an early detection of the bond slip, and a continuously monitoring of the bond slip development.

5.2 Detection principles

Figure 5-2 presents the principle of the bond slip detection between concrete and steel plate using smart aggregate based active sensing system. As shown in the figure, one smart aggregate embedded in the concrete (mark with red) is utilized as an actuator. A swept sine wave with desired parameters is generated by the actuator. Other smart aggregates are attached on the surface of the steel plate. When no bond slip happens, the sensor signal is recorded as a baseline. When bond slip happens, the compactness between concrete and steel plate will decrease. Due to the properties of stress wave propagation [126], the stress wave energy will attenuates related to the severity of the bond slip condition. The wavelet packet-based damage index can be utilized as an indicator to identify the beginning and the degree of the bond slip. In addition, if several predetermined distributed smart aggregates are attached on the steel plate, the proposed method has the potential determine the location of where bond slip happens.



(a) Health state before bond slip

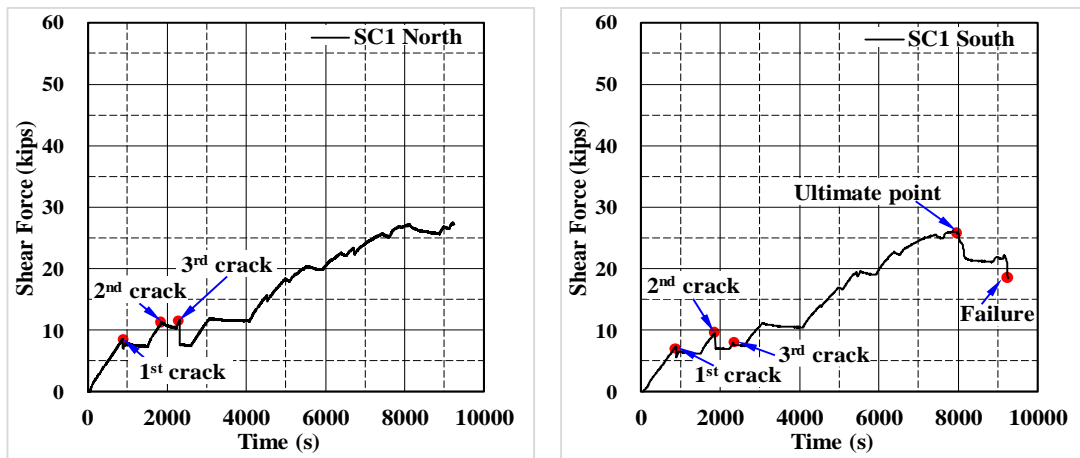
(b) Damaged state after bond slip

Figure 5-2 Block diagram of smart aggregate based bond slip detection between concrete and steel plate

5.3 Bond slip detection of steel plate reinforced concrete beams

5.3.1 Experimental results and discussions

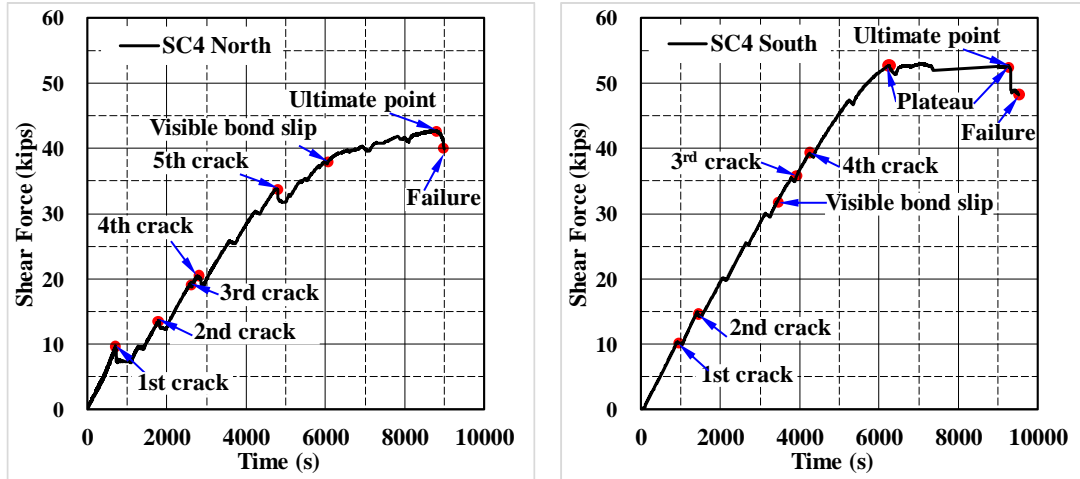
In both experiments, shear force for each beam at each side was measured. The curves of shear force vs. time for each test are shown in Figure 5-3 and Figure 5-4. According to the measured curves of shear force vs. time and visual check during loading, the statistic of crack damage and visible bond slips are shown in Table 5-1.



(a) SC1 north

(b) SC1 south

Figure 5-3 Shear Force vs. time of SC1 north and south



(a) SC4 North

(b) SC4 South

Figure 5-4 Shear Force vs. time of SC4 north and south

Table 5-1 Damage information of each beam

	1 st crack	2 nd crack	3 rd crack	4 th crack	5 th crack	Visible bond slip
SC1 North	—	—	2320s	—	—	7690s
SC1 South	880s	1870s	—	—	—	6615s
SC4 North	705s	1810s	2665s	2849s	4855s	6200s
SC4 South	1440s	1980s	5250s	6415s	—	3535s

Some photos of cracks and bond slips are shown in Figure 5-14 and Figure 5-15. For north side of the beam, SA01 was used as the actuator and SA1-4 were used as sensors; For south side of the beam, SA02 was used as the actuator and SA5-8 were used as sensors. The damage index for each sensor was calculated. The results of each side of the beam are presented as followed:

5.3.1.1 SC1 test

The loading test of SC1 lasted around 9000s. During the test, several cracks and bond slips were observed. Three major cracks occurred at the location shown in Figure 5-5 and Figure 5-6.

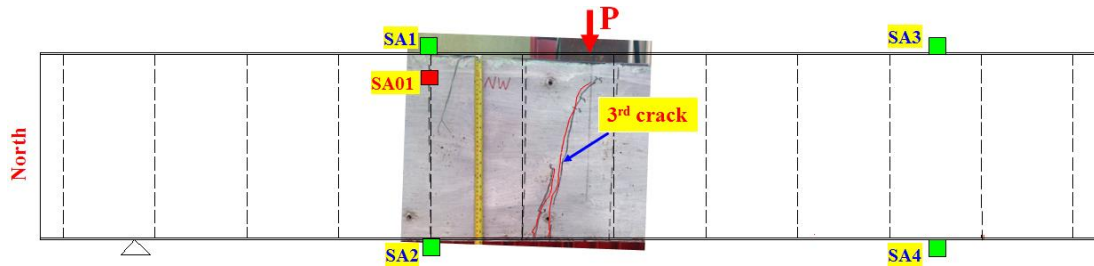


Figure 5-5 Details of crack on north side of SC1 after loading

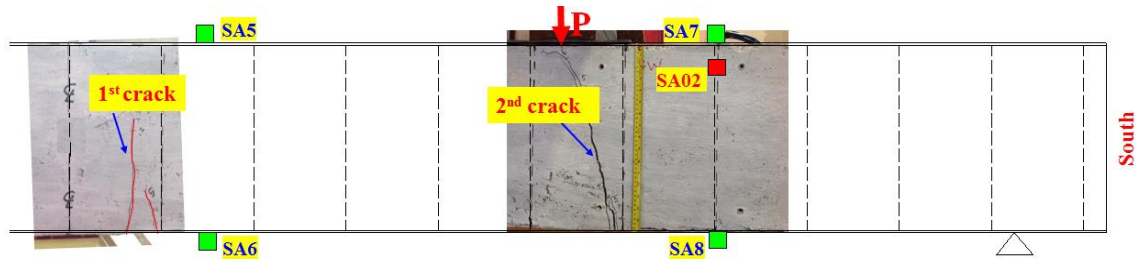


Figure 5-6 Details of cracks on south side of SC1 after loading

Since all major cracks occurred from the bottom of the beam, then developed to the top of the beam, no cracks happened between the path from the actuator SA01 to the sensor SA1. In addition, the bond slips between the steel plates and concrete all appeared between the bottom plate and concrete. Therefore, no cracks and bond slips happened in the stress wave path between the actuator SA01 to the sensor SA1. The damage index of SA1 is shown in Figure 5-7. It can be clearly found that, throughout the test, the values of damage index for SA1 are all small which means very little structural damage exists between SA01 and SA1.

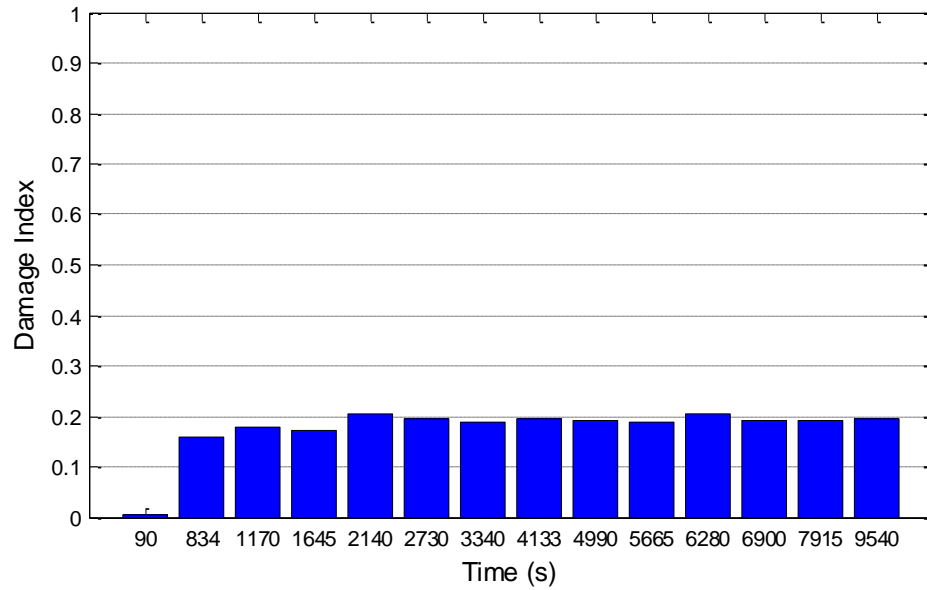


Figure 5-7 Damage index of SA1 on north side of SC1

From 0s to 1170s, the values shown in the damage index are very small which means the SC1 is in a health state. Then, a great value change from 1170s to 1645s can be observed from the damage index of SA2, as shown in Figure 5-8. According to Figure 5-5, no cracks existed on the path between SA01 and SA2. Then, the received stress wave of SA2 was not affected by any cracks. A bond slip event was supposed to happen on the bottom of the steel plate on north side. After the measurement point at 1645s, the value of the damage index of SA2 slightly increases till to the end of the test. Therefore, a major bond slip on the north side occurred from 1170s to 1645s can be determined by the experimental results.

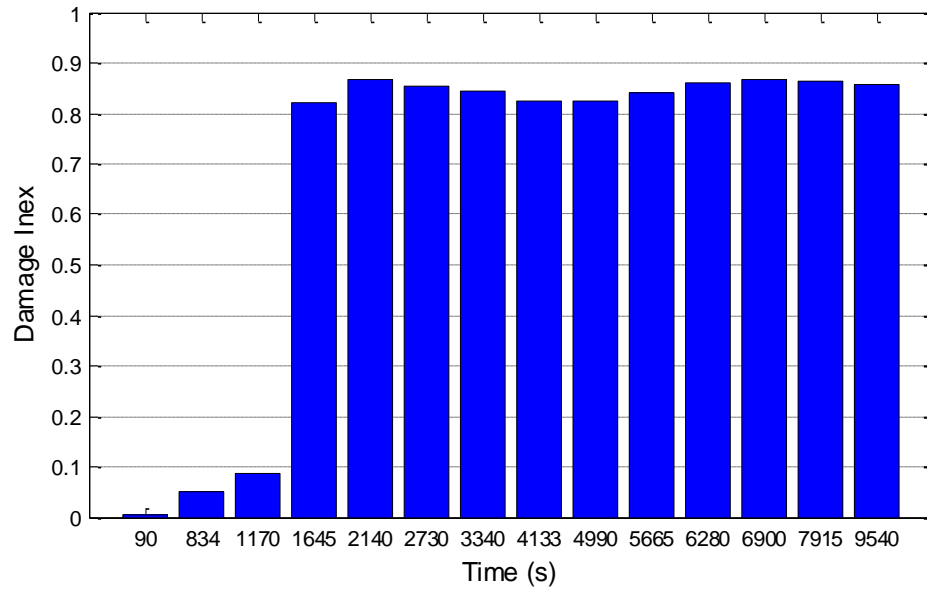


Figure 5-8 Damage index of SA2 on north side of SC1

From the visual check, the 3rd crack on north side of SC1 occurred at 2320s. The 3rd crack is on the stress wave path between SA01 and SA3. The damage index of SA3 shown as Figure 5-9 successfully detects the event. From the damage index, the value of damage index at 2140s is 0.2, but jumps to 0.3 from the next measurement at 2730s. This period is exactly the moment that the 3rd crack happened. The 3rd crack opened from the bottom of the steel plate and then extended upwards to the top of the steel plate. The damage index of SA2 also successfully monitored that development of the 3rd crack from 2730s to the end of the test. The increasing value of the damage index indicates the severity of the 3rd crack. When the test was almost finished, the value of the damage index is approaching to 0.5 which is almost two times then the value when the 3rd crack was appeared.

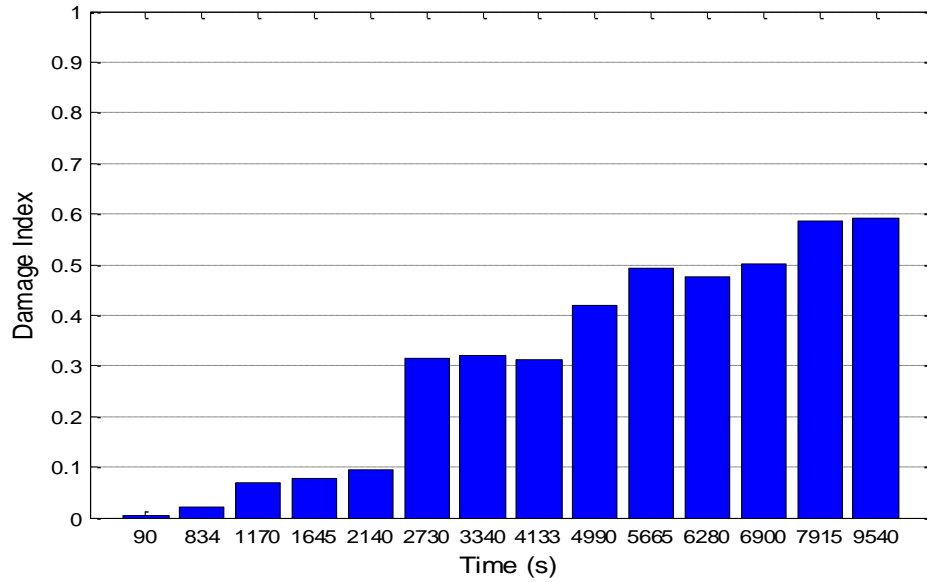


Figure 5-9 Damage index of SA3 on north side of SC1

The same result of the 3rd crack detection can be found in damage index of SA4, as shown in Figure 5-10. An obvious increase of the damage index value is presented at point 2140s and 2730s. Different from SA3, the early 3rd crack mainly crossed the stress wave path between SA01 and SA4 which means more stress wave energy was attenuated between SA01 and SA4 than SA01 and SA3. The value of damage index for SA4 at 2730s is 0.5 which is much greater than 0.3 presented from SA3. In addition, since the subsequent development of the 3rd crack departed the stress wave path between SA01 and SA4, the damage index of SA4 cannot monitor the crack development. The rest values of damage index for SA4 increase only from 0.5 to 0.7. The reason of the increasing values of the damage index after 2730s is maybe from the increasing width of the crack as the loading progressing.

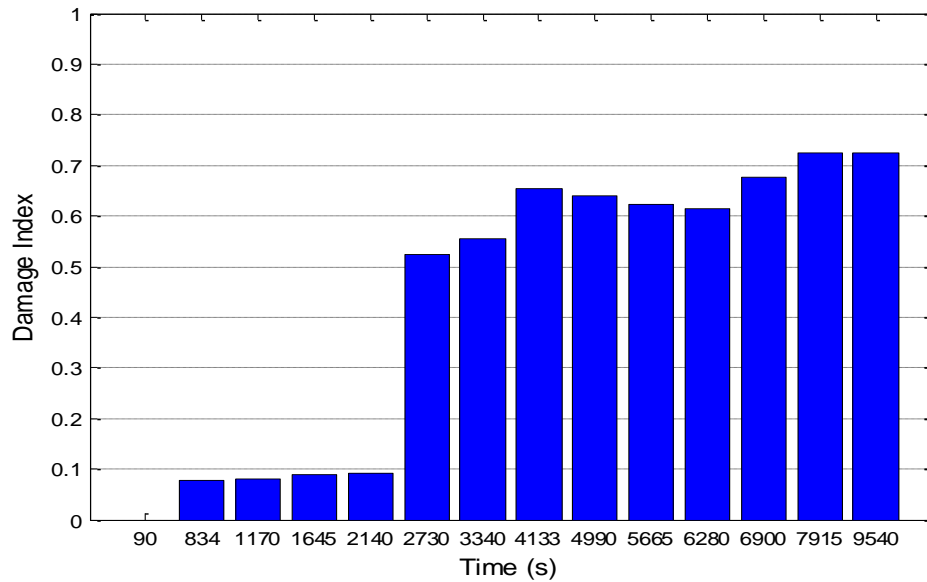


Figure 5-10 Damage index of SA4 on north side of SC1

In SC1 test, the 1st and 2nd cracks happened on south side of SC1, as shown in Figure 5-11. Since the 1st crack occurred away from any path between the actuator SA02 and its corresponding sensors, all damage indices on south side were not able to detect the 1st crack.

From the visual check and the curve of shear force vs. time, the 2nd crack happened on south side of SC1 at 1810s from the beginning of the loading. An increase value between 1645s and 2140s of the damage index for SA5 detected the appearance of the 2nd crack. The increasing trend of the values after 2140s shown in the damage index also monitored the crack development from the bottom to the top. Since the location of the 2nd crack on south side and 3rd crack on north side are kind of symmetrical to each other, the characteristics of the corresponding damage indices between SA3 and SA5 are similar.

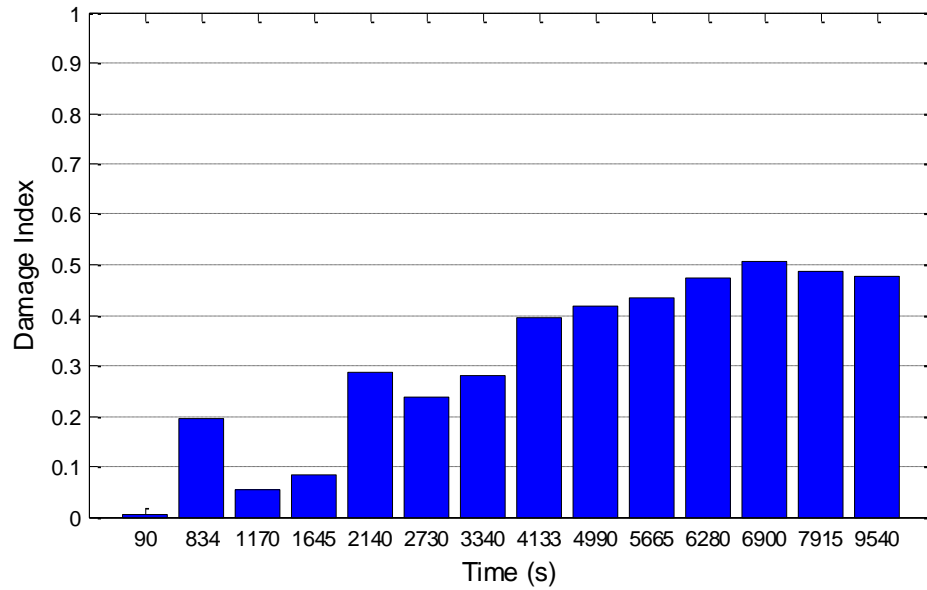


Figure 5-11 Damage index of SA5 on south side of SC1

A similar result of the calculated damage indices between SA6 and SA5 is not found. Comparing to the damage index of SA5, the increasing phenomenon of the damage index appeared between 834s and 1170s from the beginning of the loading as shown in Figure 5-12. This is the period when the 1st crack happened. One possible reason of the increasing value is that there may be a bond slip between the bottom plate and concrete around the location of SA 6 when the 1st crack happened. Due to the bond slip, the value of the damage index increases when the 1st crack happens, and then maintains the value between 0.4 and 0.5. Another possible reason is there may be a crack occurred inside the concrete between SA02 and SA6 in that period. The crack in the concrete can also attenuate the stress wave propagation energy and make the value of the damage index increase.

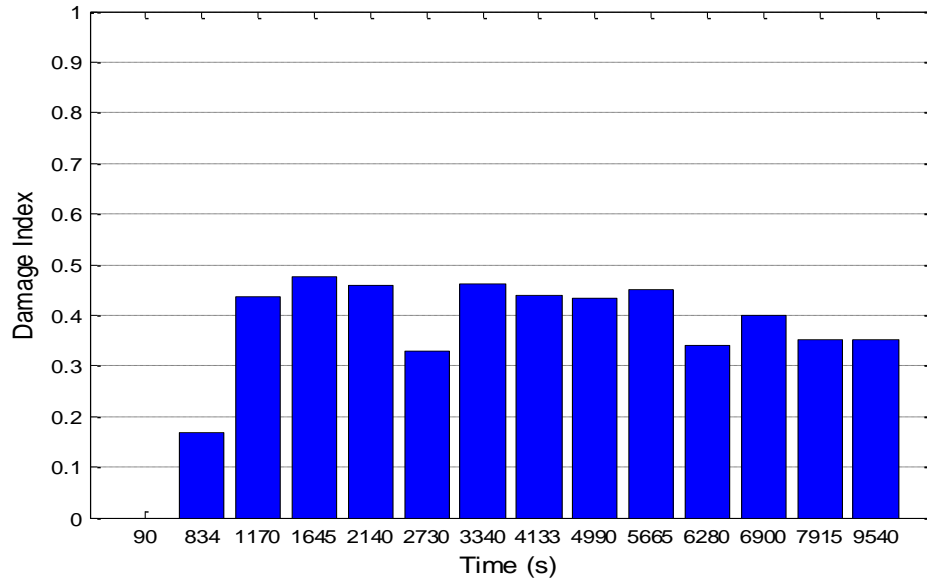


Figure 5-12 Damage index of SA6 on south side of SC1

Similar to the result of damage index calculated from SA1, no cracks and bond slips happened between the actuator SA02 to the sensor SA7. The damage index is shown in Figure 5-13.

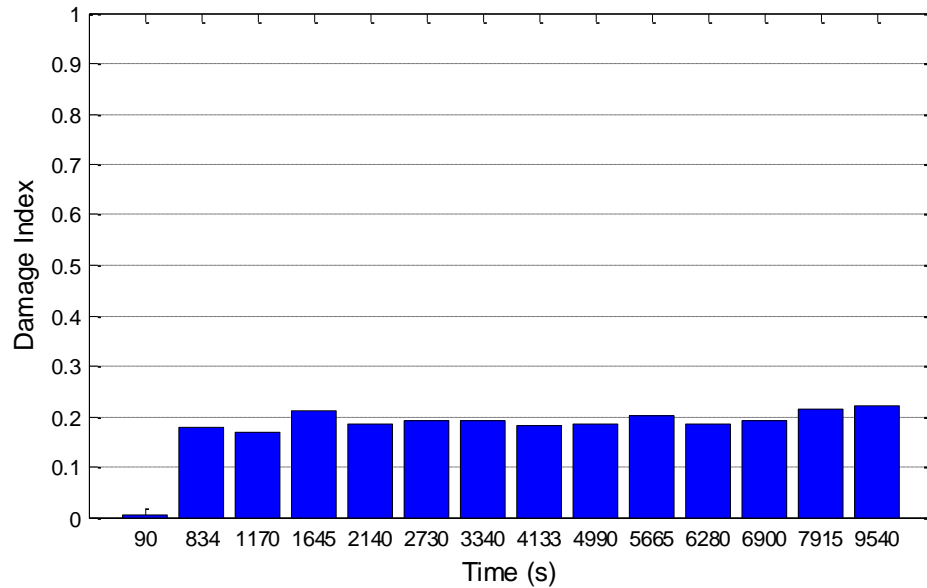


Figure 5-13 Damage index of SA7 on south side of SC1

A bond slip is detected between the bottom steel plate and concrete in the location around SA8. As shown in Figure 5-14, the value of the damage index of SA8 at 2140s is 0.9 which is three times than the previous measurement at 1645s. Since no cracks happened closed to the path between SA02 and SA8, it can be confirmed that a bond slip event occurred during that time. Since the 2nd crack opened from the bottom steel plate at 1870s, it may lead to a bond slip between the bottom steel plate and concrete in the local area. After the bond slip happened, the value of the damage index of SA8 will dramatically increase. From the trend of values after 1870s, it can be concluded that the bond slip at the bottom on south side degenerated as the loading progressing.

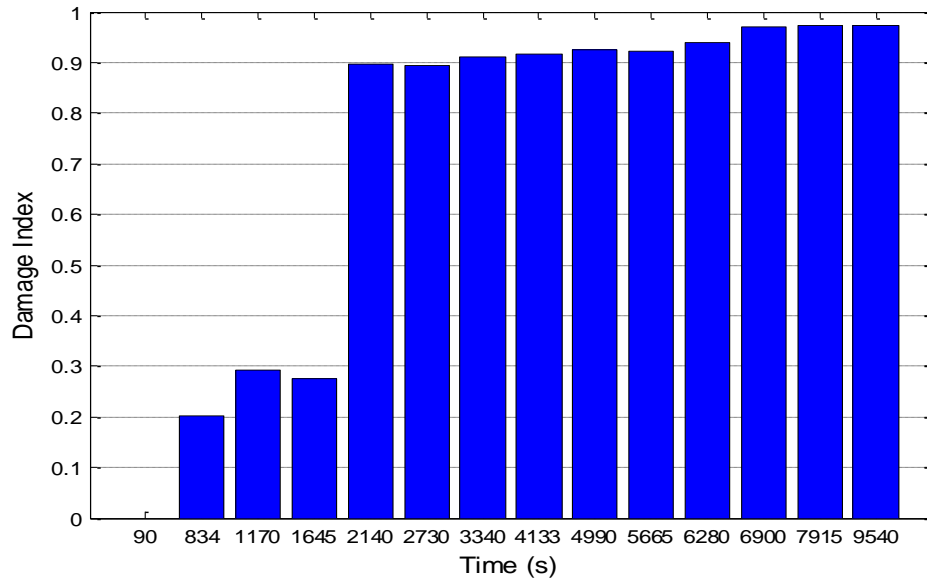


Figure 5-14 Damage index of SA8 on south side of SC1

5.3.1.2 SC4 test on north side

Since the distances of reinforcement bar are different from north side and south side, loading on north side and south side of SC4 were conducted separately. North side of SC4 was loaded first, and then the loading process was repeated on south side. The

loading process of on north side lasted around 9000s. After loading, five major cracks were observed from the beam. Figure 5-15 shows the location of the cracks on north side of SC4.

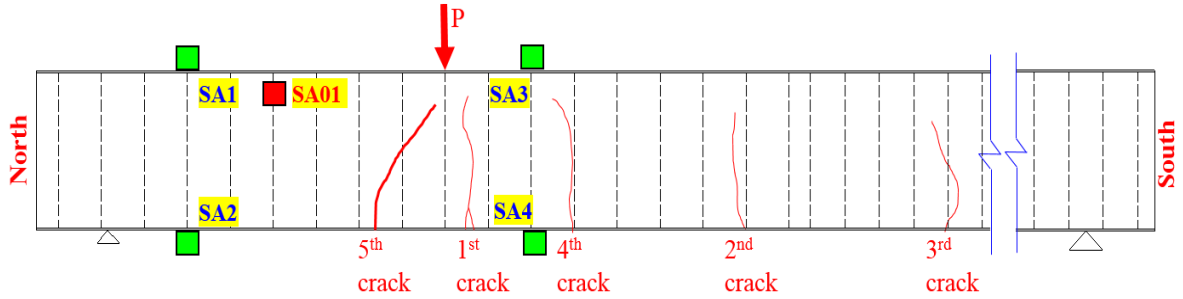


Figure 5-15 Details of crack on north side of SC4 after loading

Since no major cracks and bond slips happened between the stress wave paths from SA01 to SA1, the values of the damage index from SA1 are all small from the beginning to the end of the test, as shown in Figure 5-16.

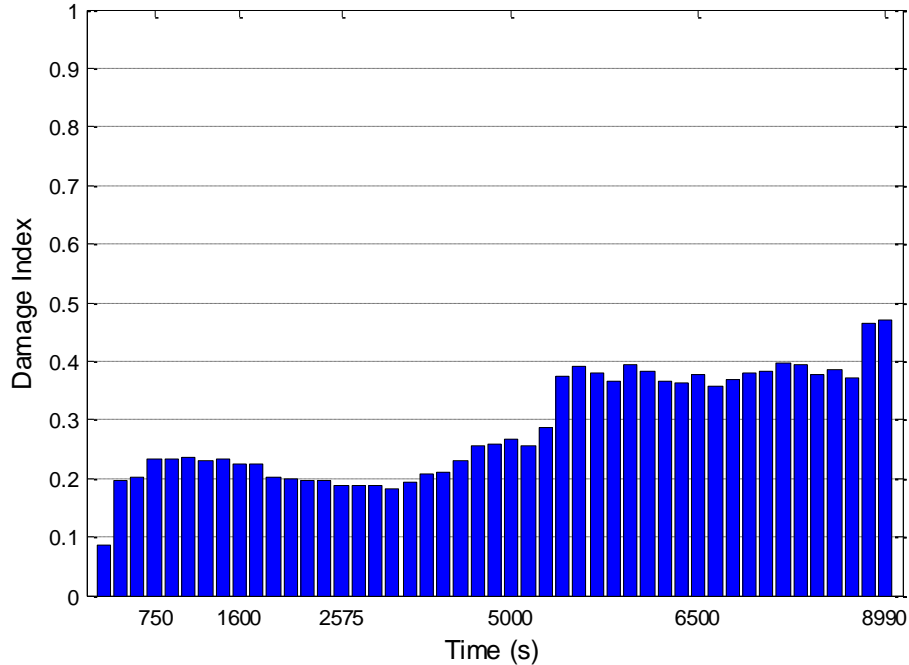


Figure 5-16 Damage index of SA1 on north side of SC4

Two obvious increasing values can be found in the damage index of SA2, as shown in Figure 5-17. Since no major crack was happened between SA01 and SA2, these two moments are bond slips between the bottom steel plate and concrete. The first bond slip was happened around 750s from the beginning of loading. The second bond slip was happened around 6500s. According to the visual check shown in Table 5-1, the first crack occurred at 705s from the beginning of loading. The first bond slip between the bottom steel plate and concrete may came from the first crack. In addition from the visual check, a visible bond slip happened around 6200s which is very close to 6500s presented in the damage index.

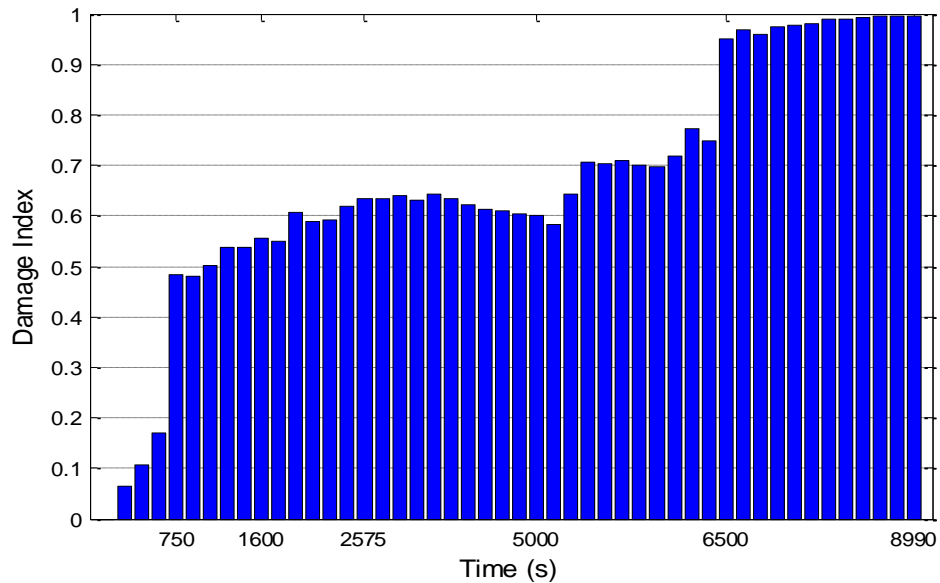


Figure 5-17 Damage index of SA2 on north side of SC4

Since the 1st crack exited on the stress wave path between SA01 and SA3, the 1st crack was detected by the damage index of SA3, as shown in Figure 5-18. The value of damage index at 750s is 0.6 which is much greater than the previous values. Therefore, the damage index of SA3 successfully detected the 1st crack occurred on north side of

SC4. After the 1st crack happened, the values of damage index continuously increase which indicate the development of the 1st crack. Meanwhile, the crack was also detected by the damage index of SA4 shown in Figure 5-19. The values of damage index dramatically increase at 750s. Since the early crack happened from the bottom of the SC4 and then develops to the top side, the values shown in the damage index of SA3 are smoothly increasing as the loading progressing. Another result found in Figure 5-18 is two extreme high values at the end of the damage index. In author's opinion, when approaching to the end of the test, the crack was further developed to the top side which led to higher energy attenuation from the actuator to the sensor. Correspondingly, the values of the damage index increased.

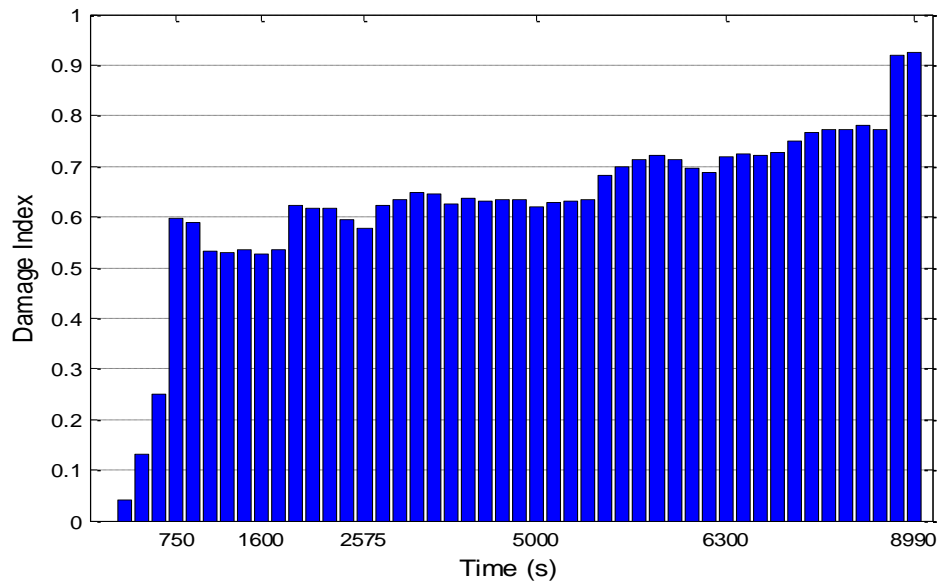


Figure 5-18 Damage index of SA3 on north side of SC4

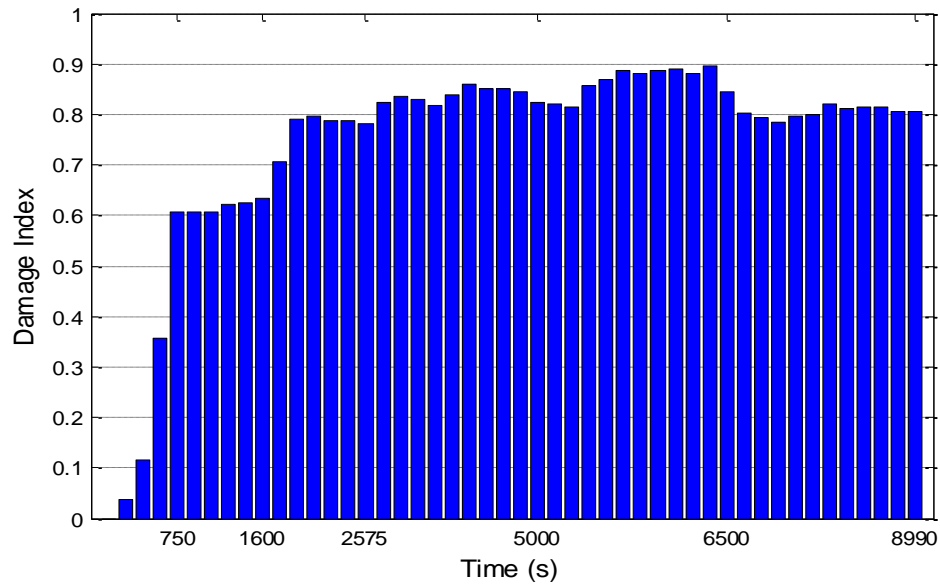


Figure 5-19 Damage index of SA4 on north side of SC4

5.3.1.3 SC4 test on south side

The loading process of on south side of SC4 lasted around 9500s. After loading, four major cracks were observed from the beam. Figure 5-20 shows the location of the cracks on south side of SC4. Please note that the view of Figure 5-20 is from the back side of the beam. In this test, SA7 lost communication from the data acquisition system, the damage indices are presented only for SA5, SA6, and SA8.

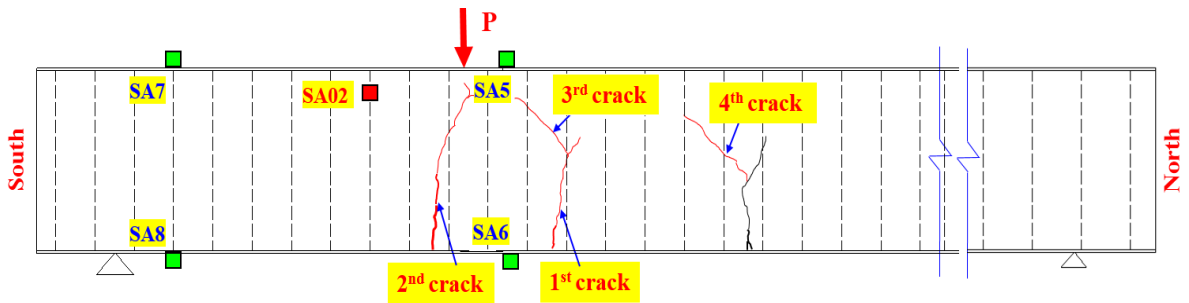


Figure 5-20 Damage index of SA4 on north side of SC4

In the test, the 1st, 3rd, and 4th crack were not on any of the stress wave paths between SA02 actuator and other SA sensors. These cracks could not be detected by the

SA sensors installed in the SC4 on south side. However, two value jumps can be observed from the damage index of SA5 at 975s and 2020s, respectively, as shown in Figure 5-21. 2nd crack is a visible crack which was verified. The time of 2nd crack is appeared at 1980s from the beginning of the loading. Therefore, the second value jump in the damage index of SA5 is associated with the 2nd crack. Another crack was supposed to appear inside the concrete around 975s according to the damage index. In addition, the value of the damage index continuous increase till to the end of loading which means the 2nd crack was developing along with the loading process.

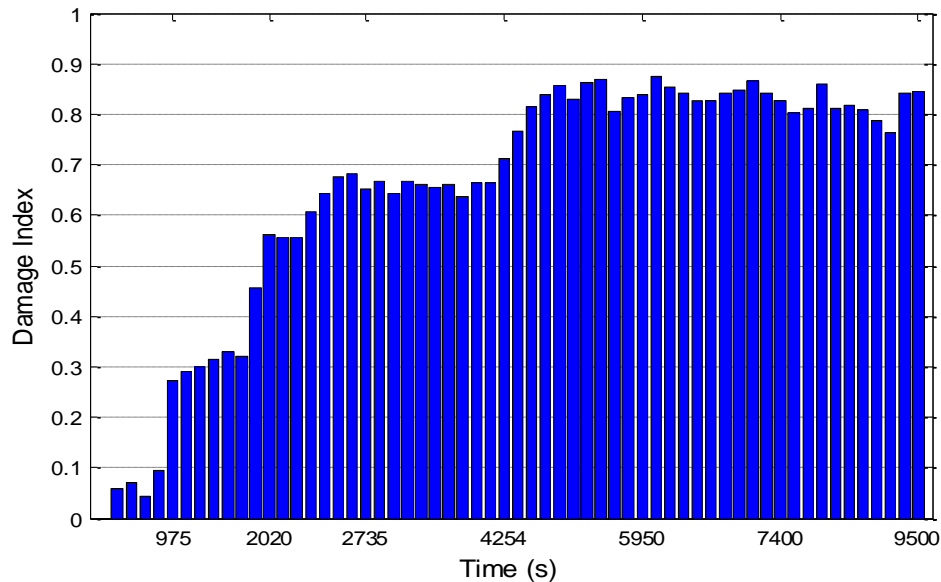


Figure 5-21 Damage index of SA5 on south side of SC4

The 2nd crack was also detected by SA6. As shown in Figure 5-22, the values of damage index in the beginning of the loading are very small. Then, the value jumps to 0.5 at 2020s. Different from SA5, the following development of the 2nd crack does not affect the stress wave propagation from SA02 to SA6, the rest values of the damage index of SA6 after 2020s just slightly increase.

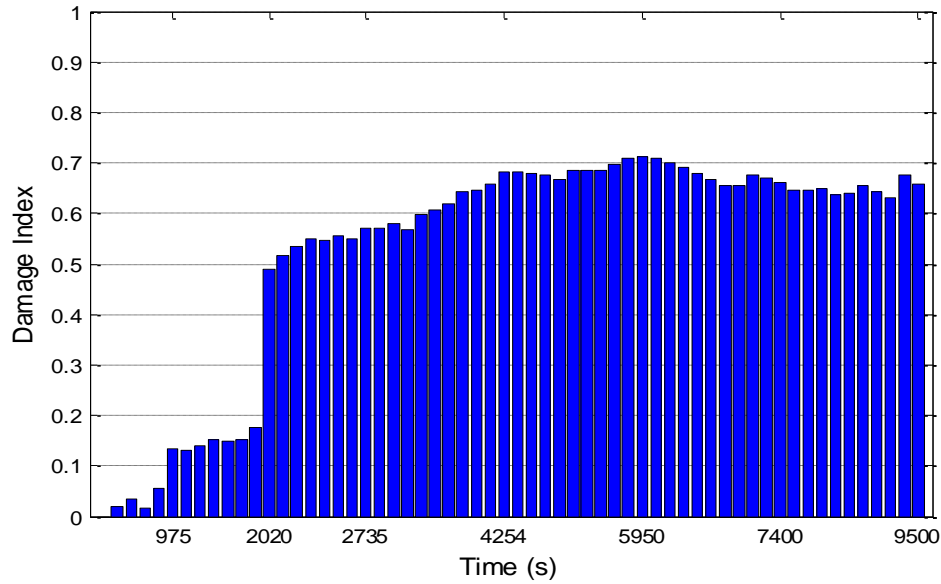


Figure 5-22 Damage index of SA6 on south side of SC4

The damage index of SA8 presents the bond slip phenomenon at the bottom steel plate, as shown in Figure 5-23. The values of the damage index are increasing as the loading progressing. It means that the bond slip between the bottom steel plate and concrete was developing from the beginning of the loading to the end. A visible bond slip was recorded at 3535s which is around 0.5 according to the value of the damage index. Before that, bond slip existed but cannot be by visual inspection. When the value of the damage index reaches to 0.5, the bond slip between the bottom steel plate and concrete becomes more serious which can be monitored by visual check.

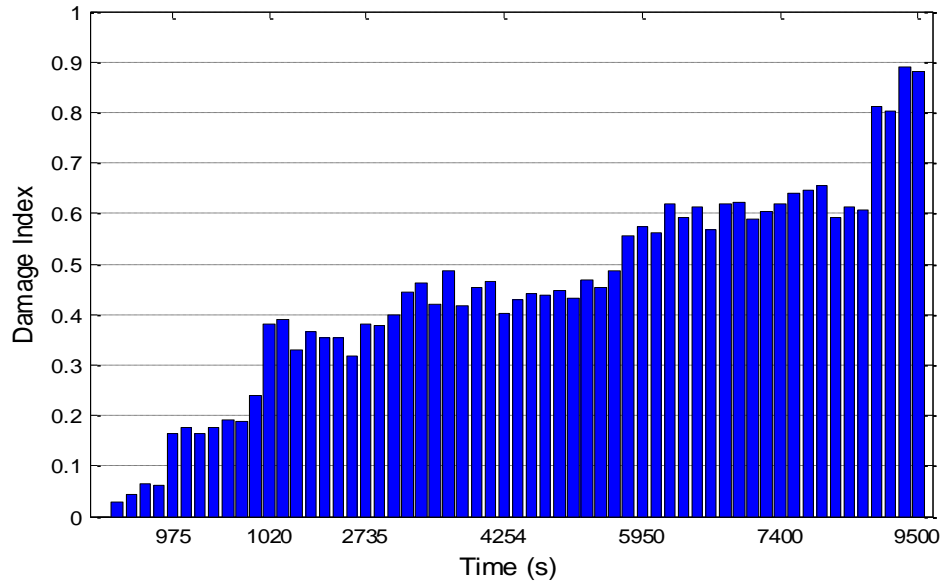


Figure 5-23 Damage index of SA8 on south side of SC4

5.3.1.4 Discussions

The location of cracks appeared vertically and cracks always developed from the bottom of concrete to the top side of concrete. Major bonding slips all happened between the bottom steel plate and concrete on both sides. As test results and analysis indicated before, sensors SBS and NBS in SC1 and SC4 captured initial stage and development of bond slip successfully. Figure 5-24 presents the shear force corresponding to damage indexes of SBS and NBS in SC1 and SC4. From SC1 to SC4 north and south, increasingly higher shear reinforcement ratio ($\rho_{t,test}$) was provided as given in Table 5-2. As more shear reinforcement was provided, SC beam could resistant larger shear force with significantly lesser damage caused by bond slip. This was especially true when shear force was larger than 10 kips, as shown in Figure 5-24. In the unique plateau stage of SC4 south, despite small fluctuation as marked in Figure 5-24, damage index was 0.60 and shear force was 52.50 kips (233.53 kN). It is clear that cross ties in SC beams can be

an effective method to improve bond between concrete and steel plate. Meanwhile, cross ties as shear reinforcement can evidently improve ductility and shear strength of SC beams. Therefore, shear design of SC beams conforming to the proposed minimum shear reinforcement ($\rho_{t,min}$) is acceptable.

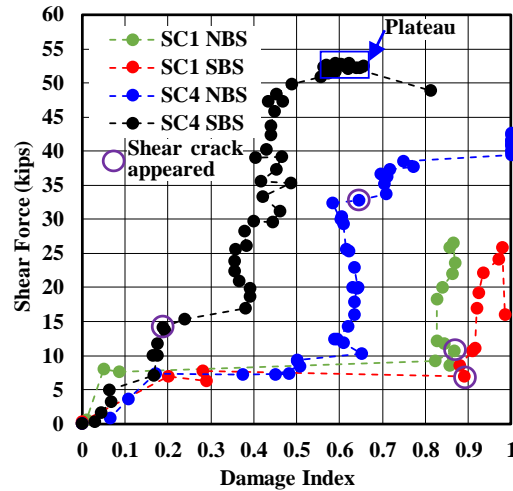


Fig. 1 Figure 5-24 Shear force vs. damage index of SC1 and SC4

5.3.2 Experimental setup and procedures

5.3.2.1 Detailed information of test beams

Two SC beams (SC1 to SC4) have been tested at Thomas T. C. Hsu structural research laboratory, the University of Houston. The length, width, and depth of each SC beam are 15.0 ft. (4572 mm), 12.0 in. (304 mm), and 16.0 in. (406 mm), respectively.

Table 5-2 shows the detailed information of the test beams. The shear span-to-depth (a/d) ratio and cross ties ratio ($\rho_{t,test}$) are measured before the experiments started. Kani (1964) found that Reinforced Concrete (RC) members subjected to concentrated load exhibits the minimum shear strength when the shear span-to-depth (a/d) ratio is

about 2.5. This phenomenon was also verified by Laskar et al., in tests on Prestressed Concrete (PC) beams. Laskar et al., proposed the minimum amount of shear reinforcement for PC member, which is a double of ACI 318 provision for a/d between 2.0 to 4.0.

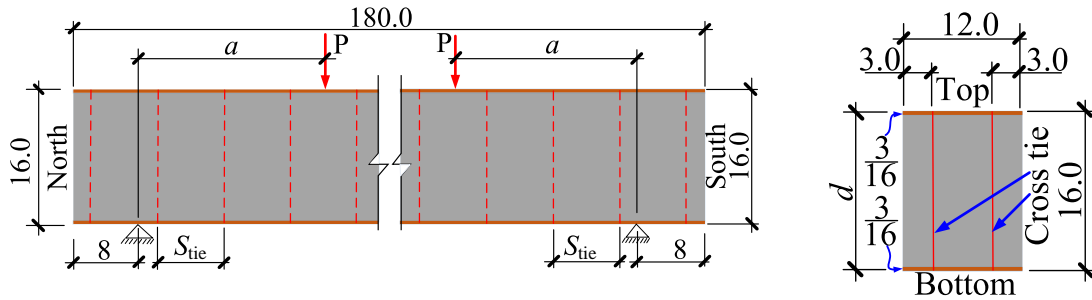
Table 5-2 Detailed information of the test beams

Specimen	a/d	$S_{tie}^{\#}$ (in.)	f_c^{t*} (ksi)	$\rho_{t,ACI}$ (%)	$\rho_{t,test}$ (%)	$\rho_{t,test}/\rho_{t,ACI}$
SC1 north	2.5	8.00	8.13	0.111	0.102	0.92
SC1 south	2.5	8.00	8.13	0.111	0.102	0.92
SC4 north	2.5	5.00	7.37	0.106	0.164	1.54
SC4 south	2.5	4.00	7.37	0.106	0.205	1.93

S_{tie} is the spacing of cross ties.

* f_c' = the concrete compression strength from concrete cylinder (6.00" \times 12.0"), tested on the testing day (over 28 days)

To fully secure the connections between steel plates and shear reinforcement, penetration welding was applied. The holes on top and bottom plates were drilled at the desired spacing, and then the shear reinforcement bar (cross tie) was placed. The welding was applied on both outside and inside surface of steel plates. The shear span a , as shown in Figure 5-25(a), is defined as the distance from center line of the support to the center line of the actuator, and the depth d , as shown in Figure 5-25(b), is defined as the distance from the extreme top fiber to the center line of the bottom steel plate. Please note that a/d value of each beam were carefully determined as 2.5 which is a possible value for the test beams to exhibit shear strength under the load. Figure 5-26 shows a photo of the completed steel plates connected with welded reinforcement bar for SC1.



(a) Elevation view of SC beam specimens

(b) Cross section dimensions

Figure 5-25 Dimensions of SC beam specimens (unit: inch)

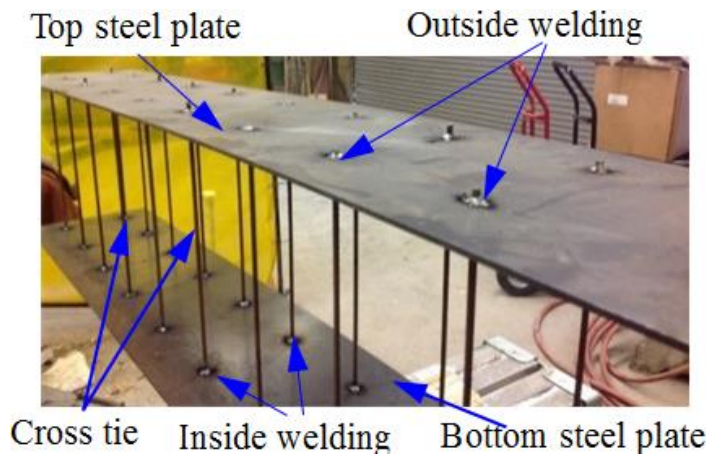


Figure 5-26 A photo of steel plates with welded reinforcement bar for SC1

5.3.2.2 Sensor installation and location

Several smart aggregates used as actuators were fixed between reinforcement bar using zip ties before placing concrete. Other smart aggregates used as sensors were attached to the outside steel plates using Epoxy. The sensor location of each beam is shown in Figure 5-27 and Figure 5-28, and the detailed photo of installed smart aggregates is shown in Figure 5-29. For each beam, SA01 and SA02 were used as actuators. SA1 to SA8 were used as sensors.

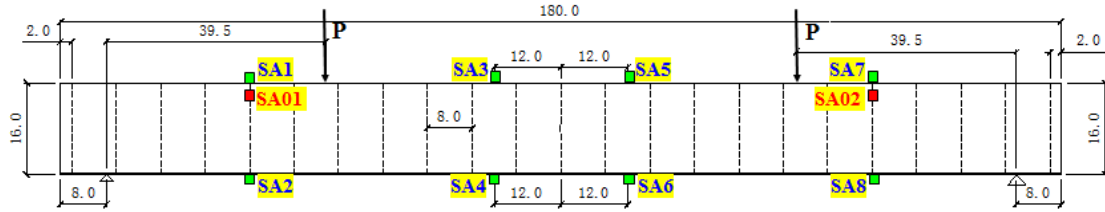


Figure 5-27 Location of smart aggregates in SC 1 (Unit: Inch)

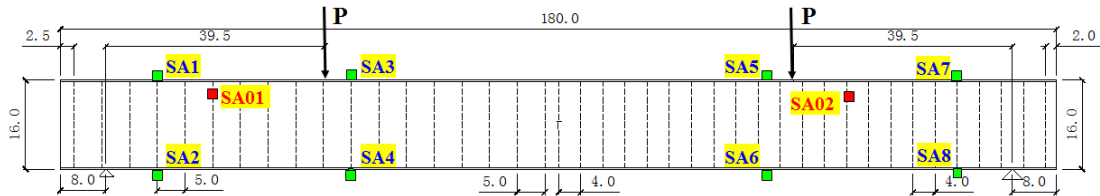


Figure 5-28 Location of smart aggregates in SC 4 (Unit: Inch)



Figure 5-29 Smart aggregate fixed between reinforcement rebar (left) and attached on steel plate (right)

5.3.2.3 Instrument setup

In each beam test, a function generator (Agilent 33120A) was applied to produce a repeated swept sine wave to the actuators (SA01, SA02). In order to generate a higher power excitation signal, a power amplifier was also utilized. The amplitude of the swept sine wave signal is 3V and the frequency range is from 100 Hz to 150 KHz. The gain of the power amplifier is 50. A data acquisition system combined with a NI USB 6361 and a laptop was used to record the received data collected from smart aggregate sensors. The

schematic of experiment instrumentation is shown in Figure 5-30 and the experimental setup of SC1 is shown in Figure 5-31.

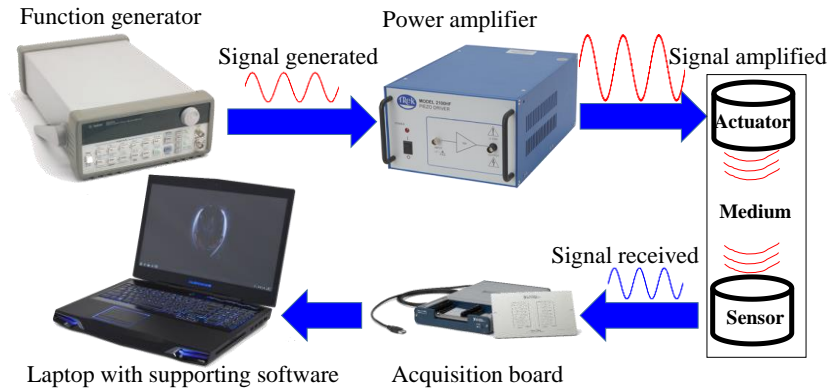


Figure 5-30 Experimental diagram

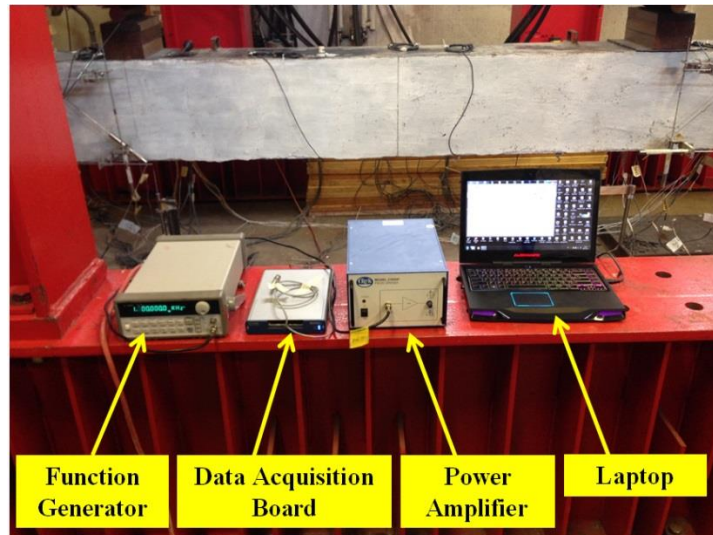


Figure 5-31 Experimental setup of SC1

5.3.2.4 Loading protocol

The specimens were subject to vertical loading provided by north and/or south actuators with a capacity of 600 kips (2670 kN) each. The loads and displacements of the actuators were controlled by the MTS Flex system. The loading protocol was comprised of several loading steps. Every loading step had a constant loading rate of 0.10 in. (2.54

mm) per 15.0 minutes. During each loading step, the loading might be put on hold and resumed, to check and mark the cracks. Each test lasted 3 to 5 hours. The displacement control feature was essential in capturing the post ultimate behavior of SC beams.

SC1 was loaded at both north and south sides, simultaneously. For SC4, north and south sides were loaded separately. The loading actuators and the casted concrete beam of SC1 are shown in Figure 5-32.



Figure 5-32 The loading actuators and the casted concrete beam of SC1

5.4 Summary

This chapter concentrates bond slip detection by using smart aggregate based active sensing approach. Two steel plate concrete beams were investigated. Since the stress wave propagation is high sensitive to the debonding condition between steel plates and concrete, active sensing approach using smart aggregates can be utilized to detect bond slip initiation and the development. Distributed sensors on the steel plates provide detailed information form bond slip condition in different locations. The wavelet packet-based structural damage index can offer quantitative values determine the bond slip development.

6 Water presence detection in concrete cracks

6.1 Introduction

Aging infrastructure all around the world demands significant focus and expenditure. Most of aging infrastructure is concrete structure. Health monitoring of concrete structure has been studied for many years. Although the study has been ongoing for many years, the detection of liquid presence in concrete cracks rarely attracts enough attention. However, the detection of liquid presence in concrete cracks is significant for the concrete health condition. In underground containment for nuclear materials, cracks and underground water are a lethal combination to migrate the radioactive pollution. For another example, the detection of liquid presence in concrete cracks for concrete dams is highly in demand. If water remains in concrete cracks for a long time, the erosion of the concrete interface and embedded rebar may cause a sustained damage and can even lead to complete structural failure of the concrete dam. Therefore, the detection of liquid presence in concrete cracks is essential and meaningful to the concrete structure facilities.

Moisture detection of concrete structures is another field that attracted concerns in recent years. Multon *et al.*, presented some quantitative results to describe the moisture transfers in a concrete beam using weighing and gamma densitometry [127]. Yeo *et al.*, successfully developed the Fiber Bragg Grating (FBG) sensors with moisture sensitive polymer coating to measure the moisture content of different concrete samples [128]. Ong *et al.*, applied the wireless, passive embedded sensor to real-time monitor the water content. Water in concrete can also be detected by analyzing the propagation velocity of

ultrasonic waves [129]. A disadvantage of this method is its cost and lack of robustness, in that bulky equipment is required.

In this chapter, a smart aggregate based active sensing system is proposed to detect concrete crack and the further water presence. Two simple experimental verifications were first performed to proof the feasibility of the proposed method. A concrete beam with three embedded smart aggregates was investigated. The wavelet packet-based energy analysis was used to determine three conditions of the concrete beam: health condition, crack condition, and the condition of water presence in the crack.

6.2 Detection principles

The active sensing based water detection relies on the change of received stress wave energy. Figure 6-1 is a schematic diagram of stress wave propagation through a concrete crack between smart aggregates. The left smart aggregate is utilized as an actuator to generate a desired stress wave which can be detected by the sensor. The right smart aggregate is utilized as a sensor to detect the stress wave. When the crack appears in the concrete, it can be regarded as the stress relief which reduces the received stress wave energy. In this case, very little energy can be received from the smart aggregate sensor.

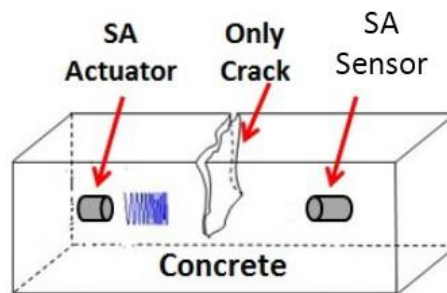


Figure 6-1 Schematic diagram of stress wave propagation through a concrete crack

Subsequently, liquid migrating into the concrete crack functions as the conduit of the stress wave and partly recovers the wave propagation, as shown below in Figure 6-2. The whole process of the water presence detection in a concrete crack is presented as the “interruption” of the stress wave transition when cracks form and the “recovery” when water migrates into the concrete crack. Since the stress wave propagation is sensitively related to the crack and water, the change of the received stress wave energy can be used as a significant indicator to present the crack and water condition in the concrete.

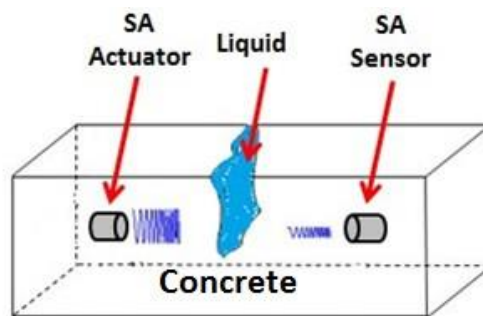


Figure 6-2 Diagram of stress wave propagation through a water filled concrete crack

6.3 Simple experimental verifications

6.3.1 Water existence detection

In this verification, two smart aggregates were fixed by clips with a 1mm gap between them, as shown in Figure 6-3. SA (1) was used as an actuator connected to a function generator (Agilent 33120A) and SA (2) was used as a sensor connected to an oscilloscope (Waverunner LT342). The smart aggregate actuator generated a swept sine wave by function generator. The start frequency and stop frequency of the excitation signal are 1Hz and 1MHz, respectively. The amplitude of the signal is 10V. The SA (2)

was used to detect the swept sine wave from SA (1). The amplitude of the wave was measured by the oscilloscope.

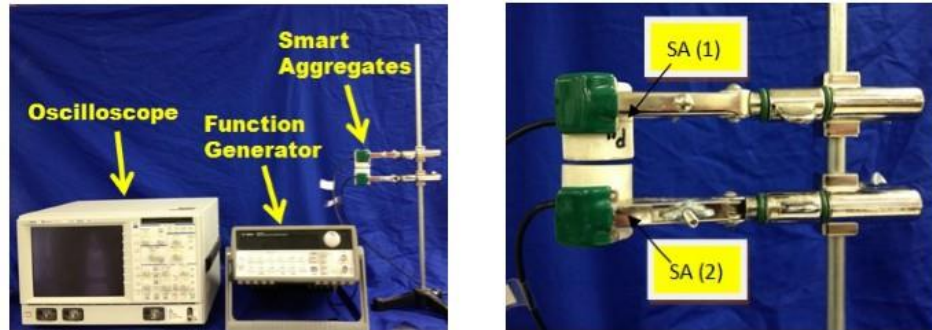


Figure 6-3 Experimental setup of water drop detection

The test was operated in two cases described as follows:

Case 1: The 1mm gap was open to the air. SA (1) generated a swept frequency sine wave from 1Hz to 1MHz and the signal amplitude detected by the SA sensor was measured by the oscilloscope.

Case 2: The 1mm gap was filled with water drops. The rest of the process was all repeated from Case 1.

Figure 6-4 presents the voltage amplitudes of the received sensor signal in two cases: (1) No water in the gap and (2) with water in the gap. The X-axis is a logarithmic coordinate of the frequency from 1Hz to 1MHz. The blue curve represents the sensor signal amplitude in “no water” drop case while the red curve depicts the sensor signal amplitude in “water” drop case. When the gap was out of water, the stress wave could hardly go through the air gap from the SA actuator to the SA sensor. Therefore, the received signal amplitude was very low. However, when the gap was filled with water, water functioned as a conduit of the wave path. Much more stress wave energy can go through the gap. The amplitude of the signal dramatically increased especially between

50 kHz-200 kHz. This test verified that the amplitudes of the sensor voltage were closely related to the crack and water between SAs.

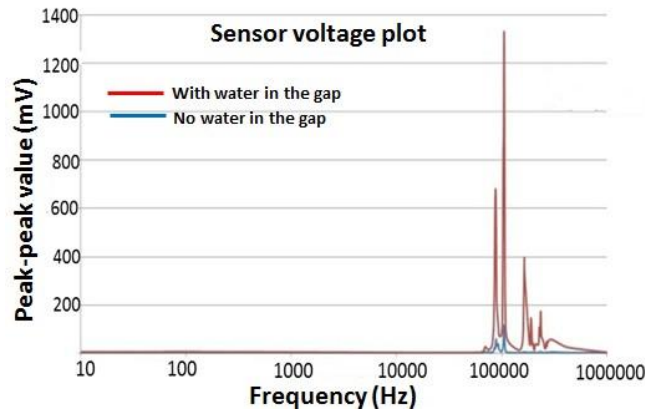


Figure 6-4 Sensor voltage plot in two cases

6.3.2 Water quantity detection

In this test, the SA1 (actuator) was embedded into a small concrete cylinder before casting and SA2 (sensor) was fixed by a clamp outside the concrete shown in Figure 6-5. An additional water layer is between these two SAs. The SA (1) generated a swept frequency sine wave from 1Hz to 1MHz and the SA (2) detected the signal response. The depths of the water between the concrete and SA (2) were set in three cases: (1) 1mm, (2) 2mm, and (3) 3mm.



Figure 6-5 Experimental setup of water quantity detection and the schematic diagram

Figure 6-6 shows the results of the sensor signal amplitude in different water depths. The amplitudes of the sensor voltage show a proportional trend of decreasing

voltage vs. increasing water depth. This test verified that the amplitudes of the sensor voltage correlated to the water quantity between SAs.

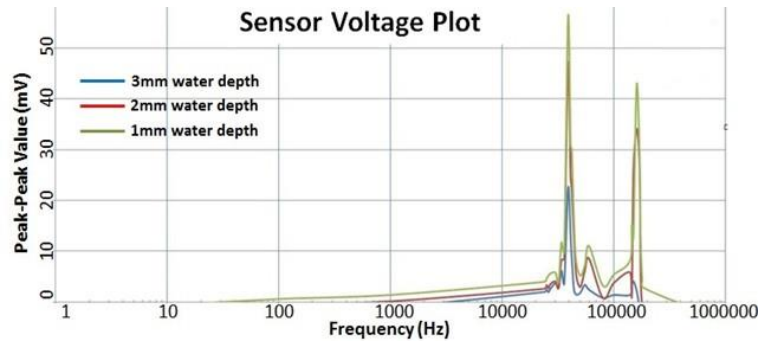


Figure 6-6 Sensor voltage plot in three cases

From these two simple experimental verifications, the active sensing approach successfully detected the water migrating case. The water functioned as the conduit to strengthen the stress wave propagation. Moreover, the verified tests provided potential feasibility to quantitatively monitor the water amount existed in the crack.

6.4 Water detection in a concrete crack

6.4.1 Experimental setup and procedures

Case 1: Concrete beam without crack

In the experiment, a cuboid concrete beam (18"×6"×3"), as shown in Figure 6-7, was casted. Three SAs were embedded in the pre-determined locations before casting. SA (0), as the actuator, was placed in the middle of the concrete beam. SA (1) and SA (2), as sensors, were placed 2 inch to the ends of the concrete beam. The rebar on the bottom of the concrete beam was used to enhance the strength of the concrete beam. The orientation and distribution of SAs in the concrete beam is shown in Figure 6-8.



Figure 6-7 Concrete Beam embedded with three smart aggregates

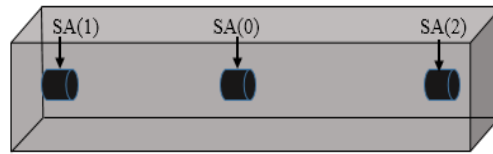


Figure 6-8 Orientation and location of smart aggregates

Case 2: Concrete beam with a large crack

A large artificial crack was made by the load equipment shown in Figure 6-9. A continuously increasing load was applied to the concrete beam. After the loading process, an artificial crack was generated on the left side of the concrete shown in Figure 6-10.



Figure 6-9 Experimental Setup of the loading process

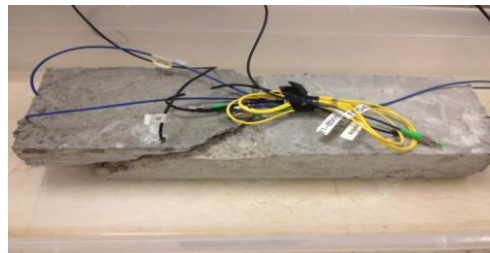


Figure 6-10 A photo of the concrete beam with a large crack after loading

Case 3: Water filled in the crack

In case 3, the whole concrete beam was stored in a water environment. Therefore, the water was completely filled in the concrete crack, as shown in Figure 6-11.



Figure 6-11 The concrete beam filled in a water container

In this experiment, SA (0) was used as the actuator to generate the desired swept sine wave using Agilent 33120A function/arbitrary waveform generator. The detailed parameters of the guided wave are shown in Table 6-1 while the graph of the sweep sine wave within 0.3 seconds' data length is shown below in Figure 6-12.

Table 6-1 Detailed parameters of the guided swept sine wave

Start Frequency	100 Hz
Stop Frequency	150 kHz
Amplitude	10 V
Period	1 s

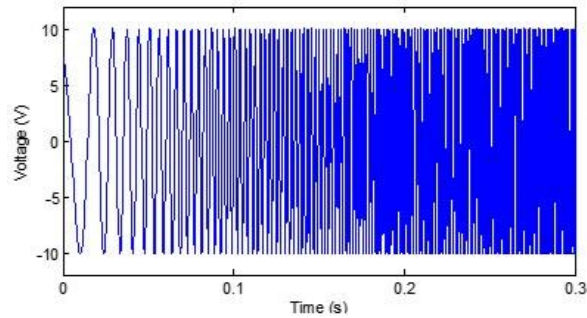


Figure 6-12 An example of swept sine wave lasted for 0.3s

6.4.2 Experimental results and discussions

6.4.2.1 Time domain analysis

In each case mentioned above, SA (1) and SA (2) were used as sensors to detect the stress wave generated by SA (0). The received sensor voltage plots, as shown below in Figure 16 demonstrated the sensor signal response. Figure 6-13(a), (c), (e) corresponded to SA (1) while Figure 6-13 (b), (d), (f) corresponded to SA (2). Each of the signal graphics contained two periods of the sensor signal according to the swept excitation sine wave. Due to the artificial crack between SA (0) and SA (1), the stress wave propagation was extremely weakened and no signal response was detected. When the crack was filled with water, water functioned as a conduit of the stress wave path. As the result, the amplitude of the received signal increased shown in Figure (e). Figure 6-13 (b), (d), (e) presented the signal responses of SA (2). In comparison to the crack existence condition between SA (0) and SA (1), no crack formed between SA (0) and SA (2). On the other hand, when comparing Figure 6-13 (d) to Figure 16 (b), Figure 6-13 (d) demonstrated the same voltage level but a different signal response of the sensor voltage graphic. Figure 6-13 (f) indicates a slightly voltage value drop when the concrete beam is placed in the water environment. When the large crack formed in the concrete and the concrete beam was surrounded by water, the damping ratio and the stiffness of the concrete beam changed. The changed mechanical parameters significantly influenced the signal response between SA (0) and SA (2).

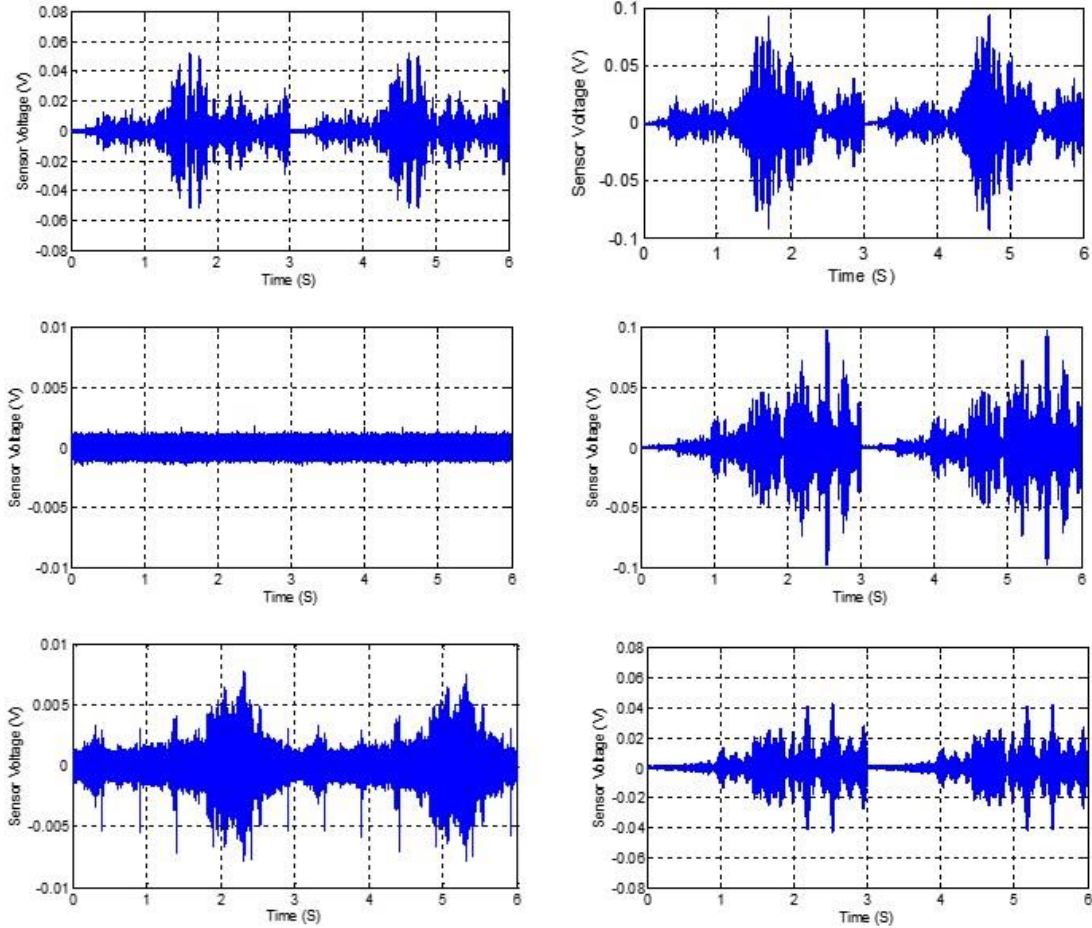


Figure 6-13 Sensor voltage graphic: (a): SA 1, no crack and no water; (b): SA 2, no crack and no water; (c): SA 1, with crack but no water; (d): SA 2, with crack but no water; (e): SA 1, with water in crack; (f): SA 2, with water in crack

6.4.2.2 Wavelet packet analysis: Sensor Energy Index

Based on the energy vector calculation with wavelet packet analysis, the sensor energy performance is presented in Figure 6-14. For SA (1), a sensor energy trend is demonstrated in cases of concrete beam without crack, with crack and water in crack. Without the crack and water, the received sensor energy level is close to 105, as shown with the left most blue bar. The large crack in the concrete beam reduces the sensor energy to the degree of 102, as shown with the left most green bar. When water is filled in the crack, the sensor energy rises to the degree of 103 shown with the left most brown

bar. For SA (2), the sensor energy maintains stable for all the cases, as seen in the right hand portion of Figure 6-14.

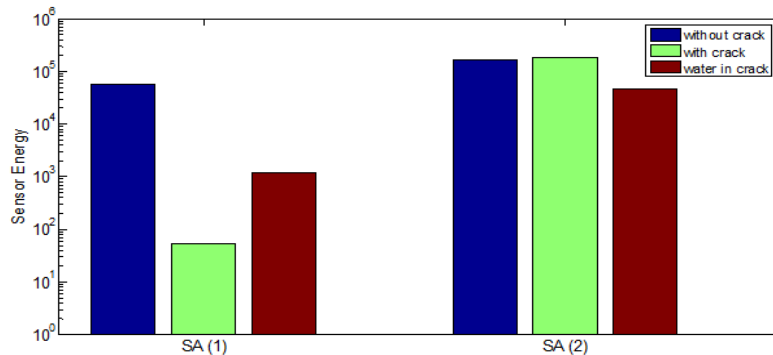


Figure 6-14 Sensor energy performance of SA (1) and SA (2) in three cases

6.5 Summary

In this chapter, concrete crack detection and the further water presence detection in the crack were experimentally studied. Two experimental verifications were performed prior to the experiment. The smart aggregate based active sensing system was verified to be an effective approach to detect water presence in the concrete crack. Crack in the stress wave path acts as a stress relief and attenuates the transition energy from the actuator to the sensor. Therefore, the amplitude of the received sensor voltage significantly reduces. However, the water filled in a concrete crack functions as a conduit and guides the excited stress wave to propagate through the crack. The water presence in the concrete crack can be confirmed by the increasing of the received sensor signal amplitude. In addition, a wavelet packet-based energy index in this research quantitatively indicates the received sensor energy level corresponding to different concrete conditions such as health status, large crack damage and water filled in the concrete crack.

7 Very early age concrete hydration monitoring

7.1 Introduction

Since the strength and durability of hardened concrete is mainly determined by the 28 days' curing during the concrete hydration process, researchers investigated much work on the early age concrete hydration monitoring, as concrete hydration is a fundamental process for concrete formation.

Temperature measurement is a traditional and common method that monitors the early age concrete hydration. Zou *et al.*, applied fabry-perot fiber optic temperature sensors to the concrete hydration and obtained the temperature changes in different water-to-cement ratios [130]. In order to better understand the temperature changes during the hydration, Azenha *et al.*, demonstrated both the internal and surface measurement of temperature fields in a $0.40 \times 0.40 \times 0.40$ m³ concrete cube with the help of infrared thermography technology and standard embedded sensors [131]. On the other hand, electro-mechanical impedance (EMI) based concrete damage detection has also been studied for many years [132][133]. Recently, concrete hydration characterization using EMI has been presented by many researchers. McCarter *et al.*, innovatively developed the EMI technique into Portland cement paste and found that the impedance of the concrete is sensitively related to the concrete hydration process [134]. Wave propagation based concrete hydration monitoring has also actively received attention. Ultrasonic wave measurement is the most popular method that showed much potential to reflect the change of the concrete properties [135][136][137][138]. Zhang *et al.*, compared both the electrical resistivity and ultrasonic techniques for the concrete

hydration monitoring during the first 7 days and identified 4 stages of the concrete hydration condition [139]. On the other hand, Song et al., proposed the smart aggregate based active sensing approach for structure health monitoring [63]. Consequently, Song *et al.*, and Gu *et al.*, employed smart aggregate based active sensing method to monitor strength development during the early age concrete hydration process from day 1 to day 28 [86].

However, the quality of concrete hydration is highly influenced by the very early age (0-20 hours) performance when concrete is under intensive reaction. The research related to the very early age concrete hydration monitoring has not received much attention. Xu *et al.*, evaluated different calorimetric test methods that showed comparison results using Isothermal and semi-adiabatic temperature prediction approaches for the first 80 hours during the concrete hydration [140]. Yang *et al.*, measured the admittance of a reusable PZT sensor with an impedance analyzer and employed the RMSM method to indicate the concrete hydration characteristics within the first 48 hours after casting [36]. Branco *et al.*, presented a numerical method dealing with environmental interaction and concreting phases to measure the temperature and stress characterization during the first day after casting [141].

In this chapter, the very early age (0-20 hours) of concrete hydration process was researched based on an innovative active sensing approach complemented with smart aggregates. The very early age concrete hydration is a very significant stage, where concrete experiences a complicated chemical reaction from liquid stage to hardened stage during the first 20 hours after concrete casting. Additionally, a comparison study of the

proposed method in concrete hydration monitoring with different modes of smart aggregates was experimentally researched in a small-scaled concrete beam.

7.2 Very early age concrete hydration monitoring using smart aggregates

7.2.1 A concrete beam test using compressive mode smart aggregates

7.2.1.1 Experimental setup and procedures

The experimental setup for the smart aggregate based concrete hydration monitoring is shown in Figure 7-1. The two smart aggregates were fixed to a rebar prior to concrete casting. In this concrete specimen, the distance between the two rebar which were used to install the two smart aggregates was 50.8mm. Since the distance of the pair of smart aggregates was only 50.8mm (two inches), which was much smaller than the size of the concrete beam, the complex geometry of the host concrete structure had very little effect to the results of concrete hydration monitoring. A function generator (Agilent 33120A) produced a sinusoidal wave signal to one smart aggregate (Actuator) while the response signal was received from the other smart aggregate (Sensor). Two types of signals were used. One is a swept sine wave and the other is a constant frequency sine wave. The probing signal produced from the actuator was received by the sensor and recorded using a data acquisition system. The sampling rate for the data acquisition system was 500 kS/s. The parameters of the swept sine wave are shown in Table 7-1. In this experiment, a Texas Department of Transportation (TxDOT) traditional concrete mix was used, as shown in Table 7-2. The schematic diagram of the experimental setup is shown in Figure 7-2.



Figure 7-1 (a) smart aggregates installed beside reinforcement rebar (b) A photo of the test concrete beam after casing



Figure 7-2 Schematic diagram of the experimental setup

Table 7-1 Parameters of the Swept Sine Wave

Start Frequency	50 kHz
Stop Frequency	100 kHz
Period	3 seconds
Amplitude	10 V

Table 7-2 Composition details of the TxDoT traditional concrete mix

Cement	519 lb/yd ³
Fly Ash	248 lb/yd ³
Coarse aggregate	1899 lb/yd ³
Fine aggregate	1156 lb/yd ³
Water/cement ratio	0.43
Water/cementitious ratio	0.30
HRWR/Supperplastizer	20 fl.oz./cwt
Retarder	3 fl.oz./cwt

7.2.1.2 Experimental results

The hydration process of the concrete beam was monitored for 17 hours. The swept sine excitation signal used in the test had a frequency range from 50 kHz to 110

kHz and its period was 3s. Utilizing the active sensing approach, the sensor continuously received the propagated wave signal transmitted from the actuator. Since ultrasonic wave propagation is greatly sensitive to the medium and the wave frequency, the collected response signal presented a different amplitude variation trend for both the time domain and frequency domain during the concrete state transition from liquid state to hardened state. Through analyzing the characteristics of the collected signals, three stages of the concrete hydration process were classified.

7.2.1.2.1 Three stages during the very early age of concrete hydration

7.2.1.2.1.1 Fluid stage

Figure 7-3 shows the time domain signal response of the fluid stage in 15 minutes intervals from concrete hydration from the beginning of the test to the end of the first hour. Each plot presented a complete period sensor signal according to the excitation swept sine wave. Due to the initial formation of bubbles and the high damping of fluid concrete, the amplitudes of the collected sensor signal were very weak in the first hour, producing signals of less than 10 mV. The Fourier Transform was also utilized to further frequency analysis of the received signal. Figure 7-4 presents the signal frequency response according to each time domain signal. From the plots, the magnitudes of the signal in the first hour were all lower than -100 dB. However, two small frequency peaks could be observed around 65 kHz and 95 kHz. Both the time domain and frequency domain signal responses concluded that concrete hydration during this stage was quite steady and stable. Considering the characteristics of the sensor signal in the first hour, the concrete hydration stage was classified under the fluid stage.

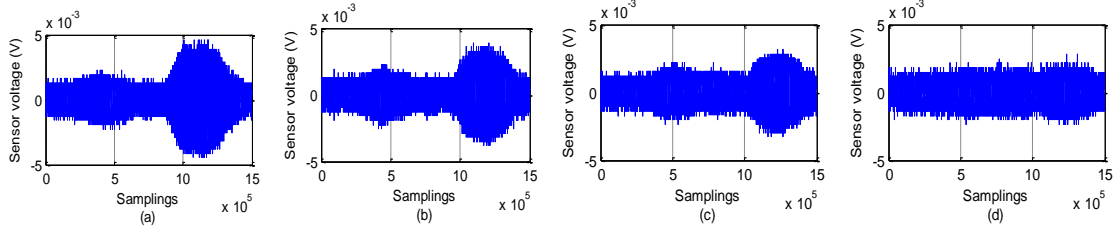


Figure 7-3 Time domain signal response of the fluid stage at (a): 15 minutes; (b): 30 minutes; (c): 45 minutes; (d): 1 hour

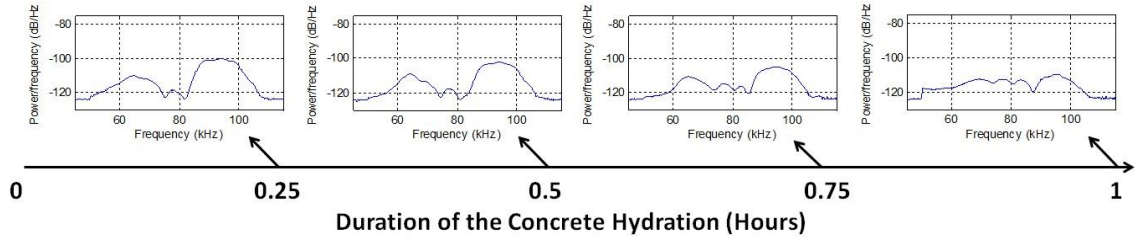


Figure 7-4 Frequency domain signal response of the fluid stage

7.2.1.2.1.2 Transition stage

Compared with the liquid stage, the amplitudes of the collected signal were much higher and the “shapes” of the collected signals constantly changed. As depicted in Figure 7-5, these signal responses are higher from 1 hour to around 7.5 hours. It can therefore be concluded that more energy could be propagated through the concrete between two smart aggregates and the concrete status was disparate as the hydration process was ongoing. Throughout this stage, the concrete's strength increased rapidly. Consequently, the ultrasonic wave transmission through the hardening concrete became more intense. This stage is classified as the concrete transition stage from the liquid stage to the hardened stage. From Figure 7-5(a)-(f), the sensor signal representations were completely different, which meant that the concrete hydration reaction was strong during 2 hours to 6 hours. Meanwhile, from Figure 7-5(g)-(h), the sensor signal began to present a similar trend, which indicated that the hydration was approaching stability after 6 hours.

Additionally, the collected signals in the frequency domain shown in Figure 7-6 also verified the phenomenon. The magnitudes of the sensor signal in the transition stage were all higher than that in the liquid stage. From observation, the frequency response of the sensor signal was chaotic from 2 hours to 6 hours and gradually trended to be stable after 6 hours from the concrete hydration process.

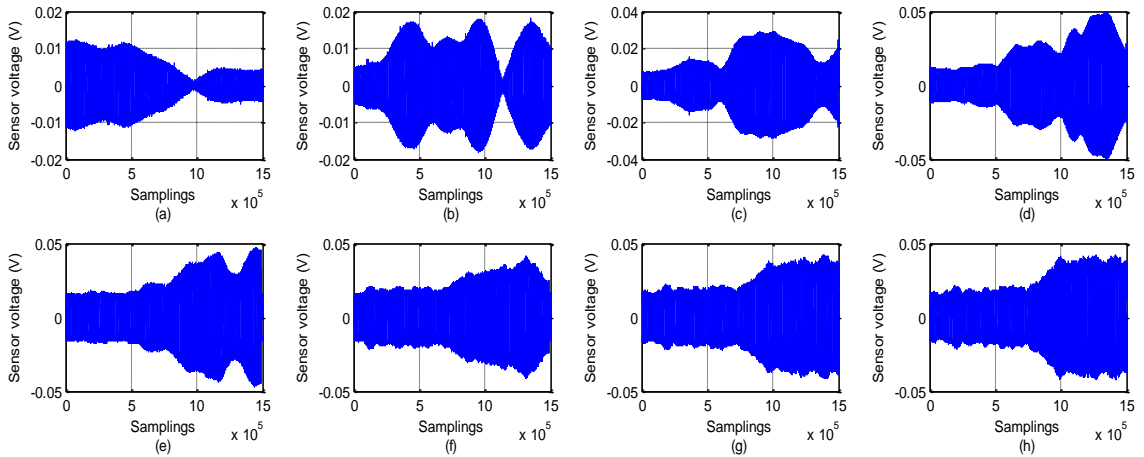


Figure 7-5 Time domain signal response of the transition stage (a): 2 hours; (b): 3hours (c): 4hours (d): 4.5 hours (e): 5 hours (f): 6 hours; (g): 7 hours (h): 7.5 hours

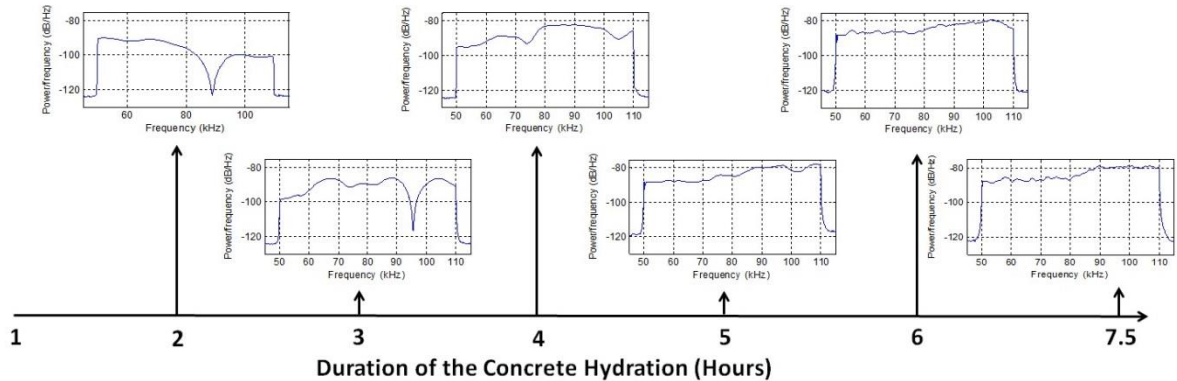


Figure 7-6 Frequency domain signal response of the transition stage

7.2.1.2.1.3 Hardened stage

The hardened stage started from 7.5 hours after casting, during which the concrete had transitioned into the solid state, when the structure in the concrete became hardened.

Comparing with the two prior stages, the sensor signal in the hardened stage shown in Figure 7-7 was extremely smooth and stable. Since the concrete structure was mostly solidified in this stage, the received ultrasonic wave energy from 7.5 hours to 17 hours did not show much change. The amplitudes of the sensor signal were also greater than the previous two stages due to increased strength. The frequency domain sensor signal shown in Figure 7-8 presented the same stable trend in the hardened stage. After 7.5 hours from the concrete hydration, the frequency response of the signal was almost the same. Therefore, both the time domain and frequency domain signal response were steady, which verified that the concrete structure in the hardened concrete hydration stage was quite consistent.

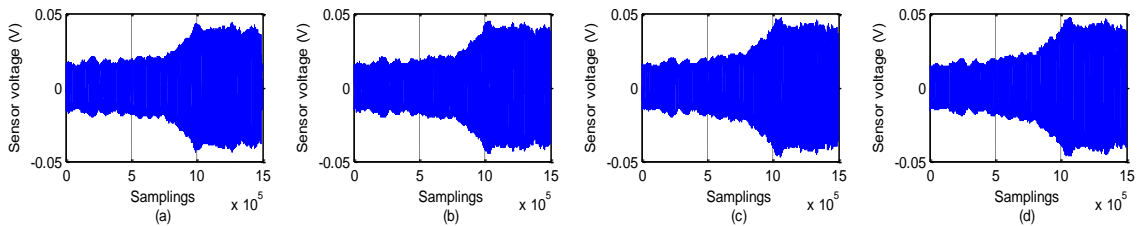


Figure 7-7 Time domain signal response of the hardened stage (a): 8 hours; (b): 10 hours (c): 12 hours (d): 16 hours

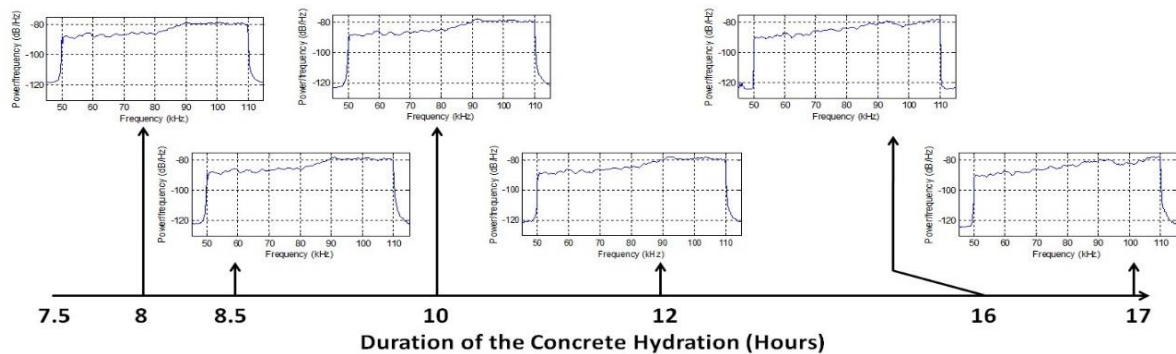


Figure 7-8 Frequency domain signal response of the transition stage

Figure 7-9 shows the frequency domain signal response during the entirety of the very early age concrete hydration process. The red curves represent the frequency domain

signal response in the liquid stage (0-1 hour). In this stage, the signals were weak and two small frequency peaks were observed. The blue curves represent the transition stage signal response (1-7.5 hours). In this stage, the signal was unstable in form (“shape”) because of the transition concrete hydration period. The green curves represent the hardened stage signal response. In this stage, the hardened concrete structure enhanced the ultrasonic wave propagation. The amplitudes of the signal approached their maximum and maintained their stability as the concrete hydration process continued.

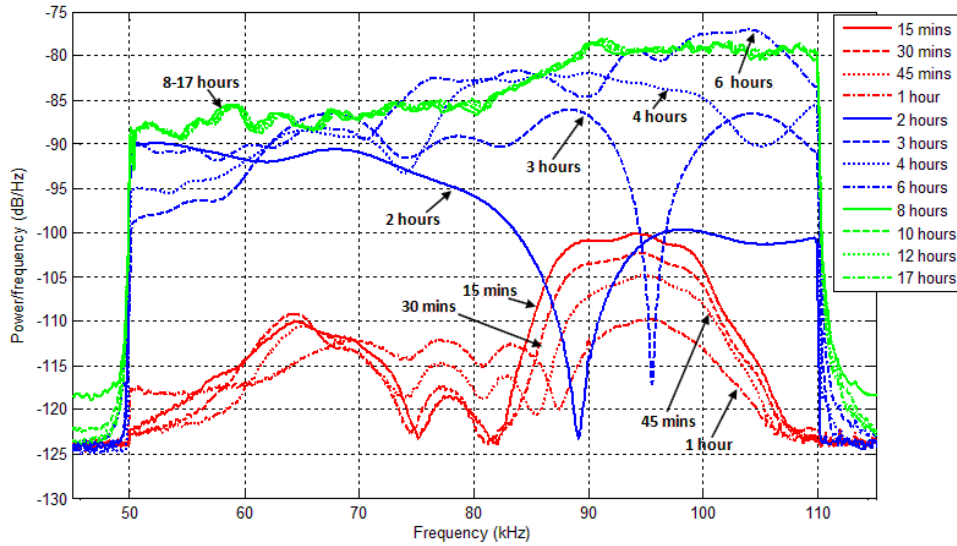


Figure 7-9 Frequency domain signal response during the concrete hydration

7.2.2 A concrete beam test using both compressive mode and shear mode smart aggregates

7.2.2.1 Smart aggregates in compression mode and shear mode

In the previous section, compressive mode smart aggregate was investigated. In this section, a comparison study was studied between two types of smart aggregates. Based on the different modes of PZT patches, two types of smart aggregates were

investigated: compression mode smart aggregate (CMSA) and shear mode smart aggregate (SMSA), as mentioned in Section 2.4.

The proposed experiment will be used to evaluate the performance of compressive wave and shear wave in the very early age concrete hydration monitoring. One pair of smart aggregates in compression mode and another pair of smart aggregates in shear mode were installed in the mold before placing concrete.

7.2.2.2 Experimental setup and procedures

Four smart aggregates were installed at pre-determined locations before casting. Two smart aggregates marked in red color are in compression mode, while the other two smart aggregates marked in yellow color are in shear mode, as shown in Figure 7-10. For each type of the smart aggregate, the embedded piezoceramic lies in the same plane pointed by the black line. The orientation of the smart aggregates is shown in Figure 7-11. Each pair of the SAs was 3" away from the end of the specimen and 1.5" height to the bottom. A photo of the concrete mold with installed smart aggregates is shown in Figure 7-12.

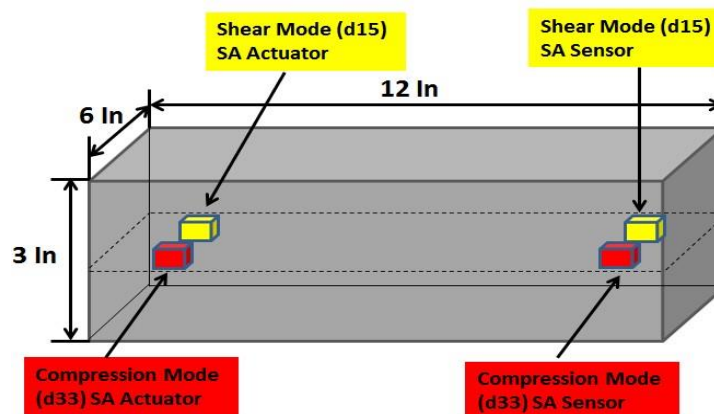


Figure 7-10 The schematic of the proposed concrete beam with embedded smart aggregates

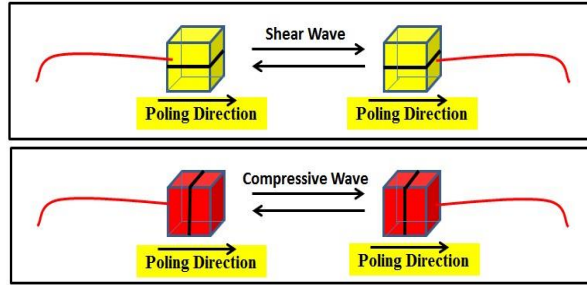


Figure 7-11 The orientation of two pairs of smart aggregates



Figure 7-12 A photo of the concrete mold with installed smart aggregates

The data acquisition started shortly after the concrete was casted. For both CMSAs and SMSAs, one of each pair was used as an actuator and the other one was used as a sensor. The excitation signal to the actuator was a repeated swept sine wave signal. The amplitude was 10V, and the period was 1s. The start and stop frequency were 100 Hz and 150 kHz, respectively. The sensors' signal was regularly recorded from the beginning of the concrete casting to 37 hours for both SMSAs and CMSAs.

7.2.2.3 *Experimental results and discussions*

7.2.2.3.1 *Result analysis of SMSA*

Figure 5 shows the power spectrum density plot of the SMSA sensor signal during the entire concrete hydration monitoring from 0 to 37 hours.

From 0 to 8 hours shown in Figure 7-13(a), the magnitude of the sensor signal dramatically increased, especially in the low frequency range. The yellow line represents

the detected signal in the first hour after casting. Since the casted concrete within the first hour was mostly in the liquid stage, the ultrasonic wave transition energy between the actuator and sensor was subject to a high attenuation level. Therefore, the magnitude of the sensor signal was very low. As the concrete hydration progressed, the concrete continuously hardened, which enhanced the energy transition rate from the actuator to the sensor. Consequently, the magnitude of the sensor signal smoothly increased as shown in green, red and blue color, respectively. Around 8 hours, the concrete was close to the hardened stage and the magnitude of the sensor signal reached the maximum. Throughout the entire frequency range from 100 Hz to 150 kHz, a 20 dB increase of the magnitude can be observed from 0 hour to 8 hours.

After 8 hours, the concrete was in the hardened stage and became solid. The magnitude of the signal remained in the high level within low frequency range since the concrete hydration was approaching to solid stage. However, the magnitude of the signal in high frequency range continuously decreased and eventually dropped 20 dB back to the initial value when the concrete was casted, as shown in Figure 7-13(b) and Figure 7-14.

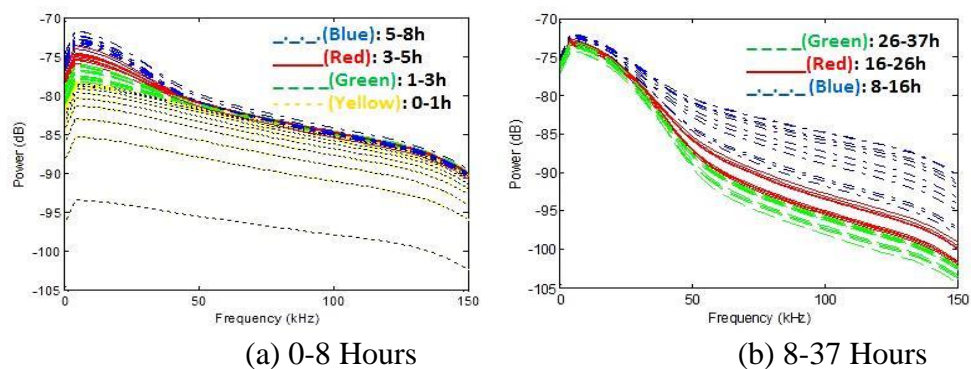


Figure 7-13 Power Spectrum Density of SMSA Sensor Signal during the entire concrete hydration process

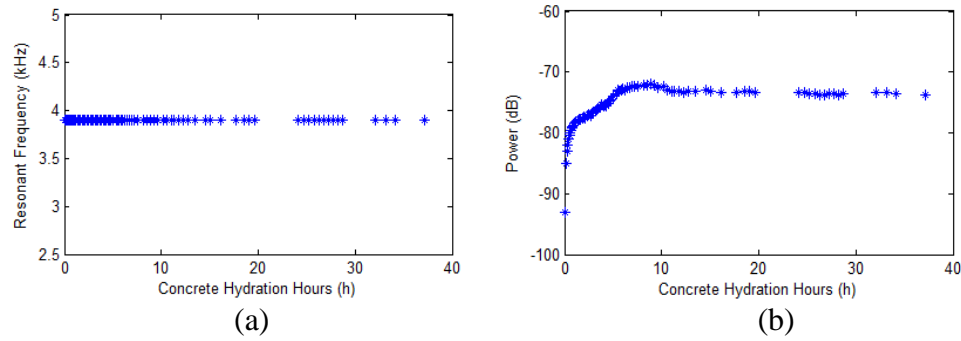


Figure 7-14 Resonance frequency (a) and the corresponding signal power (b) for SMSAs

7.2.2.3.2 Result analysis of CMSA

Figure 7-15 presents the power spectrum density results of the signal using CMSAs. From 0 to 8 hours, the magnitude of the signals were much closer to each other and maintained a low level profile, as shown in Figure 7-15(a). It can be supposed that the ultrasonic wave in compression mode had difficulty propagating through the concrete within the first 8 hours. Consequently, a magnitude “jump” can be observed at 70 kHz when the concrete hydration was approaching to 8 hours. As the concrete hydration progressing after 8 hours, the magnitude of the detect signal in high frequency range increased, while the magnitude of the signal in low frequency range kept in the same value, as shown in Figure 7-15(b) and Figure 7-16.

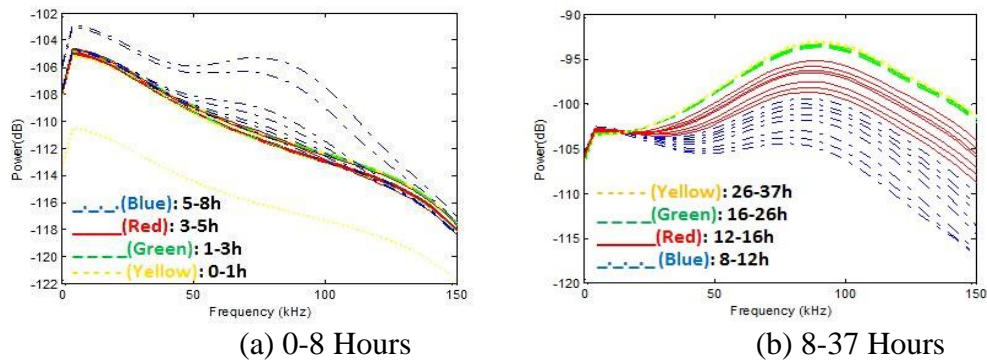


Figure 7-15 Power Spectrum Density of CMSA Sensor Signal during the entire concrete hydration process

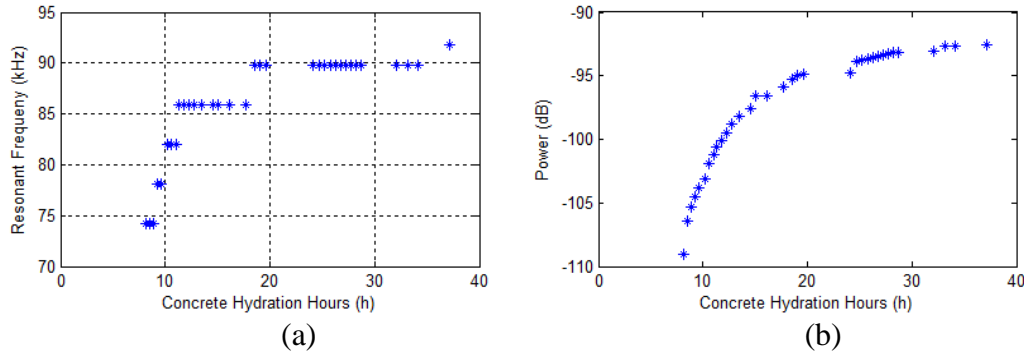


Figure 7-16 Resonance frequency (a) and the corresponding signal power (b) for CMSAs

7.2.2.3.3 Comparison results of SMSA and CMSA based detection

Although the concrete hydration monitoring using both the SMSAs and CMSAs is based on the active sensing system and ultrasonic wave propagation, several differences between these two modes can be concluded. First of all, the average magnitude of the detected signal using SMSAs is much greater than those using CMSAs. Comparison with Figure 7-13 and Figure 7-15, the magnitude range measured by SMSAs during the entire concrete hydration ranged from -100dB to -72dB which is higher than the range of -122dB to -93dB measured by CMSAs. Secondly, SMSA based concrete hydration monitoring functions earlier than the CMSA based monitoring. For the concrete specimen used in this experiment, the increasing trend of the signal magnitude measured by SMSAs represents the state of the specimen right after the concrete casting, however, the trend is shown at 8 hours after casting using CMSAs. Finally, the effective frequency range to monitor the concrete hydration by SMSA is in the low frequency range and the related frequency range to monitor the concrete hydration by CMSA is in the high frequency range. The summary of comparison results is shown in Table 7-3.

Table 7-3 Comparison results between SMSA and CMSA

	Detected Signal Strength	Effective Monitoring Time	Related Frequency Range
SMSA	Strong	From 0 h	Low (<10kHz)
CMSA	Not Strong	From 8 h	High (>50kHz)

7.2.2.3.4 Result analysis using constant frequency excitation method

During the concrete hydration process, the constant frequency sine wave was also applied to monitor the status of the concrete. In this test, two constant frequency sine waves were chosen (90 kHz and 100 kHz). Comparing with the swept sine wave excitation, the constant frequency sine wave excitation induced a sensor signal, which at each time showed the same amplitude and frequency response. Therefore, the author utilized the amplitude value of the sensor signal to record data at each time. Figure 7-17 shows the signal response of the sensor SA excited by two single constant-frequency sine waves (90 kHz and 100 kHz) during the whole concrete hydration process. The results from the constant frequency exaction approach also verified the three stages' classification of the concrete hydration discussed before. In the first liquid stage, the amplitudes of the signal were very low. In the second transition stage, the amplitudes of the signal were chaotically increasing. Finally, in the third hardened stage, the amplitudes of the signal were approaching to the maximum value and maintained stability.

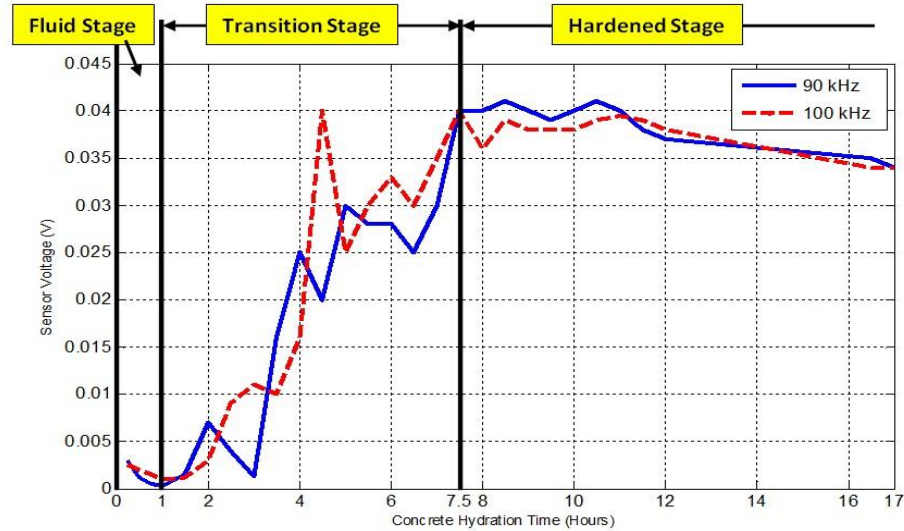


Figure 7-17 The amplitude of received signal under the constant frequency sine wave excitation (90 kHz and 100 kHz)

7.2.2.4 Discussions

In this section, the active sensing approach is applied to the very early age concrete hydration characterization monitoring. Through analyzing the amplitude and the frequency response of the received, three hydration stages were clearly verified. In the first 1 hour (liquid stage), the concrete was in the fluid condition and the structure inside the concrete changed steadily. Meanwhile, the signal responses between smart aggregates were weak. From 1 hour to 7.5 hours (transition stage), due to the concrete phase transition, the properties of concrete structure were constantly changing. Thus, the signal responses from both time domain and frequency domain were classified as chaotic. From 7.5 hours (hardened stage) and onwards, the hydration turned to hardened stage and the reaction became smooth in which the amplitudes of the signal were strong and stable.

7.3 Summary

In this chapter, the proposed active sensing approach using smart aggregates was investigated to very early age (the first 20 hours) concrete hydration monitoring. A pair of smart aggregates was appropriately installed closely to each other before casting. According to the amplitude level and frequency domain analysis, three states during the concrete hydration were found: (1) the liquid state, (2) the transition state, and (3) the hardened state. In addition, a comparison study was done by using a pair of CMSAs and SMSAs for a very early age concrete hydration monitoring, simultaneously. It is found that the average of received signal from SMSAs is stronger than that from CMSAs. In addition, the effective concrete hydration monitoring for SMSAs can start from the beginning of the hydration, which is 8 hours' earlier than CMSAs based concrete hydration monitoring.

The influence of concrete hydration behavior from different concrete mix was not investigated in the research. However, concrete hydration behavior will highly depend on the composition of the concrete mix. Fly ash, slag and silica fume, as supplementary cementations materials, are the most commonly used mineral admixtures in contemporary concrete, In common, silica fume speeds up the hydration process while fly ash and slag retard it. In the future research, the effect of mineral admixture on the hydration process of concretes can be revealed.

8 Soil freeze-thaw monitoring

8.1 Introduction

It is well known that the frozen soil has impacts on infrastructure, agriculture, and the environment. During the freeze-thaw cycle, the soil is subject to expansion and contraction which can result in crop failure, pavement cracks, and road deformation, for example. Seasonal freezing has also been found to change the dynamic properties of bridges and buildings and hence affect their seismic characteristics [142] [143] [144]. Robinson *et al.*, and Zhang *et al.*, presented seasonal freezing and thawing conditions of land in the northern hemisphere [145] [146].

Microwave detection is an effective technique to monitor the soil freeze-thaw state transition. Elachi *et al.*, studied the variation of the dielectric properties of soils during the freeze-thaw cycle [147]. The NASA Scatterometer (NSCAT) was also applied by many researchers to monitor the soil freeze-thaw transitions [148] [149]. Naeimi *et al.*, developed a threshold analysis method using C-band scatterometer data to monitor the freeze-thaw conditions in real-time [150]. Zwieback *et al.*, combined Ku- and C-band scatterometer data and presented a sensor fusion algorithm to retrieve the freeze-thaw data [151].

In the recent decades, piezoceramic materials have been successfully utilized for infrastructure monitoring. Li *et al.*, detected the water-ice transition based on the resonance frequency of the piezoceramic material [152]. An impedance-based approach based on the electromechanical property of the piezoceramic material was also utilized to monitor the structural health [38] [153]. Gu *et al.*, demonstrated the effective use of

Smart Aggregate (SA) based active sensing approaches for monitoring the structural health of concrete columns subjected to seismic excitations [154].

This chapter developed a new application of active sensing approach to monitor the soil freeze-thaw process using smart aggregates. Two soil specimen with different sizes were investigated. Since the characterization of stress wave propagation is highly sensitive to the mechanical properties of soil during the freezing and thawing process. The received stress wave can be an effective indicator to determine the soil status. With the developed signal process technique and root-mean-square deviation technique, the degree of soil freezing or thawing was characterized by the proposed wavelet packet-based soil frozen index.

8.2 Detection principles

Active sensing approach complemented with smart aggregates is developed for real-time soil freeze-thaw monitoring. In the basic active sensing system as mentioned in section 2.4.2.2, one smart aggregate (SA1) is used as an actuator to generate the desired stress wave which will propagate through the soil. At the meanwhile, another smart aggregate (SA2) is used as a sensor to detect the wave response, as shown in Figure 8-1. As the soil goes through a freeze-thaw cycle, its mechanical properties changes considerably depending on the amount of ice matrix formed; the change in mechanical properties of soil will impact the stress wave propagation between the smart aggregate's changes and hence the signal received at the sensor. Potentially the signal received at the sensor can be correlated with the mechanical properties of the soil, providing a continuous assessment of the mechanical property variation during a freeze-thaw cycle.

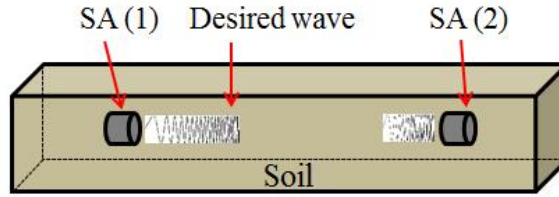


Figure 8-1 Schematic diagram of smart aggregate based active sensing approach

If multiple smart aggregates are embedded in the soil, the actuators and sensors can be altered. Therefore an active sensing system with multiple smart aggregates has a potential to monitor the global characteristics of the soil freeze-thaw condition. The diagram of an active sensing system example with multiple smart aggregates is shown in Figure 8-2.

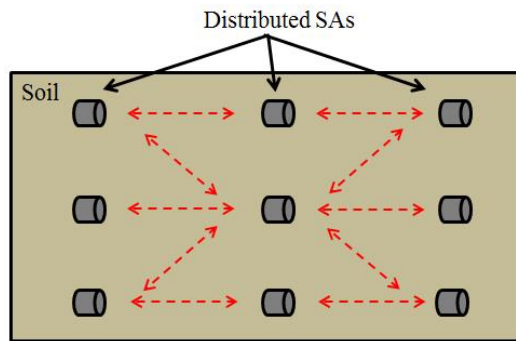


Figure 8-2 A proposed active sensing system with multiple smart aggregates for soil freeze-thaw monitoring

8.3 A small scale soil specimen test

8.3.1 Experimental setup and procedures

8.3.1.1 Test specimen description

Figure 8-3 shows a view of the prepared test soil specimen complemented with two smart aggregates and one thermocouple sensor. Figure 8-4 depicts the test setup. The length and diameter of the specimen is 8" and 2.5", respectively. Two smart aggregates (SA1 and SA2) and a thermocouple sensor were embedded into the soil specimen at pre-

determined locations (refer to Figure 8-4). The thermocouple was embedded in the center of the specimen and each smart aggregate was installed 1.5" away from the end of the specimen. The electrical properties of the smart aggregates are listed in Table 8-1. A loose sandy soil specimen with a moisture content of 8% was housed in a PVC pipe. Figure 8-5 illustrates the particle size distribution curve for the soil specimen. According to the Unified Soil Classification System, the soil specimen is classified as poorly graded sand (SP).



Figure 8-3 A photo of the test soil specimen with transducers

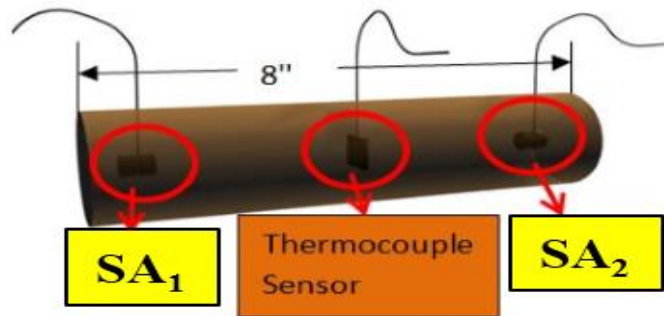


Figure 8-4 Schematic of the test soil specimen and sensor location

Table 8-1 Properties of the smart aggregates

	Sensitivity (Pc/N)	Capacitance (nF)
SA 1	252.28	6.68
SA 2	262.9	7.72

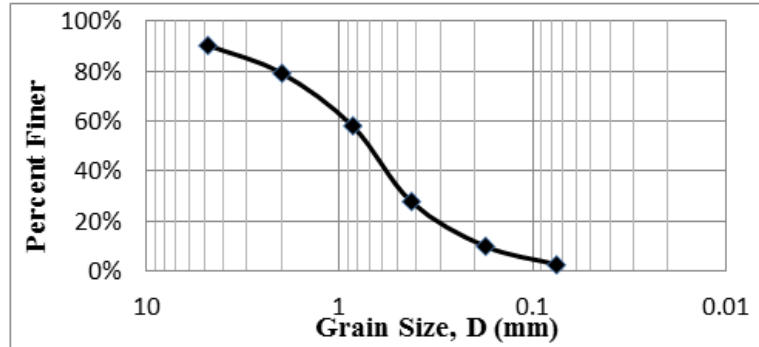


Figure 8-5 Particle size distribution of the soil specimen

8.3.1.2 Test procedures

An entire freezing and thawing process was simulated in a temperature-controllable freezer. The sandy soil specimen was prepared and kept in the laboratory at a room temperature of 2°C. In the freezing process, the specimen was moved into the temperature-controllable freezer for artificial freezing. Upon complete freezing, the temperature of the specimen started to drop below 0°C and reached -20°C before this experiment shifted to thawing process. In the thawing process, the specimen was taken out from the freezer and kept in the laboratory at a room temperature of 25°C. Under the room temperature, the specimen warmed up gradually and started to thaw. Upon complete thawing, the temperature of the specimen started to rise and reached 10°C at the end of this experiment. During the freeze-thaw cycle, in addition to the thermocouple measurements, the active sensing system based on two SAs (SA1 and SA2) was used to monitor the entire process.

8.3.1.3 Experimental setup

In this experiment, SA1 was used as the actuator to emit a swept sine wave and SA2 was used as the sensor to receive the stress wave emitted from SA1. The swept sine

wave parameters are shown in Table 8-2. The frequency of the swept sine wave increases linearly from 0.1 kHz to 10 kHz in a 3-sec cycle. During the soil freeze-thaw cycle, a thermocouple sensor was utilized to record the temperature of the specimen and SA2 was used to record transmitted stress wave through the soil specimen. The sampling rate is 50 kHz. During the test, one measurement was recorded every 5 minutes and each measurement lasted for 9 second (three cycles of the guided swept sine wave).

Table 8-2 Parameters of the swept sine wave

Start Frequency	0.1 kHz
Stop Frequency	10 kHz
Sweep period	3 sec
Voltage Amplitude	10 V

8.3.2 Experimental results and discussions

8.3.2.1 Temperature monitoring

A thermocouple sensor was used to measure the temperature of the specimen during the freeze–thaw cycle. As shown in Figure 8-6, the initial temperature of the specimen was 25.14°C and the coldest temperature of the specimen was -23.11°C. The first 4.1 hours was the freezing process and the thawing process was from 4.1 hours to 6.5 hours. At the beginning of the freezing process, the temperature of the soil dropped smoothly. When the soil started to freeze, the temperature of the soil stayed around the freezing point, i.e. 0°C, for about 1 hour before it started to drop again. The thawing process is opposite to the freezing process. Since the freezing was achieved by the freezer and the thawing process occurred at room temperature in the laboratory, the thawing process appears to be faster than the freezing process.

8.3.2.2 Time domain analysis

When the soil was unfrozen, no meaningful data was observed. Loose soil has relatively low stiffness and almost no stress wave energy in the higher frequency range can transmit through the soil, thus the signal recorded at the sensor appears as white noise.

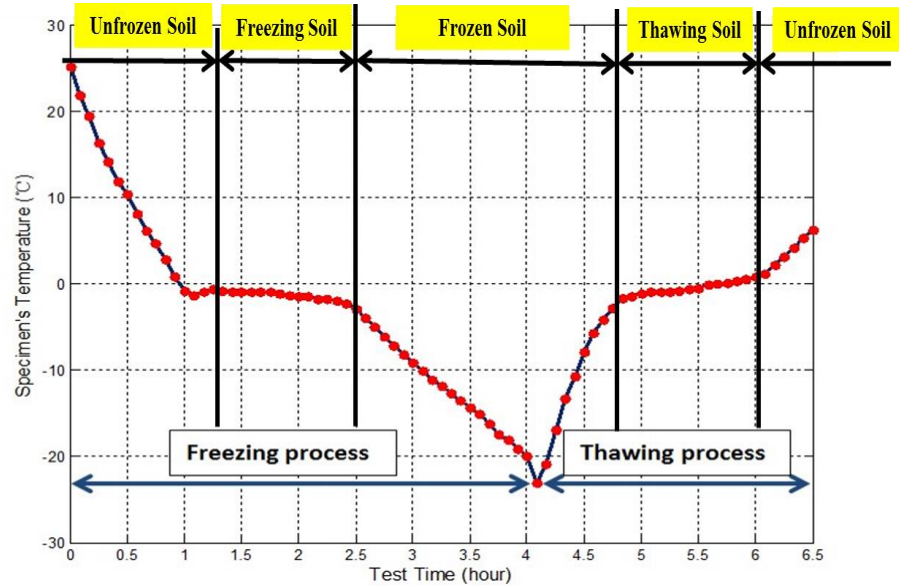


Figure 8-6 Specimen temperature monitoring during the freezing-thawing cycle

When the temperature of the specimen in the freezer dropped below 0°C, the pore water inside the moist soil specimen began to freeze. Freezing of the pore water kept the specimen's temperature around the freezing point. When most of the pore water froze, the soil temperature started to drop again. As pore water freezes, ice bonds form between soil particles, hence increasing the stiffness of the soil gradually but substantially. A continuously stiffened soil is capable of transmitting more and more stress wave energy from the actuator to the sensor, and the SA sensor began to capture the signals with increasing magnitude. Figure 8-7 shows the signals from the SA sensor in one sweep sine

wave cycle from the initial freezing stage to the stage when the specimen reached the lowest temperature. Note that that time is directly related to frequency since the frequency of the emitted sine wave linearly increases from 0.1 kHz to 10 kHz. Two obvious peaks can be observed from this plot. The left peak at a lower frequency was named the 1st resonant frequency peak (RFP) and the right peak at a high frequency was named the 2nd RFP. It is seen from Figure 8 that both amplitude and frequency of the RFPs increased significantly.

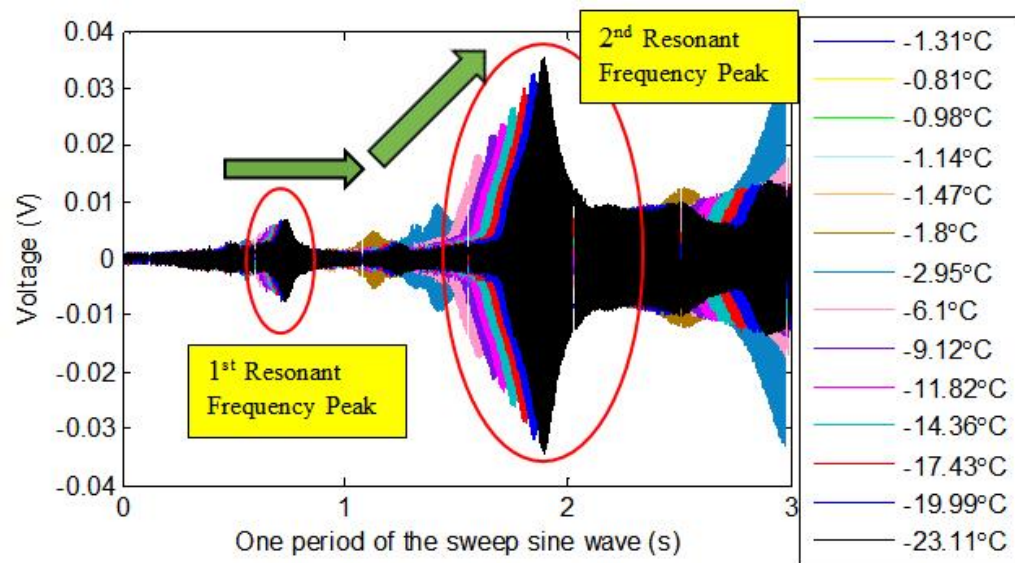


Figure 8-7 Signal recorded by the SA sensor during the freezing process

8.3.2.3 Frequency domain analysis

Figure 8-8 shows the Power Spectrum Density (PSD) results of the collected signals at different soil temperature in the freeze-thaw cycle. In the freezing process, the power of the signal remains very weak until the soil temperature reaches the freezing point. As shown in Figure 8-8, the plot corresponding to -0.81°C is the PSD plot of the unfrozen soil at the initial stage of freezing and the plot corresponding to -23.11°C is the

last in the freezing process. When the pore water freezes to form ice bonds in the soil, two peaks with low energy appear in the plot corresponding to -0.98°C . As the soil freezing process continues both the amplitudes of the two peaks and the frequencies of the two peaks increase. The increase in energy as the temperature drops could be attributed to the stiffening of the soil and the two peaks correspond to the 1st and 2nd RFP observed in Figure 8-7. The RFP will be analyzed in the following section.

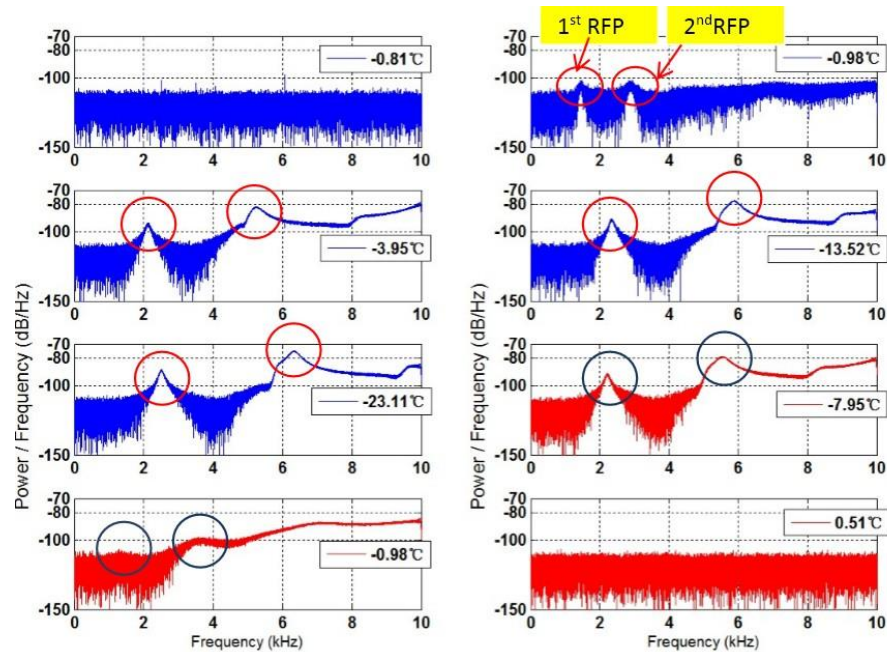


Figure 8-8 Power Spectrum Density at different soil temperature during the freeze-thaw cycle

In the soil thawing process, the temperature of the thawing process increases from -23.11°C to 6.51°C . Three PSD plots of the signal recorded by the sensor during the thawing process are shown in Figure 8-8. The two peaks shift back to lower frequency range and the amplitudes decrease. At the soil temperature of 0.51°C , the two peaks disappear entirely and no meaningful signal can be collected. Table 8-3 and Table 8-4 list the change of frequency and amplitude of the first RFP and the second RFP, respectively.

Table 8-3 Frequency and amplitude of the 1st RFP at various soil temperatures

Soil temperature (°C)	-0.98	-3.95	-13.52	-23.11	-7.95	-0.98
Frequency (kHz)	1.44	2.08	2.35	2.51	2.21	1.36
Amplitude (dB/Hz)	-101.7	-94.5	-90.8	-88.9	-92.2	-106.9

Table 8-4 Frequency and amplitude of the 2nd RFP at various soil temperatures

Soil temperature (°C)	-0.98	-3.95	-13.52	-23.11	-7.95	-0.98
Frequency (kHz)	2.90	5.23	5.90	6.33	5.55	3.57
Amplitude (dB/Hz)	-102.3	-82.1	-77.7	-75.0	-79.6	-98.0

8.3.2.4 Resonance frequency analysis

In the soil specimen, the SA actuator and sensors are embedded into the soil. As observed in Figure 8-7 and Figure 8-8, resonance between the SAs and the soil occurred at various frequencies. The resonant frequency of the SAs embedded in the soil is affected by the soil density and stiffness, and the mechanical and geometry properties of the SAs. Lee *et al.*, provided a first-order estimate of the resonant frequency of a bender element (a SA in this case) embedded in soil and this estimate can be used to estimate the resonant frequency (f_r) of a SA embedded in soil [155]. The resonant frequency can be expressed as

$$f_r = \frac{1}{2\pi} \left[\frac{1.875^4 \frac{E_{SA} I}{(\alpha L_{SA})^3} + \eta V_P^2 \rho_s L_{SA}}{\rho_{SA} \alpha \pi r_{SA}^2 L_{SA} + (\rho_s \pi r_{SA}^2 L_{SA}) \beta} \right]^{1/2}, \quad (8-1)$$

where E_{SA} and ρ_{SA} are the Young's modulus and mass density of the SA. Since the PZT material is sandwiched between two marble plates, the Young's modulus and mass density of marble is used in this analysis. E_{SA} and ρ_{SA} were determined to be 5.6×10^{10} N/m² and 2600 kg/m³ respectively. I is the moment of inertia of the SA; $I = \pi r_{SA}^4/4$, $r_{SA} = 1.27$ cm is the radius of the SA. $L_{SA} = 2.54$ cm is the length of the SA; α is effective length factor which is affected by the anchor efficiency ($\alpha = 1$ for a perfectly rigid

anchor and $\alpha > 1$ for a soft anchor); α was assumed to be 4 to account for the direct embedment (very soft anchor) of the SA in the soil; η is mean displacement influence factor at the soil element interface; $\eta \approx 2$; V_P is the pressure wave velocity of the soil specimen; $\nu = 0.3$ and $\rho_s = 1,500 \text{ kg/m}^3$ are Poisson's ratio and mass density of the soil specimen, respectively; β is an experimentally determined value. The shear wave velocity V_S in the soil specimen can also be obtained as

$$\frac{V_P}{V_S} = \sqrt{\frac{2(1-\nu)}{1-2\nu}}. \quad (8-2)$$

Firstly, parameter β can be evaluated from data obtained at the soil initial freezing condition. When the temperature was -0.98°C , the first resonance frequency (f_r) was observed as 1.6 kHz. Based on the soil mass density, V_S of the loose sand with little confinement pressure was estimated to be around 120 m/s and V_P was estimated to be about 224 m/s at the initial freezing condition. β was determined to be 10.8 by using equation 8-1.

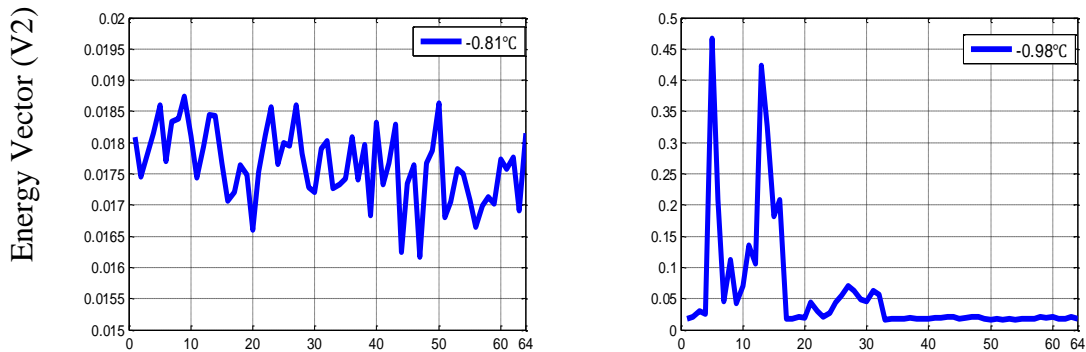
Now the pressure wave velocity V_P and shear wave velocity V_S in the soil specimen at different temperatures can be evaluated based on the resonant frequencies listed in Table 8-3. Table 8-5 lists the pressure wave and shear wave velocity inferred from the resonant frequency data. One can see that as the soil specimen transitions from the water freezing point to -23°C , its pressure wave velocity increases from 224 m/s to 914 m/s, and its shear wave velocity increases from 120 m/s to 489 m/s. The pressure wave velocity and shear wave velocity appears to be reasonable for the ice-poor frozen soils used in this experiment. Should the initial water content be higher, the increase in pressure wave or shear wave velocity would be larger.

Table 8-5 Pressure and shear wave velocity of the soil specimen at various temperatures

Temperature (°C)	First resonance frequency (kHz)	P-wave velocity (m/s)	S-wave velocity (m/s)
-0.98	1.6	224	120
-3.95	2.0	598	320
-13.52	2.3	795	425
-23.11	2.5	914	489

8.3.2.5 Energy vector analysis

The energy vectors of the SA signal are shown in Figure 8-9. Two obvious energy peaks can also be observed in this plot. Both the 1st RFP and the 2nd RFP change in a trend similar to that of the PSD result. No obvious peak can be observed before the ice bonds form or after all the ice bonds thaw. During the entire freeze-thaw process, the energy of the received signal increases as the soil freezes and decreases as the soil thaws. The maximum received energy of the two resonant frequency peaks are 140 and 170, as shown in the energy vector vs. temperature plot. The variation of frequency and amplitude of the two resonant frequency peaks with soil temperature are shown in Figure 8-10 and Figure 8-11, respectively.



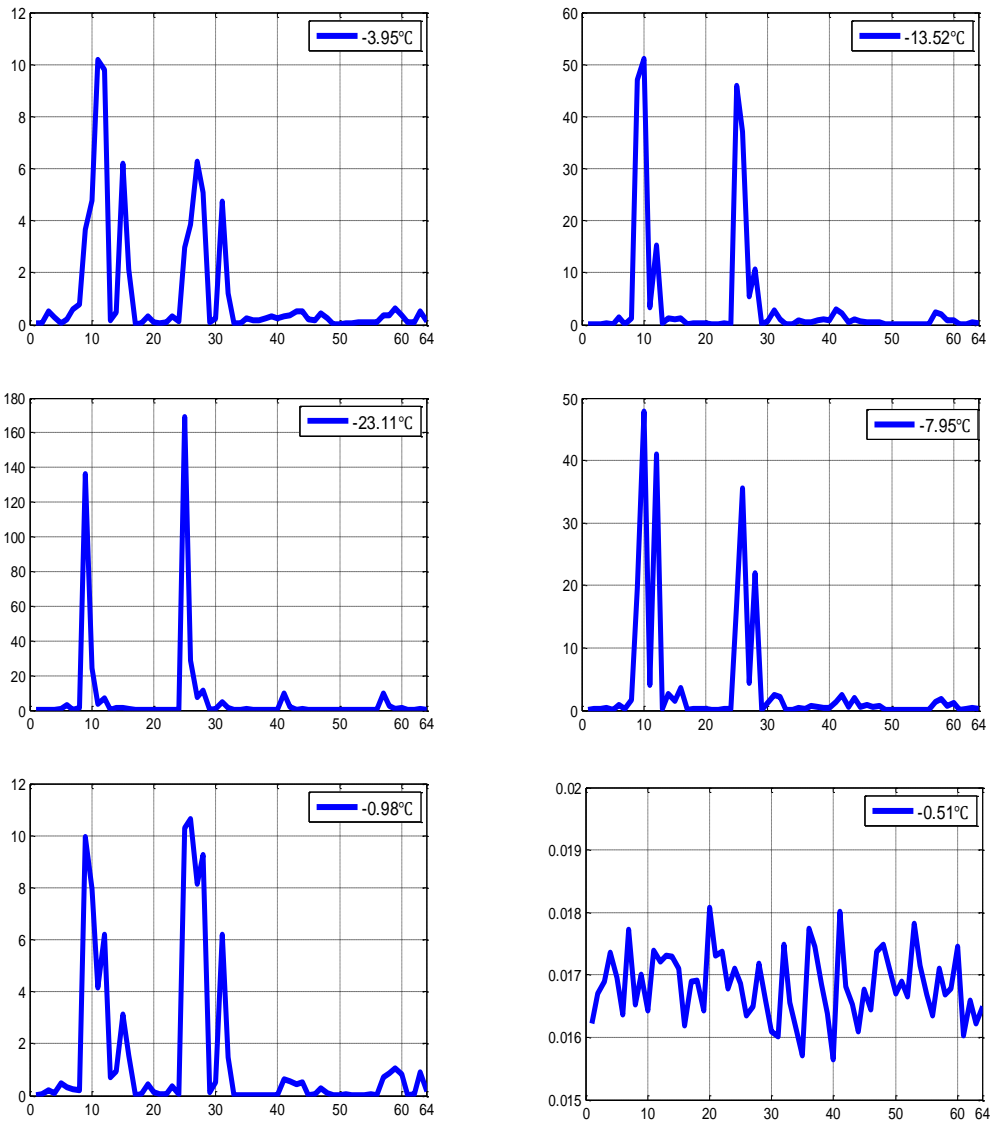


Figure 8-9 Energy vector plot in different freezing and thawing degrees

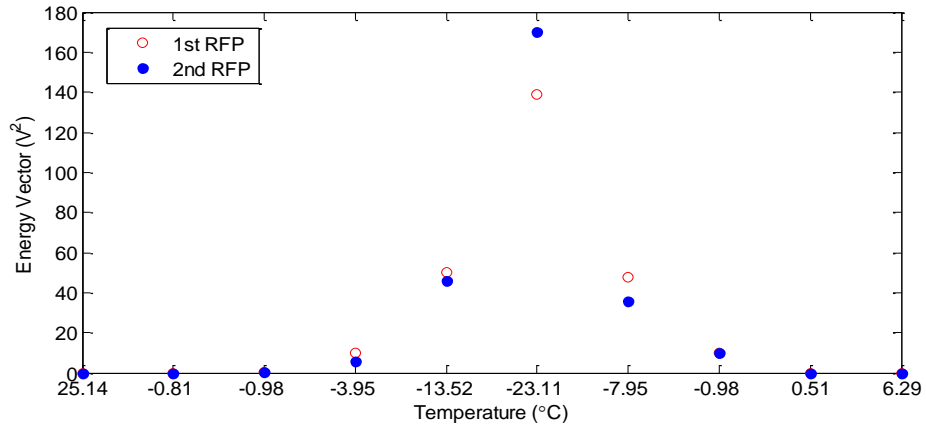


Figure 8-10 Calculated signal energy of two resonant frequency peaks in different temperature

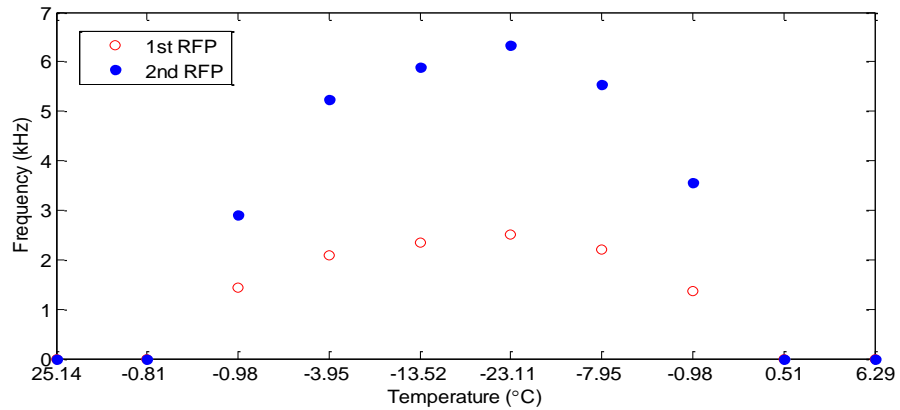


Figure 8-11 The values of resonance frequencies of two resonant frequency peaks in different temperature

8.3.2.6 Wavelet packet analysis

Using the wavelet packet-based energy vector calculation, a soil freeze-thaw status indicator can be established, as shown in Figure 8-12. The height of the histogram reflects the freeze status of the soil, indicating how much pore water transforms to ice bonds or the overall stiffness of the partially frozen or frozen soil. The maximum value in the indicator occurs when the specimen is at the lowest temperature, or highest stiffness. In the freeze-thaw cycle, this indicator can have different values at the same soil

temperature, depending on if it is at the freezing process or the thawing process. Possible reason is hysteresis in the water phase transition. Take an example, when the temperature of the soil specimen increased from -1°C to 1°C , the water cannot complete the full transition from ice state to water state. The actual soil frozen condition cannot be accurately determined by the temperature. However, the wave propagation based soil freeze-thaw monitoring is capable of providing more accurate and reliable results than the temperature measurement.

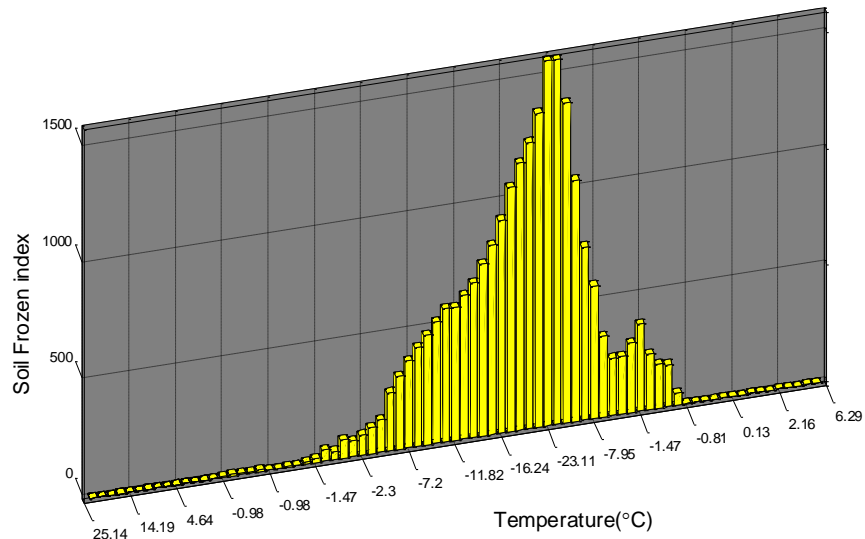


Figure 8-12 Wavelet packet-based soil frozen index

8.3.2.7 Discussion

The results presented in this section show that, while the soil transitions from unfrozen to frozen status, or from frozen to thawed status, soil temperature varies very little, giving little to no information as how much pore water has transformed into ice. Instead, the energy transmitted through the soil and the resonant frequencies found in the test results reveal much more information during this phase transformation process than

the soil temperature. These results demonstrate that the active sensing technique with smart aggregates could be developed further into a technology for characterizing partially frozen soil or very warm permafrost that poses many engineering challenges. In addition, the resonant frequencies revealed in the test results could also be used to evaluate the shear wave velocity or stiffness of the soil.

8.4 A large scale soil specimen test

8.4.1 Experimental setup and procedures

8.4.1.1 Experimental setup

The experimental setup is shown in Figure 8-13. Two SAs were installed in the center of an empty plastic box (23''×16.25''×12.38'') by bonding to two wooden beams, as shown in Figure 8-13 (a). Saturated sandy soil was then poured into the plastic box, as shown in Figure 8-13 (b) form the test specimen. The distance between the two SAs is 3''. A thermocouple sensor was embedded into the center of the specimen. The data acquisition system used in this study was an NI-USB 6353, as shown in Figure 8-13 (c). In order to enhance the response of the signal received from the sensor, a power amplifier (50x Gain) was used to drive the actuating SA.

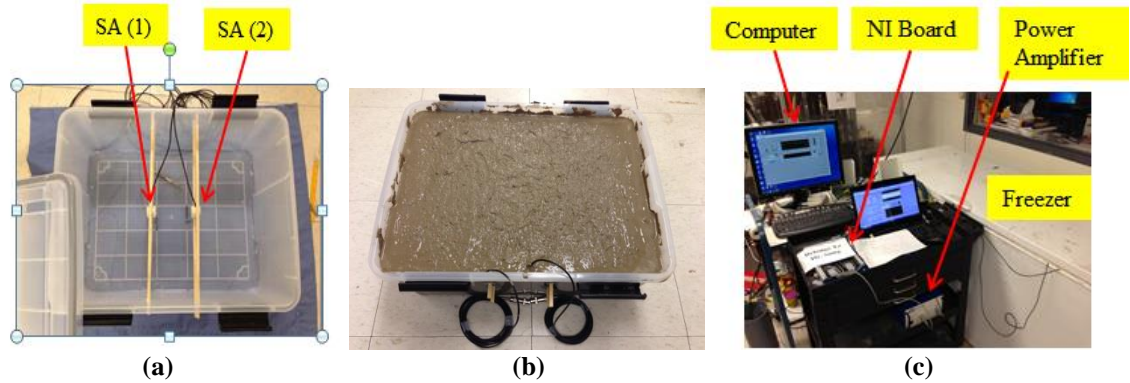


Figure 8-13 Experimental setup

8.4.1.2 Test Procedures

The entire freezing process was simulated in a temperature-controllable freezer. The initial temperature of the soil specimen was the room temperature of 25°C. In the freezing process, the specimen was moved into the temperature-controllable freezer for artificial freezing. The temperature at the end of the freezing process was -17°C. Then the experiment was shifted to the thawing process. In the thawing process, the specimen was taken out from the freezer and kept in the laboratory at a room temperature of 25°C. Under the room temperature, the specimen warmed up gradually and started to thaw. Since the sensor would not detect any meaningful signal when the soil was completely thawed, the experiment was ended at the temperature around 5°C.

The parameters of the swept sine wave signal are listed in Table 2-1. The sampling rate was 1 Ms/s. During the test, one measurement was recorded every 15 minutes and each measurement lasted for 1 second (one period of the guided swept sine wave). With the amplifier, the driving voltage to the actuating smart aggregate was 150V.

Table 8-6 Parameters of the excitation sine wave

Start Frequency	100Hz
Stop Frequency	150kHz
Sweep period	1 s
Voltage Amplitude	150V

8.4.2 Experimental results and discussions

8.4.2.1 Time domain analysis

When the soil was unfrozen, the soil has relatively low stiffness and high damping. The stress wave energy can hardly propagate from the smart aggregate actuator to the smart aggregate sensor. The detected signal was similar to white noise, as shown in Figure 8-14.

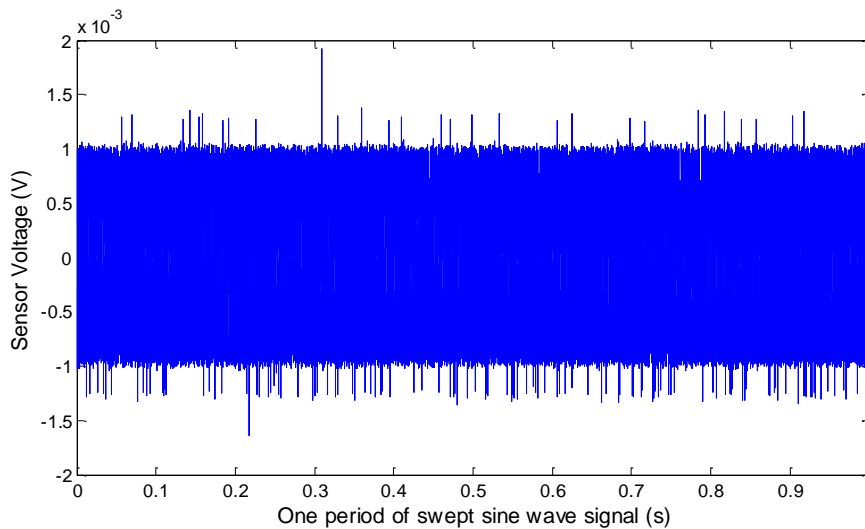


Figure 8-14 Recorded signal of the SA sensor for the unfrozen soil

When the temperature of the specimen in the freezer dropped below 0°C, the pore water inside the saturated soil began to freeze. The stiffness of the saturated soil increased steadily when more and more ice bondages formed in the soil. A continuously stiffened soil is capable of transmitting more and more stress wave energy from the

actuator to the sensor, and the SA sensor began to capture the signals with increasing magnitude. Several detected sensor signal in soil freezing process is presented at the temperature of -1°C , -5°C , -10°C , -17°C , as shown in Figure 8-15. As the temperature of the soil dropping down, the magnitude of the sensor signal continuous increases.

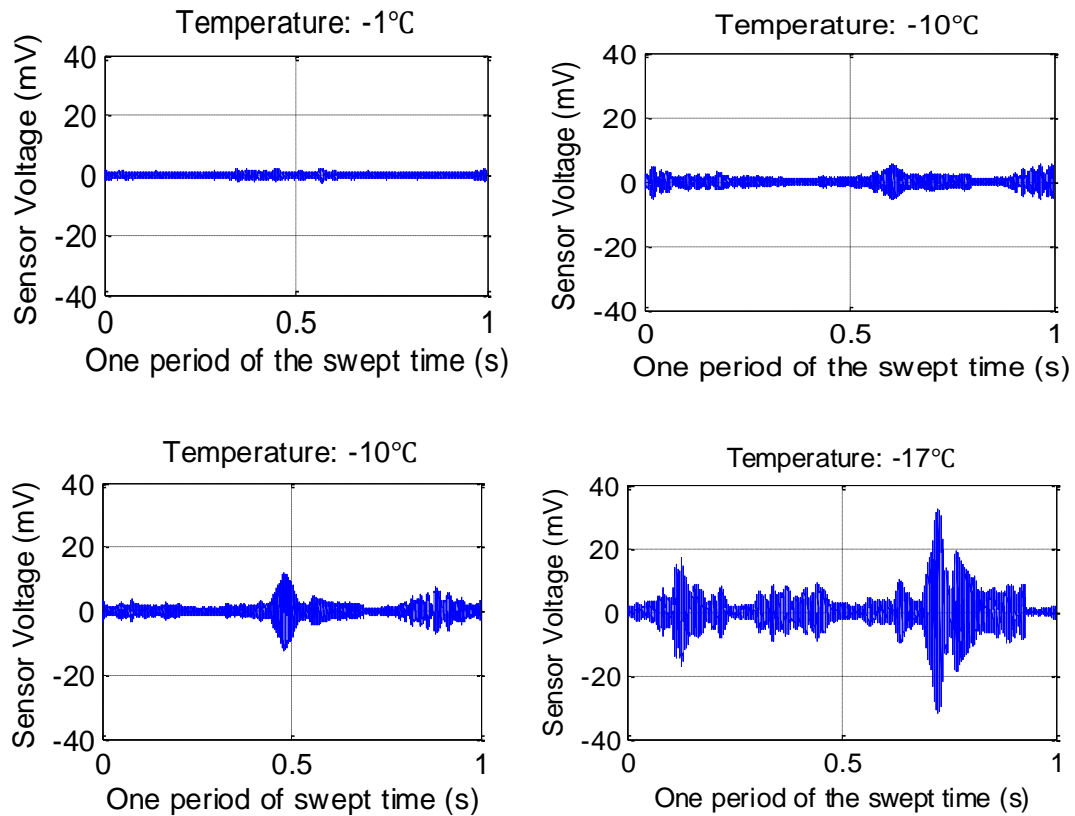


Figure 8-15 sensor signal in one sweep period at different temperatures

8.4.2.2 Wavelet packet-based soil freeze-thaw status indicator

Applying the wavelet packet-based analysis, a soil freeze-thaw indicator is created, as shown in Figure 8-16. The height of the histogram reflects the freeze-thaw status of the soil, indicating the overall stiffness of the partially frozen or fully frozen soil. The maximum value in the indicator occurs when the specimen is at the lowest temperature,

or highest stiffness. In this experiment, the lowest temperature of the soil occurred at -17°C matching with the maximum value of the indicator around 800. During the thawing process, the value of the indicator continuously drops to 0.

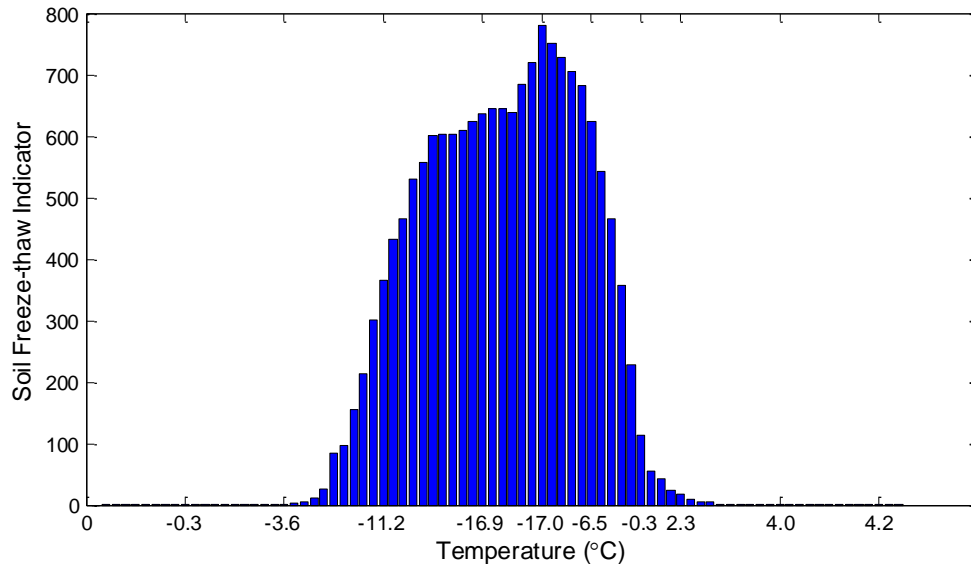


Figure 8-16 Wavelet packet based soil freeze-thaw status indicator

Figure 8-17 shows the hysteresis loop of soil freeze-thaw indicator vs. soil temperature. It may be observed in the figure that the soil freeze-thaw indicator presents different values even at the same soil temperature. A hysteretic phenomenon can be seen during the cycle. During the freezing process (right to left on blue curve), more liquid water exists in the sample than ice, and a relative lower value of the indicator is observed; however during the thawing process (left to right on red curve), more ice exists in the sample than liquid water, and a relative higher value of the indicator is observed. Thus the hysteresis may be observed due to a phase transition delay between liquid water phase and the solid ice phase.

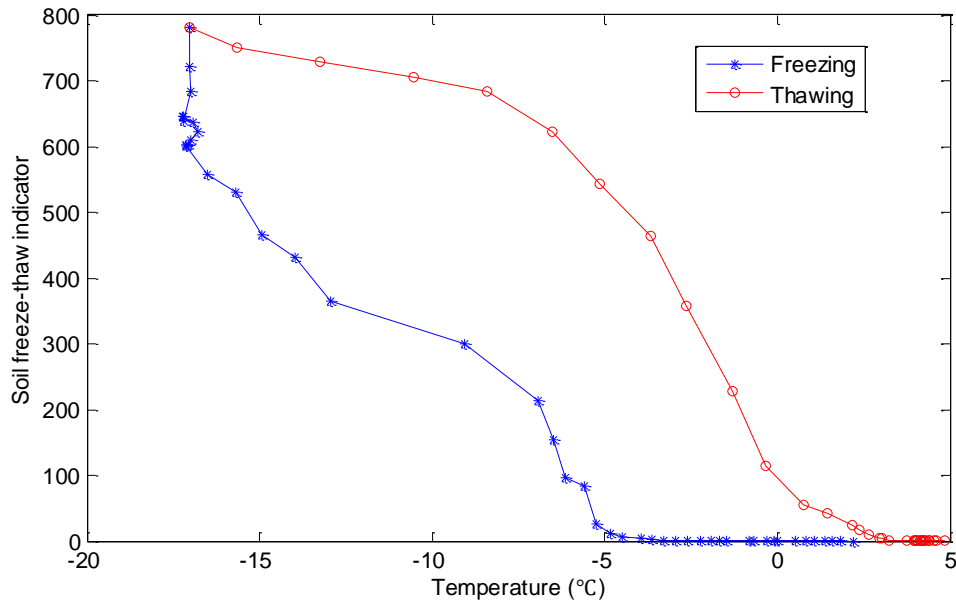


Figure 8-17 The hysteresis loop of freeze-thaw status indicator vs. temperature

8.5 Summary

In this chapter, the innovative smart aggregate based active sensing approach and the wavelet packet analysis were developed to quantitatively monitor the soil freezing and thawing process. When the soil is at unfrozen status, little stress wave energy is transmitted through the soil due to its low stiffness and high damping; the received signal is very weak. In the stage when pore water begins to transform into ice bonds, the soil skeleton begins to harden, hence the soil overall stiffness, and the stress wave energy begins to propagate through the specimen. The stress wave energy vector and the resonant frequencies revealed in the PSD result gradually changes as the soil freezes and thaws. Potentially the active sensing approach with smart aggregates could be developed further into a technology for characterizing partially frozen soil or very warm permafrost that poses many engineering challenges with future studies.

9 General Conclusions and Future Works

In this dissertation, the modeling and innovative applications of structural health monitoring using piezoceramic based transducers were investigated. Smart aggregates, with exceptional survivability comparing to the naked PZT patch, have shown their abilities to be used as embedded transducers in an active sensing system. Developed active sensing approach using smart aggregates was deeply explored to different applications of structural health monitoring. Associated with appropriate signal processing analysis, structural damage can be quantitatively characterized by a wavelet packet-based structural damage index.

This dissertation proposed theoretical model of the smart aggregate, as shown in Chapter 3. Constitutive equations and related basic equations of the smart aggregate was established. Based on the established equations, the dynamic solutions of the smart aggregate were derived. The natural frequencies were computed under the numerical simulations. Accurate values of resonance frequencies will greatly assist the implementation of piezoceramic based smart aggregates for structural health monitoring. Experimental verifications were conducted and the experimental results are in good agreement with the theoretical ones.

In chapter 4, an active sensing approach using piezoceramic based transducers was developed and experimentally studied. A crack detection of a pipeline deployed with distributed piezoceramic based transducers was first investigated. Since the crack functions as a stress relief in the wave propagation path, the signal response of the sensors report a decreasing trend with the increasing depth of the crack. A wavelet

packet-based structural damage index can successfully detect the crack development of the pipeline. Since the damage index values of the sensors are highly dependent upon sensor locations, the proposed crack severity index presents great potential to locate cracks with distributed sensors. The crack open-close detection was also investigated in a concrete column. Under the pseudo-dynamic load, the crack is subject to opening and closing which was monitored by embedded smart aggregates based on the active sensing approach. The wavelet packet-based structural damage index presents appreciable values to determine if the crack is opening or closing.

This dissertation developed an active sensing approach using smart aggregates to detect the bond slip initiation and development, as shown in Chapter 5. A wavelet packet-based structural damage index is perfectly capable of detecting the bond slip initiation and providing reliable values to monitor the further development of the bond slip severity. This investigation offers an early detection to detect the bond slip of structures.

This dissertation developed a smart aggregate based active sensing approach to detect concrete cracks and the further water presence in the cracks, as shown in Chapter 6. A concrete beam was experimentally investigated. The received signal in time domain clearly identifies three conditions, health state, crack condition, and the water presence in the crack, of the concrete beam. In addition, a wavelet packet-based energy analysis was performed. The comparison of energy level from the received sensor signal also presents different conditions of the concrete beam. This investigation is significant to provide a prompt warning of material migration from underground containment for nuclear materials.

This dissertation developed an active sensing approach using smart aggregates to monitor the very early age concrete hydration process, as shown in Chapter 7. Three stages, liquid stage, transition stage, and hardened stage, are observed from the received sensing signal. A comparison study of concrete hydration monitoring using compressive and shear modes smart aggregates were also investigated. It is found that the average of received signal from SMSAs is stronger than that from CMSAs. In addition, the effective concrete hydration monitoring for SMSAs can start from the beginning of the hydration, which is earlier than CMSAs based concrete hydration monitoring. The influence of concrete hydration behavior from different concrete mix was not investigated in the research. In the future research, the effect of mineral admixture on the hydration process of concretes can be revealed.

This dissertation proposed an active sensing approach to monitoring the soil freeze-thaw process. Smart aggregates were used as actuators and sensors in different sizes of soil specimens. A wavelet packet-based structural index can quantitatively characterize the cyclic soil freeze-thaw process. In the soil freeze-thaw cycle, the index can have different values at the same soil temperature, depending on if it is at the freezing process or the thawing process. Possible reason is hysteresis in the water phase transition. Potentially the active sensing approach with smart aggregates could be developed further into a technology for characterizing partially frozen soil or very warm permafrost that poses many engineering challenges with future studies.

References

- [1] Song, G., Gu, H., and Mo, Y. L. (2008). Smart Aggregates: Multi-Functional Sensors for Concrete Structures—A Tutorial and A Review. *Smart Materials and Structures*, 17(3), 033001.
- [2] Hou, S., Zhang, H. B., and Ou, J. P. (2012). A PZT-based Smart Aggregate for Compressive Seismic Stress Monitoring. *Smart Materials and Structures*, 21(10), 105035.
- [3] Zhu, S., Levinson, D., Liu, H.X., and Harder, K. (2010). The Traffic and Behavioral Effects of the I-35W Mississippi River Bridge Collapse. *Transportation research part A: policy and practice*, 44(10), 771-784.
- [4] Farrar, C.R., and Worden, K. (2007). An Introduction to Structural Health Monitoring. *Philosophical Transactions of the Royal Society A: Mathematical, Physical and Engineering Sciences*, 365(1851), 303-315.
- [5] Phares, B.M., Rolander, D.D., Graybeal, B.A., and Washer, G.A. (2000). Studying the Teliability of Bridge Inspection. *Public Roads*, 64(3).
- [6] Staszewski, W., Boller, C., Tomlinson, G. R, and Editors. (2004) *Health Monitoring of Serospace Dtructures: Smart Sensor Technologies and Signal Processing*.
- [7] Leutenegger, T., Schlums, D. H., and Dual, J. (1999) *Structural Testing of Fatigued Structures*. In *1999 Symposium on Smart Structures and Materials* (pp. 987-997). International Society for Optics and Photonics.

- [8] Hannah, R.L. and Reed, S.E. (Eds.) (1992). Strain Gage Users' Manual, p. 122. Society for Experimental Mechanics. ISBN 0-912053-36-4.
- [9] Harris, C. M. (2002). Harris' shock and vibration handbook (Vol. 5). New York: McGraw-Hill.
- [10] Choi, H., Choi, S., and Cha, H. (2008, June). Structural Health Monitoring System based on Strain Gauge Enabled Wireless Sensor Nodes. In Networked Sensing Systems, 2008. INSS 2008. 5th International Conference on (pp. 211-214). IEEE.
- [11] Pecora, A., Maiolo, L., Minotti, A., De Francesco, R., De Francesco, E., Leccese, F., and Ferrone, A. (2014, May). Strain Gauge Sensors based on Thermoplastic Nanocomposite for Monitoring Inflatable Structures. In Metrology for Aerospace (MetroAeroSpace), 2014 IEEE (pp. 84-88). IEEE.
- [12] Kashyap, R., and López-Higuera, J.M. (2002). Handbook of Optical Fibre Sensing Technology ed J M López-Higuera (New York Wiley) p 349
- [13] Majumder, M., Gangopadhyay, T.K., Chakraborty, A.K., Dasguta, K., and Bhattacharya, D.K. (2008) Fibre Bragg Gratings in Structural Health Monitoring – Present status and applications Sensors and Actuators. A Physical 147 150-164
- [14] Chung, W., and Kang, D. (2008). Full-scale Test of A Concrete Box Girder using FBG Sensing System. Engineering Structures 30 643–652
- [15] Ren, L., Li, H.N., Zhou, J., Li, D.S., and Sun, L. (2006). Health Monitoring System for Offshore Platform with Fiber Bragg Grating Sensors. Optical Engineering 45 084401-1-9

- [16] Li, X. (2007). Finite Element Modeling Of Skewed Reinforced Concrete Bridges And The Bond-Slip Relationship Between Concrete And Reinforcement Auburn. University MS Thesis
- [17] Yeo, T.L, Sun, T., and Grattan, K.T.V. (2008). Fibre-optic Sensor Technologies for Humidity and Moisture Measurement. *Sensors and Actuators A* 144 280-295
- [18] Ikeda, T., and Ikeda, T. (1990). *Fundamentals of Piezoelectricity (Vol. 2)*. Oxford: Oxford university press.
- [19] Bhalla, S., and Soh, C. K. (2004). High Frequency Piezoelectric Signatures for Diagnosis of Seismic/blast Induced Structural Damages. *Ndt and E International*, 37(1), 23-33.
- [20] Na, W. B., and Kundu, T. (2003). Inspection of Interfaces between Corroded Steel Bars and Concrete using the Combination of a Piezoelectric Zirconate-Titanate Transducer and an Electromagnetic Acoustic Transducer. *Experimental mechanics*, 43(1), 24-31.
- [21] Raju, V., Park, G., and Cudney, H. H. (1999, March). Impedance-based Health Monitoring of Composite Reinforced Structures. In *Ninth International Conference on Adaptive Structures and Technologies* (pp. 448-457).
- [22] Park, G., Cudney, H. H., and Inman, D. J. (2001). Feasibility of using Impedance - based Damage Assessment for Pipeline Structures. *Earthquake engineering and structural dynamics*, 30(10), 1463-1474.

- [23] Song, G., Olmi, C., and Gu, H. (2007). An Overheight Vehicle–bridge Collision Monitoring System using Piezoelectric Transducers. *Smart materials and structures*, 16(2), 462.
- [24] Friswell, M.I. (2007). Damage Identification using Inverse Methods. *Philosophical Transactions of the Royal Society A: Mathematical, Physical and Engineering Sciences*, 365(1851), 393-410.
- [25] Zak, A., Krawczuk, M., and Ostachowicz, W. (2001). Vibration of A Laminated Composite Plate with Closing Delamination. *Journal of Intelligent Material Systems and Structures*, 12(8), 545-551.
- [26] Messina, A., Contursi, T., and Williams, E. J. (1997). Multiple Damage Evaluation using Natural Frequency Changes. *Proceedings of the 15th International Modal Analysis Conference, Orlando, Florida*, 1, 652-657.
- [27] Stanbridge, A.B., Khan, A.Z., and Ewins, D.J. (1997). Fault Identification in Vibrating Structures using A Scanning Laser Doppler Vibrometer. *Structural Health Monitoring, Current Status and Perspectives*, 56-65.
- [28] Mal, A., Banerjee, S., and Ricci, F. (2007). An Automated Damage Identification Technique Based on Vibration and Wave Propagation Data. *Philosophical Transactions of the Royal Society A: Mathematical, Physical and Engineering Sciences*, 365(1851), 479-491.

- [29] Montalvao, D., Maia, N.M.M., and Ribeiro, A. M. R. (2006). A Review of Vibration-based Structural Health Monitoring with Special Emphasis on Composite Materials. *Shock and Vibration Digest*, 38(4), 295-326.
- [30] Keye, S., Rose, M., and Sachau, D. (2001, February). Localizing Delamination Damages in Aircraft Panels from Modal Damping Parameters. In *Proceedings of the 19th International Modal Analysis Conference (IMAC XIX)*, Kissimmee, Florida, USA (pp. 412-417).
- [31] Kyriazoglou, C., Le Page, B. H., & Guild, F. J. (2004). Vibration Damping for Crack Detection in Composite Laminates. *Composites Part A: Applied Science and Manufacturing*, 35(7), 945-953.
- [32] Sampaio, R.P.C., Maia, N.M.M., and Silva, J.M.M. (1999). Damage Detection Using the Frequency-response-function Curvature Method. *Journal of Sound and Vibration*, 226(5), 1029-1042.
- [33] Bandara, R.P., Chan, T. H., and Thambiratnam, D.P. (2014). Structural Damage Detection Method using Frequency Response Functions. *Structural Health Monitoring*, 1475921714522847.
- [34] Giurgiutiu, V., Reynolds, A., and Rogers, C. A. (1999). Experimental Investigation of E/M Impedance Health Monitoring for Spot-welded Structural Joints. *Journal of Intelligent Material Systems and Structures*, 10(10), 802-812.
- [35] Peairs, D. M., Park, G., and Inman, D. J. (2004). Improving Accessibility of the Impedance-based Structural Health Monitoring Method. *Journal of Intelligent Material Systems and Structures*, 15(2), 129-139.

- [36] Yang, Y., Divsholi, B. S., and Soh, C. K. (2010). A Reusable PZT Transducer for Monitoring Initial Hydration and Structural Health of Concrete. *Sensors*, 10(5), 5193-5208.
- [37] Divsholi, B. S., and Yang, Y. (2008, December). Application of PZT Sensors for Detection of Damage Severity and Location in Concrete. In *Smart Materials, Nano-and Micro-Smart Systems* (pp. 726813-726813). International Society for Optics and Photonics.
- [38] Park, S., Ahmad, S., Yun, C. B., and Roh, Y. (2006). Multiple Crack Detection of Concrete Structures using Impedance-based Structural Health Monitoring techniques. *Experimental Mechanics*, 46(5), 609-618.
- [39] Park, G., Cudney, H. H., and Inman, D. J. (2000). Impedance-based Health Monitoring of Civil Structural Components. *Journal of infrastructure systems*, 6(4), 153-160.
- [40] Divsholi, B. S., and Yang, Y. (2009, March). Application of Reusable PZT Sensors for Monitoring Initial Hydration of Concrete. In *SPIE Smart Structures and Materials Nondestructive Evaluation and Health Monitoring* (pp. 729222-729222). International Society for Optics and Photonics.
- [41] Shin, S. W., Qureshi, A. R., Lee, J. Y., and Yun, C. B. (2008). Piezoelectric Sensor based Nondestructive Active Monitoring of Strength Gain in Concrete. *Smart Materials and Structures*, 17(5), 055002.

- [42] Sabra, K. G., and Huston, S. (2011). Passive Structural Health Monitoring of A High-speed Naval Ship from Ambient Vibrations. *The Journal of the Acoustical Society of America*, 129(5), 2991-2999.
- [43] Ikemoto, Y., Suzuki, S., Okamoto, H., Murakami, H., Lin, X., Itoh, H., and Asama, H. (2008, August). Force Sensor System for Structural Health Monitoring using Passive RFID Tags for Structural Health Monitoring. In *Portable Information Devices, 2008 and the 2008 7th IEEE Conference on Polymers and Adhesives in Microelectronics and Photonics. PORTABLE-POLYTRONIC 2008. 2nd IEEE International Interdisciplinary Conference on* (pp. 1-6). IEEE.
- [44] Olund, J., and DeWolf, J. (2007). Passive Structural Health Monitoring of Connecticut's Bridge Infrastructure. *Journal of Infrastructure Systems*, 13(4), 330-339.
- [45] ASTM Standard Definitions of Terms Relating to Acoustic Emission, ASTM subcommittee E07, ASTM E610-82, 1982.
- [46] Physical Acoustics Corporation (2007), PCI-2 based AE system user's manual.
- [47] Lingard, S., C. W. Yu, and Yau C.F. (1993). Sliding Wear Studies using Acoustic Emission. *Wear*, 162: 597-604.
- [48] Carpinteri, A., Lacidogna, G., and Pugno, N. (2007). Structural Damage Diagnosis and Life-time Assessment by Acoustic Emission Monitoring. *Engineering Fracture Mechanics*, 74(1), 273-289.

- [49] Farhidzadeh, A., Dehghan-Niri, E., Salamone, S., Luna, B., and Whittaker, A. (2012). Monitoring Crack Propagation in Reinforced Concrete Shear Walls by Acoustic Emission. *Journal of Structural Engineering*, 139(12).
- [50] Farrar, C. R., Hemez, F.M., Shunk, D.D., Stinemates, D.W., Nadler, B.R., and Czarnecki, J.J. (2004). A Review of Structural Health Monitoring Literature: 1996-2001 (p. 303). Los Alamos, NM: Los Alamos National Laboratory.
- [51] Choi, K., and Chang, F.K. (1996). Identification of Impact Force and Location using Distributed Sensors. *AIAA journal*, 34(1), 136-142.
- [52] Pedemonte, P., Staszewski, W.J., Aymerich, F., Found, M.S., and Priolo, P. (2001, August). Signal Processing for Passive Impact Damage Detection in Composite Structures. In *SPIE's 8th Annual International Symposium on Smart Structures and Materials* (pp. 169-178). International Society for Optics and Photonics.
- [53] Staszewski, W. J., Mahzan, S., and Traynor, R. (2009). Health Monitoring of Aerospace Composite Structures—Active and Passive Approach. *Composites Science and Technology*, 69(11), 1678-1685.
- [54] Ihn, J.B., and Chang, F.K. (2008). Pitch-catch Active Sensing Methods in Structural Health Monitoring for Aircraft Structures. *Structural Health Monitoring*, 7(1), 5-19.
- [55] Yu, L., and Giurgiutiu, V. (2008). In Situ 2-D Piezoelectric Wafer Active Sensors Arrays for Guided Wave Damage Detection. *Ultrasonics*, 48(2), 117-134.

- [56] Saafi, M., and Sayyah, T. (2001). Health Monitoring of Concrete Structures Strengthened with Advanced Composite Materials using Piezoelectric Transducers. *Composites Part B: Engineering*, 32(4), 333-342.
- [57] Wang, R. L., Gu, H., and Song, G. (2013). Active Sensing Based Bolted Structure Health Monitoring using Piezoceramic Transducers. *International Journal of Distributed Sensor Networks*, 2013.
- [58] Wang, T., Song, G., Wang, Z., and Li, Y. (2013). Proof-of-concept Study of Monitoring Bolt Connection Status using a Piezoelectric based Active Sensing Method. *Smart Materials and Structures*, 22(8), 087001.
- [59] Ruan, J., Ho, S. C. M., Patil, D., Li, M., and Song, G. (2014). Wind Turbine Blade Damage Detection using an Active Sensing Approach. *Smart Materials and Structures*, 23(10), 105005.
- [60] Du, G., Kong, Q., Lai, T., and Song, G. (2013). Feasibility Study on Crack Detection of Pipelines Using Piezoceramic Transducers. *International Journal of Distributed Sensor Networks*, 2013.
- [61] Chui, C. K. (Ed.). (1992). *An Introduction to Wavelets (Vol. 1)*. Academic press.
- [62] Hou, Z., Noori, M., and Amand, R.S. (2000). Wavelet-based Approach for Structural Damage Detection. *Journal of Engineering Mechanics*, 126(7), 677-683.
- [63] Sone, A., Yamamoto, S., Nakaoka, A., and Masuda, A. (1995). Health Monitoring System of Structures Based on Orthonormal Wave Let Transform. *ASME-PUBLICATIONS-PVP*, 312, 161-168.

- [64] Wang, W.J., and McFadden, P.D. (1995). Application of Orthogonal Wavelets to Early Gear Damage Detection. *Mechanical Systems and Signal Processing*, 9(5), 497-507.
- [65] Staszewski, W.J., and Tomlinson, G.R. (1994). Application of the Wavelet Transform to Fault Detection in A Spur Gear. *Mechanical Systems and Signal Processing*, 8(3), 289-307.
- [66] Al-Khalidy, A., Noori, M., Hou, Z., Yamamoto, S., Masuda, A., and Sone, A. (1997). Health Monitoring Systems of Linear Structures using Wavelet Analysis. In *Structural Health Monitoring—Current Status and Perspectives, Proceedings of the International Workshop on Structural Health Monitoring* (pp. 164-175).
- [67] Hou, Z., Noori, M., and Amand, R. S. (2000). Wavelet-based Approach for Structural Damage Detection. *Journal of Engineering Mechanics*, 126(7), 677-683.
- [68] Giurgiutiu, V. (2007). *Structural Health Monitoring: with Piezoelectric Wafer Active Sensors*. Academic Press.
- [69] Zhu, B., and Frangopol, D.M. (2013). Incorporation of Structural Health Monitoring Data on Load Effects in the Reliability and Redundancy Assessment of Ship Cross-sections using Bayesian Updating. *Structural Health Monitoring*, 12(4), 377-392.
- [70] Michaels, T.E., Ruzzene, M., and Michaels, J.E. (2009, March). Frequency-wavenumber Domain Methods for Analysis of Incident and Scattered Guided Wave Fields. In *SPIE Smart Structures and Materials+ Nondestructive Evaluation*

and Health Monitoring (pp. 729513-729513). International Society for Optics and Photonics.

- [71] Fink, M. (1992). Time Reversal of Ultrasonic Fields. I. Basic principles. *Ultrasonics, Ferroelectrics and Frequency Control*, IEEE Transactions on 39. 5 555-566.
- [72] Wang, C.H., Rose, J.T., and Chang, F. K. (2004). A Synthetic Time-reversal Imaging Method for Structural Health Monitoring. *Smart materials and structures*, 13(2), 415.
- [73] Chen, Y., Gunawan, E., Low, K.S., Wang, S.C., Soh, C.B., and Putti, T.C. (2008). Time-reversal Ultrawideband Breast Imaging: Pulse Design Criteria Considering Multiple Tumors with Unknown Tissue Properties. *Antennas and Propagation, IEEE Transactions on*, 56(9), 3073-3077.
- [74] Park, H.W., Sohn, H., Law, K. H., and Farrar, C.R. (2007). Time Reversal Active Sensing for Health Monitoring of A Composite Plate. *Journal of Sound and Vibration*, 302(1), 50-66.
- [75] Sakamoto, T., and Sato, T. (2010, July). A Target Tracking Method with A Single Antenna using Time-reversal UWB Radar Imaging in A Multi-path Environment. *In Geoscience and Remote Sensing Symposium (IGARSS), 2010 IEEE International* (pp. 3319-3322). IEEE.

- [76] Spina, D., Garibaldi, L., Marchesiello, S., Giorcelli, E., and Fasana, A. (1999). Different Analysis Techniques Applied to Seismic Data from the 1997 Italian Earthquake. *Key Engineering Materials*, 167, 432.
- [77] Piombo, B.A.D., Garibaldi, L., Giorcelli, E., and Marchesiello, S. (2000). CVA-ARMAV Capabilities Comparison Over the Heritage Court Tower Data. In *SPIE proceedings series* (pp. 1099-1105). Society of Photo-Optical Instrumentation Engineers.
- [78] Marchesiello, S., Piombo, B.A.D., and Sorrentino, S. (2001, February). Application of the CVA-BR Method to the Z 24 Bridge Vibration Data. In *IMAC-XIX: A Conference on Structural Dynamics*, (Vol. 1, pp. 864-869).
- [79] Jaffe, B. (2012). *Piezoelectric ceramics* (Vol. 3). Elsevier.
- [80] Yang, J. (2005). *An Introduction to the Theory of Piezoelectricity* (Vol. 9). Springer.
- [81] Meitzler, A., Tiersten, H.F., Warner, A.W., Berlincourt, D., Couqin, G.A., and Welsh III, F.S. (1988). *IEEE Standard on Piezoelectricity*.
- [82] Song, G., Gu, H., Mo, Y.L., Hsu, T.T.C., and Dhonde, H. (2007). Concrete Structural Health Monitoring using Embedded Piezoceramic Transducers. *Smart Materials and Structures*, 16(4), 959.
- [83] Yan, S., Sun, W., Song, G., Gu, H., Huo, L.S., Liu, B., and Zhang, Y.G. (2009). Health Monitoring of Reinforced Concrete Shear Walls using Smart Aggregates. *Smart Materials and Structures*, 18(4), 047001.

- [84] Laskar, A., Gu, H., Mo, Y.L., and Song, G. (2009). Progressive Collapse of A Two-story Reinforced Concrete Frame with Embedded Smart Aggregates. *Smart Materials and Structures*, 18(7), 075001.
- [85] Moslehy, Y., Gu, H., Belarbi, A., Mo, Y.L., and Song, G. (2010). Smart Aggregate Based Damage Detection of Circular RC Columns under Cyclic Combined Loading. *Smart Materials and Structures*, 19(6), 065021.
- [86] Gu, H., Song, G., Dhonde, H., Mo, Y.L., and Yan, S. (2006). Concrete Early-age Strength Monitoring using Embedded Piezoelectric Transducers. *Smart materials and structures*, 15(6), 1837.
- [87] Kong, Q., Hou, S., Ji, Q., Mo, Y.L., and Song, G. (2013). Very Early Age Concrete Hydration Characterization Monitoring using Piezoceramic Based Smart Aggregates. *Smart Materials and Structures*, 22(8), 085025.
- [88] Xu, B., Li, B., and Song, G. (2012). Active Debonding Detection for Large Rectangular CFSTs Based on Wavelet Packet Energy Spectrum with Piezoceramics. *Journal of Structural Engineering*, 139(9), 1435-1443.
- [89] Xu, B., Zhang, T., Song, G., and Gu, H. (2013). Active Interface Debonding Detection of A Concrete-filled Steel Tube with Piezoelectric Technologies using Wavelet Packet Analysis. *Mechanical Systems and Signal Processing*, 36(1), 7-17.
- [90] Chung, K., Kharkovsky, S., Kong, Q., and Song, G. (2014, May). Cure-state Monitoring of Concrete and Mortar Specimens using Smart Aggregates.

Instrumentation and Measurement Technology Conference (I2MTC) Proceedings, 2014 IEEE International (pp. 304-308). IEEE.

- [91] Hera, A., and Hou, Z. (2004). Application of Wavelet Approach for ASCE Structural Health Monitoring Benchmark Studies. *Journal of Engineering Mechanics*, 130(1), 96-104.
- [92] Kabsch, W. (1976). A Solution for the Best Rotation to Relate two Sets of Vectors. *Acta Crystallographica Section A: Crystal Physics, Diffraction, Theoretical and General Crystallography*, 32(5), 922-923.
- [93] Li, H., Sun, H.M., and Song, G. (2004, July). Damage Diagnosis of Framework Structure Based on Wavelet Packet Analysis and Neural Network. In *Smart Structures and Materials* (pp. 533-542). International Society for Optics and Photonics.
- [94] Wang, J., Shi, Z., and Han, Z. (2013). Analytical Solution of Piezoelectric Composite Stack Transducers. *Journal of Intelligent Material Systems and Structures*, 24(13), 1626-1636.
- [95] Wang, J.J., Shi, Z.F. (2013). Dynamic Characteristics of An Axially Polarized Multilayer Piezoelectric/elastic Composite Cylindrical Transducer. *IEEE Trans. Ultrason. Ferroelectr. Freq. Control* 60 2196-203
- [96] Shi, Z.F., Wang, J.J. (2013). Dynamic Analysis of 2-2 Cement-based Piezoelectric Transducers *J. Intell. Mater. Syst. Struct.* 24 99-107

- [97] Hu, J., Lin, S., Zhang, X., Wang, Y. (2014). Radially Sandwiched Composite Transducers Composed of the Radially Polarized Piezoelectric Ceramic Circular Ring and Metal Rings *Acta Acust. united Ac.* 100 418-26
- [98] Li, Y.D., Lee, K.Y., Zhang, N. (2012). A Generalized Hypergeometric Function Method for Axisymmetric Vibration Analysis of a Piezoelectric Actuator *Eur. J. Mech. A-Solid.* 31 110-16
- [99] Lin, S. (2008). The Radial Composite Piezoelectric Ceramic Transducer Sensors *Actuators A* 141 136-43
- [100] Lin, S. (2008) The Radial Composite Piezoelectric Ceramic Transducer Sensors *Actuators A* 141 136-43
- [101] Chen, W.Q., Lu, C.F., Yang, J.S., and Wang, J. (2009). A Circular Cylindrical, Radially Polarized Ceramic Shell Piezoelectric Transformer. *IEEE Trans. Ultrason. Ferroelectr. Freq. Control* 56 1238-45
- [102] Li, P., Jin, F. (2013). Effects of the Viscoelastic Interface Bonding on A Thickness-shear Mode Circular Cylindrical Piezoelectric Transformer *J. Intell. Mater. Syst. Struct.* 24 1888-96
- [103] Lin, S., Hu, J., Fu, Z.Q. (2013). Electromechanical Characteristics of Piezoelectric Ceramic Transformers in Radial Vibration Composed of Concentric Piezoelectric Ceramic Disk and Ring *Smart Mater. Struct.* 22 045018

- [104] Yang, J.S., Chen, Z.G., Hu, Y.T. (2007). Theoretical Modeling of A Thickness-Shear Mode Circular Cylinder Piezoelectric Transformer. *IEEE Trans. Ultrason. Ferroelectr. Freq. Control* 54 621-26
- [105] Xiang, H.J., Shi, Z.F. (2008). Static Analysis for Multi-layered Piezoelectric Cantilevers. *Int. J. Solids Struct.* 45 113-28
- [106] Mason, W.P. (1950). *Piezoelectric Crystals and their Application to Ultrasonics.* van Nostrand.
- [107] Pettersson, D., and Thelandersson, S. (2001). Crack Development in Concrete Structures Due to Imposed Strains—Part I: Modelling. *Materials and Structures*, 34(1), 7-13.
- [108] Raghavan, A., and Cesnik, C.E. (2007). Review of Guided-wave Structural Health Monitoring. *Shock and Vibration Digest*, 39(2), 91-116.
- [109] Giurgiutiu, V., and Bao, J. (2004). Embedded-ultrasonics Structural Radar for in situ Structural Health Monitoring of Thin-wall Structures. *Structural Health Monitoring*, 3(2), 121-140.
- [110] Wang, Y., Zhu, X., Hao, H., and Ou, J. (2009). Guided Wave Propagation and Spectral Element Method for Debonding Damage Assessment in RC Structures. *Journal of sound and vibration*, 324(3), 751-772.
- [111] Ruan, J., Ho, S.C. M., Patil, D., and Song, G. (2014, April). Structural Health Monitoring of Wind Turbine Blade using Piezoceramic based Active Sensing and

- Impedance Sensing. In Networking, Sensing and Control (ICNSC), 2014 IEEE 11th International Conference on (pp. 661-666). IEEE.
- [112] Li, H.N., Li, D.S., and Song, G.B. (2004). Recent Applications of Fiber Optic Sensors to Health Monitoring in Civil Engineering. *Engineering structures*, 26(11), 1647-1657.
- [113] Anastasopoulos A., Kourousis D., and Bollas K. (2009). Acoustic Emission Leak Detection of Liquid Filled Buried Pipeline. *J. Acoustic Emission*, vol. 27, pp. 27-39.
- [114] Ramuhalli, P., Udpa, L., and Udpa, S.S. (2003). Neural Network-based Inversion Algorithms in Magnetic Flux Leakage Nondestructive Evaluation. *Journal of applied physics*, 93(10), 8274-8276.
- [115] Okamoto Jr, J., Adamowski, J.C., Tsuzuki, M. S., Buiochi, F., and Camerini, C.S. (1999). Autonomous System for Oil Pipelines Inspection. *Mechatronics*, 9(7), 731-743.
- [116] Vasic, D., Bilas, V., and Ambrus, D. (2004). Pulsed Eddy-current Nondestructive Testing of Ferromagnetic Tubes. *Instrumentation and Measurement, IEEE Transactions on*, 53(4), 1289-1294.
- [117] Jiabao, Y. (2012). Ultimate Strength Behavior of Steel-Concrete-Steel Sandwich Composite Beams and Shells (Doctoral dissertation).
- [118] Braverman, J., Morante, R., and Hofmayer, C. (1997). Assessment of Modular Construction for Safety-related Structures at Advanced Nuclear Power Plants.

Nuclear Regulatory Commission, Washington, DC (United States). Div. of Engineering Technology.

- [119] Mizuno, J., Koshika, N., Tanaka, E., Suzuki, A., Nishimura, I., and Mihara, Y. (2005). Investigation on Impact Resistance of Steel Plate Reinforced Concrete Barriers Against Aircraft Impact Part 3: Analyses of Full-Scale Aircraft Impact. Transactions of the 18th SMiRT.
- [120] Yamamoto, T., Katoh, A., Chikazawa, Y., and Negishi, K. (2012). Design Evaluation Method of Steel-Plate Reinforced Concrete Structure Containment Vessel for Sodium-Cooled Fast Reactor. Journal ref: Journal of Disaster Research, 7(5), 645-655.
- [121] Jiabao, Y. (2012). Ultimate Strength Behaviour of Steel-Concrete-Steel Sandwich Composite Beams and Shells (Doctoral dissertation).
- [122] Montague, P., and Choo, Y.S. (1981, January). Double-skin Construction of Large Pressure Vessels for Sub-sea Systems. In Offshore Technology Conference. Offshore Technology Conference.
- [123] Subedi, N.K., and Coyle, N.R. (2002). Improving the Strength of Fully Composite Steel-concrete-steel Beam Elements by Increased Surface Roughness—An Experimental Study. Engineering structures, 24(10), 1349-1355.
- [124] Wu, F., and Chang, F.K. (2006). Debond Detection using Embedded Piezoelectric Elements in Reinforced Concrete Structures-part I: Experiment. Structural Health Monitoring, 5(1), 5-15.

- [125] Yan, S., Fu, J., Sun, W., Qi, B., and Liu, F. (2014). PZT-Based Detection of Compactness of Concrete in Concrete Filled Steel Tube Using Time Reversal Method. *Mathematical Problems in Engineering*, 2014.
- [126] Achenbach, J. (1984). *Wave Propagation in Elastic Solids*. Elsevier.
- [127] Multon, S., and Toutlemonde, F. (2004). Water Distribution in Concrete Beams. *Materials and Structures*, 37(6), 378-386.
- [128] Yeo, T. L., Eckstein, D., McKinley, B., Boswell, L.F., Sun, T., and Grattan, K.T.V. (2006). Demonstration of a Fibre-optic Sensing Technique for the Measurement of Moisture Absorption in Concrete. *Smart materials and structures*, 15(2), N40.
- [129] Ong, J.B., You, Z., Mills-Beale, J., Tan, E.L., Pereles, B.D., and Ong, K.G. (2008). A Wireless, Passive Embedded Sensor for Real-time Monitoring of Water Content in Civil Engineering Materials. *Sensors Journal, IEEE*, 8(12), 2053-2058.
- [130] Zou, X., Chao, A., Wu, N., Tian, Y., Yu, T.Y., and Wang, X. (2012, April). Miniature Fiber Optic Temperature Sensor for Concrete Structural Health Monitoring. In *SPIE Smart Structures and Materials+ Nondestructive Evaluation and Health Monitoring* (pp. 83454V-83454V). International Society for Optics and Photonics.
- [131] Azenha, M., Faria, R., and Figueiras, H. (2011). Thermography as A Technique for Monitoring Early Age Temperatures of Hardening Concrete. *Construction and Building Materials*, 25(11), 4232-4240.

- [132] Park, G., Sohn, H., Farrar, C.R., and Inman, D.J. (2003). Overview of Piezoelectric Impedance-based Health Monitoring and Path Forward. *Shock and Vibration Digest*, 35(6), 451-464.
- [133] Divsholi, B.S., and Yang, Y. (2012). Health Monitoring of Steel Structures using Sub-frequency Electromechanical Impedance Technique. *Journal of Nondestructive Evaluation*, 31(3), 197-207.
- [134] McCarter, W.J. (1994). A Parametric Study of the Impedance Characteristics of Cement-aggregate Systems during Early Hydration. *Cement and concrete research*, 24(6), 1097-1110.
- [135] Abo-Qudais, S.A. (2005). Effect of Concrete Mixing Parameters on Propagation of Ultrasonic Waves. *Construction and building materials*, 19(4), 257-263.
- [136] Keating, J., Hannant, D.J., and Hibbert, A.P. (1989). Correlation between Cube Strength, Ultrasonic Pulse Velocity and Volume Change for Oil Well Cement Slurries. *Cement and Concrete Research*, 19(5), 715-726.
- [137] Voigt, T., Grosse, C.U., Sun, Z., Shah, S.P., and Reinhardt, H.W. (2005). Comparison of Ultrasonic Wave Transmission and Reflection Measurements with P-and S-waves on Early Age Mortar and Concrete. *Materials and Structures*, 38(8), 729-738.
- [138] Voigt, T., Ye, G., Sun, Z., Shah, S.P., and Breugel, K. (2005). Early Age Microstructure of Portland Cement Mortar Investigated by Ultrasonic Shear Waves and Numerical Simulation. *Cement and concrete research*, 35(5), 858-866.

- [139] Zhang, J., Qin, L., and Li, Z. (2009). Hydration Monitoring of Cement-based Materials with Resistivity and Ultrasonic Methods. *Materials and Structures*, 42(1), 15-24.
- [140] Xu, Q., Ruiz, J. M., Hu, J., Wang, K., and Rasmussen, R.O. (2011). Modeling Hydration Properties and Temperature Developments of Early-age Concrete Pavement using Calorimetry Tests. *Thermochimica Acta*, 512(1), 76-85.
- [141] Branco, F.A., Mendes, P., and Mirambell, E. (1992). Heat of Hydration Effects in Concrete Structures. *ACI Materials Journal*, 89(2).
- [142] Xiong, F., and Yang, Z.J. (2008). Effects of Seasonally Frozen Soil on the Seismic Behavior of Bridges. *Cold Regions Science and Technology*, 54(1), 44-53.
- [143] Yang, Z., Dutta, U., Xiong, F., Biswas, N., and Benz, H. (2008). Seasonal Frost Effects on the Dynamic Behavior of A Twenty-story Office Building. *Cold Regions Science and Technology*, 51(1), 76-84.
- [144] Yang, Z.J., Dutta, U., Zhu, D., Marx, E., and Biswas, N. (2007). Seasonal Frost Effects on the Soil–foundation–structure Interaction System. *Journal of Cold Regions Engineering*, 21(4), 108-120.
- [145] Robinson, D.A., Frei, A., and Serreze, M.C. (1995). Recent Variations and Regional Relationships in Northern Hemisphere Snow Cover. *Annals of Glaciology*, 21, 71-76.

- [146] Zhang, T., Barry, R.G., Knowles, K., Heginbottom, J.A., and Brown, J. (2008). Statistics and Characteristics of Permafrost and Ground-ice Distribution in the Northern Hemisphere. *Polar Geography*, 31(1-2), 47-68.
- [147] Elachi, C., and Van Zyl, J.J. (2006). *Introduction to the Physics and Techniques of Remote Sensing* (Vol. 28). John Wiley & Sons.
- [148] Frohling, S., McDonald, K.C., Kimball, J.S., Way, J.B., Zimmermann, R., and Running, S.W. (1999). Using the Space Borne NASA Scatterometer (NSCAT) to Determine the Frozen and Thawed Seasons. *Journal of Geophysical Research: Atmospheres* (1984–2012), 104(D22), 27895-27907.
- [149] McDonald, K.C., and Kimball, J.S. (2005). Estimation of Surface Freeze–thaw States using Microwave Sensors. *Encyclopedia of hydrological sciences*.
- [150] Naeimi, V., Paulik, C., Bartsch, A., Wagner, W., Kidd, R., Park, S.E., and Boike, J. (2012). ASCAT Surface State Flag (SSF): Extracting Information on Surface Freeze/thaw Conditions from Backscatter Data using An Empirical Threshold-Analysis Algorithm. *Geoscience and Remote Sensing, IEEE Transactions on*, 50(7), 2566-2582.
- [151] Zwieback, S., Bartsch, A., Melzer, T., and Wagner, W. (2012). Probabilistic Fusion of Ku and C Band Scatterometer Data for Determining the Freeze/Thaw State. *IEEE Transactions on Geoscience and Remote Sensing*. DOI: 10.1109/TGRS.2011.2169076

- [152] Li, X., Shih, W.Y., Vartuli, J., Milius, D.L., Prud'homme, R., Aksay, I.A., and Shih, W.H. (2002). Detection of Water-ice Transition using A Lead Zirconate titanate/brass Transducer. *Journal of applied physics*, 92(1), 106-111.
- [153] Tseng, K.K., and Naidu, A.S.K. (2002). Non-parametric Damage Detection and Characterization using Smart Piezoceramic Material. *Smart Materials and Structures*, 11(3), 317.
- [154] Gu, H., Moslehy, Y., Sanders, D., Song, G., and Mo, Y.L. (2010). Multi-Functional Smart Aggregate-based Structural Health Monitoring of Circular Reinforced Concrete Columns Subjected to Seismic Excitations. *Smart Materials and Structures*, 19(6), 065026.
- [155] Lee, J.S., and Santamarina, J. C. (2005). Bender Elements: Performance and Signal interpretation. *Journal of Geotechnical and Geoenvironmental Engineering*, 131(9), 1063-1070.

Appendices

Appendix A

$$a_{mm} = \begin{bmatrix} a_{11} & a_{12} & \cdots & a_{1n} \\ a_{21} & a_{22} & \cdots & a_{2n} \\ \cdots & \cdots & \cdots & \cdots \\ a_{m1} & a_{m2} & \cdots & a_{mn} \end{bmatrix} \quad (\text{A.1})$$

$$A_\alpha = \begin{bmatrix} A_\alpha^{(1)} & A_\alpha^{(2)} \end{bmatrix}^T \quad (\text{A.2})$$

where

$$A_\alpha^{(1)} = \begin{bmatrix} A_M^{(1)} & B_M^{(1)} & A_{EM} & B_{EM} & A_{CM}^{(1)} & B_{CM}^{(1)} & A_{PCM}^{(1)} & B_{PCM}^{(1)} & C_1^{(1)} & C_0^{(1)} & A_{PCM}^{(2)} \end{bmatrix}$$

$$A_\alpha^{(2)} = \begin{bmatrix} B_{PCM}^{(2)} & C_1^{(2)} & C_0^{(2)} & A_{CM}^{(2)} & B_{CM}^{(2)} & A_{CE} & B_{CE} & A_E & B_E & A_M^{(2)} & B_M^{(2)} \end{bmatrix}$$

$$B_\alpha = \begin{bmatrix} B_\alpha^{(1)} & B_\alpha^{(2)} \end{bmatrix}^T \quad (\text{A.3})$$

where

$$B_\alpha^{(1)} = [0 \ 0 \ 0 \ 0 \ 0 \ 0 \ 0 \ 0 \ 0 \ 1 \ 0 \ 0]$$

$$B_\alpha^{(2)} = [1 \ 0 \ 0 \ 0 \ 0 \ 0 \ 0 \ 0 \ 0 \ 0 \ 0 \ 0]$$

$$B_\alpha^{(3)} = \left[(a_{1(13)} - a_{1(9)}) \ (a_{2(13)} - a_{2(9)}) \ \cdots \ (a_{m(13)} - a_{m(9)}) \right]^T \quad (\text{A.4})$$

Matrix elements of (A.1)

The effective coefficients in Eq. (A.1) are listed as follow, and other unmentioned coefficients are zero.

$$a_{11} = 1, a_{12} = 0 \quad (\text{B.1})$$

$$\begin{aligned} a_{21} = f_1(h_1), a_{22} = f_2(h_1), a_{23} = -f_3(h_1), a_{24} = -f_4(h_1) \\ a_{31} = g_2(h_1), a_{32} = -g_1(h_1), a_{33} = -g_4(h_1), a_{34} = g_3(h_1) \end{aligned} \quad (\text{B.2})$$

$$\begin{aligned} a_{43} = f_3(h_2), a_{44} = f_4(h_2), a_{45} = -f_5(h_2), a_{46} = -f_6(h_2) \\ a_{53} = g_4(h_2), a_{54} = -g_3(h_2), a_{55} = -g_6(h_2), a_{56} = g_5(h_2) \end{aligned} \quad (\text{B.3})$$

$$\begin{aligned} a_{65} = f_5(h_3), a_{66} = f_6(h_3), a_{67} = -f_7(h_3), a_{68} = -f_8(h_3) \\ a_{75} = g_6(h_3), a_{76} = -g_5(h_3), a_{77} = -g_8(h_3), a_{78} = g_7(h_3), a_{79} = -\Delta_2 \end{aligned} \quad (\text{B.4})$$

$$\begin{aligned} a_{87} = f_7(h_3), a_{88} = f_8(h_3), a_{89} = h_3, a_{8(10)} = 1 \\ a_{97} = \Delta_1 f_7(h_4), a_{98} = \Delta_1 f_8(h_4), a_{99} = \Delta_1 h_4, a_{9(10)} = \Delta_1 \end{aligned} \quad (\text{B.5})$$

$$\begin{aligned} a_{10(7)} = f_7(h_4), a_{10(8)} = f_8(h_4), a_{10(11)} = -f_7(h_4), a_{10(12)} = -f_8(h_4) \\ a_{11(7)} = g_8(h_4), a_{11(8)} = -g_7(h_4), a_{11(9)} = \Delta_2, a_{11(11)} = -g_8(h_4), a_{11(12)} = g_7(h_4), \\ a_{11(13)} = -\Delta_2 \end{aligned} \quad (\text{B.6})$$

$$\begin{aligned} a_{12(11)} = -\Delta_1 f_7(h_4), a_{12(12)} = -\Delta_1 f_8(h_4), a_{12(13)} = -\Delta_1 h_4, a_{12(14)} = -\Delta_1 \\ a_{13(11)} = f_7(h_5), a_{13(12)} = f_8(h_5), a_{13(13)} = h_5, a_{13(14)} = 1 \end{aligned} \quad (\text{B.7})$$

$$\begin{aligned} a_{14(11)} = f_7(h_5), a_{14(12)} = f_8(h_5), a_{14(15)} = -f_5(h_5), a_{14(16)} = -f_6(h_5) \\ a_{15(11)} = g_8(h_5), a_{15(12)} = -g_7(h_5), a_{15(13)} = \Delta_2, a_{15(15)} = -g_6(h_5), a_{15(16)} = g_5(h_5) \end{aligned} \quad (\text{B.8})$$

$$\begin{aligned} a_{16(15)} = f_5(h_6), a_{16(16)} = f_6(h_6), a_{16(17)} = -f_9(h_6), a_{16(18)} = -f_{10}(h_6) \\ a_{17(15)} = g_6(h_6), a_{17(16)} = -g_5(h_6), a_{17(17)} = -g_{10}(h_6), a_{17(18)} = g_9(h_6) \end{aligned} \quad (\text{B.9})$$

$$\begin{aligned} a_{18(17)} = f_9(h_7), a_{18(18)} = f_{10}(h_7), a_{18(19)} = -f_{11}(h_7), a_{18(20)} = -f_{12}(h_7) \\ a_{19(17)} = g_{10}(h_7), a_{19(18)} = -g_9(h_7), a_{19(19)} = -g_{12}(h_7), a_{19(20)} = g_{11}(h_7) \end{aligned} \quad (\text{B.10})$$

$$\begin{aligned} a_{20(19)} = f_{11}(h_8), a_{20(20)} = f_{12}(h_8), a_{20(21)} = -f_1(h_8), a_{20(22)} = -f_2(h_8) \\ a_{21(19)} = g_{12}(h_8), a_{21(20)} = -g_{11}(h_8), a_{21(21)} = -g_2(h_8), a_{21(22)} = g_1(h_8) \end{aligned} \quad (\text{B.11})$$

$$a_{22(21)} = g_2(h_9), a_{22(22)} = -g_1(h_9) \quad (\text{B.12})$$

where

$$\Delta_1 = e_{33}/\kappa_{33}^\varepsilon, \quad \Delta_2 = \chi_1 (e_{33}^2/\kappa_{33}^\varepsilon) \quad (\text{B.13})$$

$$\begin{aligned} f_1(z) &= \sin k_M z, & f_2(z) &= \cos k_M z, & f_3(z) &= \sin k_{EM} z, & f_4(z) &= \cos k_{EM} z, \\ f_5(z) &= \sin k_{CM} z, & f_6(z) &= \cos k_{CM} z, & f_7(z) &= \sin k_{PCM} z, & f_8(z) &= \cos k_{PCM} z, \\ f_9(z) &= \sin k_{CE} z, & f_{10}(z) &= \cos k_{CE} z, & f_{11}(z) &= \sin k_E z, & f_{12}(z) &= \cos k_E z \end{aligned} \quad (\text{B.14})$$

$$\begin{aligned} g_1(z) &= p_M \sin k_M z, & g_2(z) &= p_M \cos k_M z, & g_3(z) &= p_{EM} \sin k_{EM} z, \\ g_4(z) &= p_{EM} \cos k_{EM} z, & g_5(z) &= p_{CM} \sin k_{CM} z, & g_6(z) &= p_{CM} \cos k_{CM} z, \\ g_7(z) &= p_{PCM} \sin k_{PCM} z, & g_8(z) &= p_{PCM} \cos k_{PCM} z, & g_9(z) &= p_{CE} \sin k_{CE} z, \\ g_{10}(z) &= p_{CE} \cos k_{CE} z, & g_{11}(z) &= p_E \sin k_E z, & g_{12}(z) &= p_E \cos k_E z \end{aligned} \quad (\text{B.15})$$

Appendix B

Unit Conversion Table	
1 inch	25.4 mm

